HAL
open science

Documentation of the NASA/Ames Legacy Mars Global Climate Model: Simulations of the present seasonal water cycle

Robert M. Haberle, Melinda A. Kahre, Jeffery L. Hollingsworth, Franck Montmessin, R. John Wilson, Richard A. Urata, Amanda S. Brecht, Michael J. Wolff, Alexandre M. Kling, James R. Schaeffer

To cite this version:

Robert M. Haberle, Melinda A. Kahre, Jeffery L. Hollingsworth, Franck Montmessin, R. John Wilson, et al.. Documentation of the NASA/Ames Legacy Mars Global Climate Model: Simulations of the present seasonal water cycle. Icarus, 2019, 333, pp.130-164. 10.1016/j.icarus.2019.03.026 . insu-02107018

HAL Id: insu-02107018

https://insu.hal.science/insu-02107018v1

Submitted on 11 Sep 2019

HAL is a multi-disciplinary open access archive for the deposit and dissemination of scientific research documents, whether they are published or not. The documents may come from teaching and research institutions in France or abroad, or from public or private research centers.

L'archive ouverte pluridisciplinaire **HAL**, est destinée au dépôt et à la diffusion de documents scientifiques de niveau recherche, publiés ou non, émanant des établissements d'enseignement et de recherche français ou étrangers, des laboratoires publics ou privés.

Icarus 333 (2019) 130–164

Contents lists available at ScienceDirect

Icarus

journal homepage: www.elsevier.com/locate/icarus

Documentation of the NASA/Ames Legacy Mars Global Climate Model: Simulations of the present seasonal water cycle

Robert M. Haberle[a,*], Melinda A. Kahre[a], Jeffery L. Hollingsworth[a], Franck Montmessin[b], R. John Wilson[a], Richard A. Urata[c], Amanda S. Brecht[a], Michael J. Wolff[d], Alexandre M. Kling[c], James R. Schaeffer[e,1]

[a] Space Science and Astrobiology Division, NASA/Ames Research Center, Moffett Field, CA 94035, United States of America
[b] Laboratoire Atmosphères, Milieux, Observations Spatiales, CNRS, Guyancourt, France
[c] Bay Area Environmental Research Institute, NASA/Ames Research Center, Moffett Field, CA 94035, United States of America
[d] Space Science Institute, Boulder, CO 80301, United States of America
[e] NASA/Ames Research Center, Moffett Field, CA, United States of America

ARTICLE INFO

Keywords:
Mars atmosphere
Mars Global Climate Model
Mars water cycle
Mars climate
Mars clouds
Mars atmospheric dynamics

ABSTRACT

We describe and document the physics packages in the legacy NASA/Ames Mars Global Climate Model, present simulations of the seasonal water cycle and how it compares with observations, assess the role of radiatively active clouds on the water cycle and planetary eddies, and discuss the strengths and weakness of the model and the implication for future efforts. The physics packages we describe include the treatment of surface properties, the ground temperature model, planetary boundary layer scheme, sublimation physics, cloud microphysics, the use of a moment method for tracer transport, a semi-interactive dust tracking scheme, and a two-stream radiative transfer code based on correlated-k's. With virtually no tuning of the water cycle and assuming the north polar residual water ice cap is the only source of water we find the model gives a reasonably good simulation of the present seasonal water cycle. No persistent clouds form over the residual cap, seasonal variations in column vapor abundances are similar to those observed, the aphelion cloud belt has about the right opacity, and surface and air temperatures are in reasonably good agreement with observations. The radiative effect of clouds does not significantly alter the seasonal and spatial variation of the moisture fields, though the clouds are thicker and the atmosphere somewhat wetter. As others have found cloud radiative forcing amplifies the mean meridional circulation, transient baroclinic eddies, and global thermal tides. However, it also changes the characteristics of forced stationary waves in ways that are not straightforward to understand. The main weakness of the model, we believe, is sluggish vertical mixing. Water is not transported high enough in the model and as a consequence the water cycle is too dry, the aphelion cloud belt is too low, and the mean meridional circulation is too shallow. These, we feel, could be remedied by some combination of non-local mixing, deep mountain-induced circulations, better horizontal and vertical resolution, and/or gravity wave drag. Efforts are now underway to study these issues as we are transitioning away from our legacy code to one with a more modern dynamical core.

1. Introduction

The main goal of this paper is to document the status of the NASA/Ames Legacy Mars Global Climate Model (GCM)present and interpret selected results from it, and provide a reference for future investigations using it and/or its physics packages. The legacy code is supported by the Mars Climate Modeling Center at NASA's Ames Research Center. As we are transitioning away from the legacy code to a variety of more modern cores having greater speed and better conservation properties, our focus here is on a description of the physics packages it has and the results they produce. These packages are being modularized for incorporation into the newer cores and will eventually be made available to the general public. It is timely therefore to document these algorithms and discuss how well they capture the present climate system.

The physics packages of greatest interest are those that relate to the water cycle. The water cycle is a fundamental component of the present climate system and modeling it requires algorithms that simulate the exchange of water between the surface and atmosphere, transport

* Corresponding author.
E-mail address: Robert.M.Haberle@nasa.gov (R.M. Haberle).
[1] Deceased.

https://doi.org/10.1016/j.icarus.2019.03.026
Received 29 August 2018; Received in revised form 13 February 2019; Accepted 18 March 2019
Available online 19 April 2019
0019-1035/ © 2019 The Authors. Published by Elsevier Inc. This is an open access article under the CC BY-NC-ND license (http://creativecommons.org/licenses/BY-NC-ND/4.0/).

around the planet, the microphysics of cloud formation and dissipation, and the radiative effects of clouds on diabatic heating rates. Interaction with airborne dust, a critical thermal drive for the global circulation and a source of ice nuclei (IN), and the seasonal growth and retreat of the CO_2 polar caps must also be included.

During the past decade we put considerable effort to developing, testing, analyzing, and improving the algorithms that simulate these processes. We now have high confidence in their robustness and a good understanding of how they work. This is not to say that the model is bug free, that the physics it includes is correct and complete, or that we fully understand everything it produces; models and their developers never achieve such lofty goals. They only strive for them. Instead, it is to say that we are ready to describe what we have and explain why we think it produces what it does.

In writing this paper two philosophical principles guide us. First, while other groups have developed GCMs to simulate the Martian water cycle (e.g., Richardson and Wilson, 2002; Montmessin et al., 2004; Madeleine et al., 2012; Urata and Toon, 2013; Navarro et al., 2014; Steele et al., 2014; Lee et al., 2018; Daerden et al., 2018; Neary and Daerden, 2018; Smith et al., 2018; Musiolik et al., 2018) the level of detail provided for documentation varies widely from group to group creating uncertainty when making comparisons or assessing physical processes. In this paper we fully document our model in order to clearly communicate what we have and to lay the foundation for understanding why it produces what it does. Mars GCMs have become quite sophisticated over the years yet many of the details of their physics packages remain inadequately described. Second, we make no attempt to tune the water cycle in the model. Instead we take care to be sure the model is forced properly and then seek to understand how well it simulates the water cycle with what we consider to be state-of-the-art algorithms. We make no ad-hoc assumptions about cloud particle sizes or surface properties, for example, in order to improve the simulations. Thus, we state our assumptions and parameter choices then show the model results discussing its strengths and weaknesses. Where it succeeds we highlight the reason; where it doesn't we assess the problem. Our intent with this full disclosure approach is to lay the groundwork for future improvements based on sound physical principles.

Our criterion for a successful water cycle simulation is to achieve an annually-equilibrated state with a cloud free atmosphere over the North Polar Residual Cap (NPRC) during summer, a decent aphelion cloud belt (ACB), reasonably good vapor and cloud column abundances, and the right surface and air temperatures. The reason for these choices is that they are well observed first-order characteristics of the water cycle that any model should reproduce. The observations by which we judge the model come primarily from the Thermal Emission Spectrometer (TES) on Mars Global Surveyor, and the Mars Climate Sounder (MCS), Compact Reconnaissance Imaging Spectrometer for Mars (CRISM), and Mars Color Imager (MARCI) on Mars Reconnaissance Orbiter. While the path to achieving a good comparison with these data sets comes mainly from the algorithms and physics described below, we also found that time splitting cloud microphysical processes, implementing a quasi-interactive dust vertical distribution scheme, and using a self-consistent VIS/IR dust opacity ratio were crucial to meeting the success criterion mentioned above.

After describing the model and its physics packages in Section 2 we show how it compares with observations in Section 3 and then assess the role of cloud radiative effects in Section 4. As previous groups have shown, the radiative effects of clouds are significant and cannot be ignored as they have a major impact on the thermal structure of the atmosphere and the mean meridional circulation in particular (e.g., Wilson et al., 2008; Madeleine et al., 2012; Navarro et al., 2014; Kahre et al., 2015). The global thermal tides (Hinson and Wilson, 2004; Kleinböhl et al., 2013; Wilson et al., 2014; Wilson and Guzewich, 2014) and transient baroclinic eddies (Wilson, 2011; Mulholland et al., 2016; Pottier et al., 2017) are also affected by radiatively active clouds and we assess their effect on these components of the global circulation as well. We take this work a step further and also examine the role of cloud forcing on forced stationary waves, which have not received much attention in the literature. In Section 5 we discuss some weaknesses of the model: overall the simulated water cycle is too dry, the ACB is too low, and high-altitude polar winter clouds too thin. We argue that these deficiencies are related to weak vertical transport, a common theme that emerges from these discussions. And finally, in Section 6, we summarize our efforts and make some concluding remarks about future efforts.

2. Model description

2.1. Overview

We refer to the model described here as version GCM_2.3. This version uses the latitude/longitude "C" grid dynamical core developed at Goddard Space Flight Center (Suarez and Takacs, 1995). As mentioned in the Introduction we are transitioning to more modern cores. For this paper, however, we use our legacy core to provide a benchmark for comparison. The transport scheme that came with this core was inaccurate and highly diffusive. We therefore replaced it with a Van Leer scheme to mitigate those deficiencies, as well as to minimize the prediction of negative mixing ratios, and allow for the zonal advection of tracers across more than one grid box in a given time step. In the simulations presented here, we run at 5° latitude by 6° longitude with 24 vertical layers whose thickness increases from ~ 10 m at the lowest layer, to ~5 km at the model top (8×10^{-6} Pa, or ~90 km).

The model transports a radiatively active dust particle size distribution but we constrain the predicted fields to reproduce observed opacities. At the surface we run with Mars Orbiter Laser Altimeter (MOLA) topography (Smith et al., 1999) and Oregon State University (OSU) soil properties (Tyler and Barnes, 2014) smoothed to the grid resolution. At high latitudes we include the effects of subsurface water ice on ground conduction by having a soil component overlie a pure water ice component in our subsurface module. The depth to the ice in each hemisphere is chosen to produce a good fit to the Viking Landers surface pressure data (Haberle et al., 2008). Gravity wave forcing is ignored in this version of the model.

For the water cycle, we assume that the surface deposits of water ice in the NPRC are the only source of atmospheric water. Hence, for now we neglect a possible adsorbing regolith. The distribution of ice is determined by the value of the grid-box averaged thermal inertia. We ignore the permanent CO_2 ice South Polar Residual Cap (SPRC) and thus have no permanent sinks for water. A standard stability dependent turbulent parameterization determines the flux of water off the NPRC where it is vertically mixed into the atmosphere by our level-2 boundary layer scheme and transported by model resolved winds. Water vapor nucleates onto the transported dust particles, then grows and settles using algorithms in our cloud microphysics package. The clouds are radiatively active with optical properties dependent on predicted sizes and dust content.

2.2. Surface properties

The albedo, thermal inertia, and topography that serve as the model's lower boundary condition are shown in Fig. 2.1. The albedo and thermal inertia data are taken from Putzig and Mellon (2007) with modifications to the north polar region poleward of 60°N by the OSU Mesoscale Modeling group. As described in Tyler and Barnes (2014), these modifications tune the albedo, thermal inertia, and deep soil temperatures to give a good match to surface temperatures. However, we note that our soil model, described below, does not tune deep soil temperatures so that further adjustments are needed. We discuss this in the next section. The topography in the model is based on the 1/16th degree MOLA data (Smith et al., 1999) averaged to our 5° × 6° grid and then applying a 9-point weighted smoother.

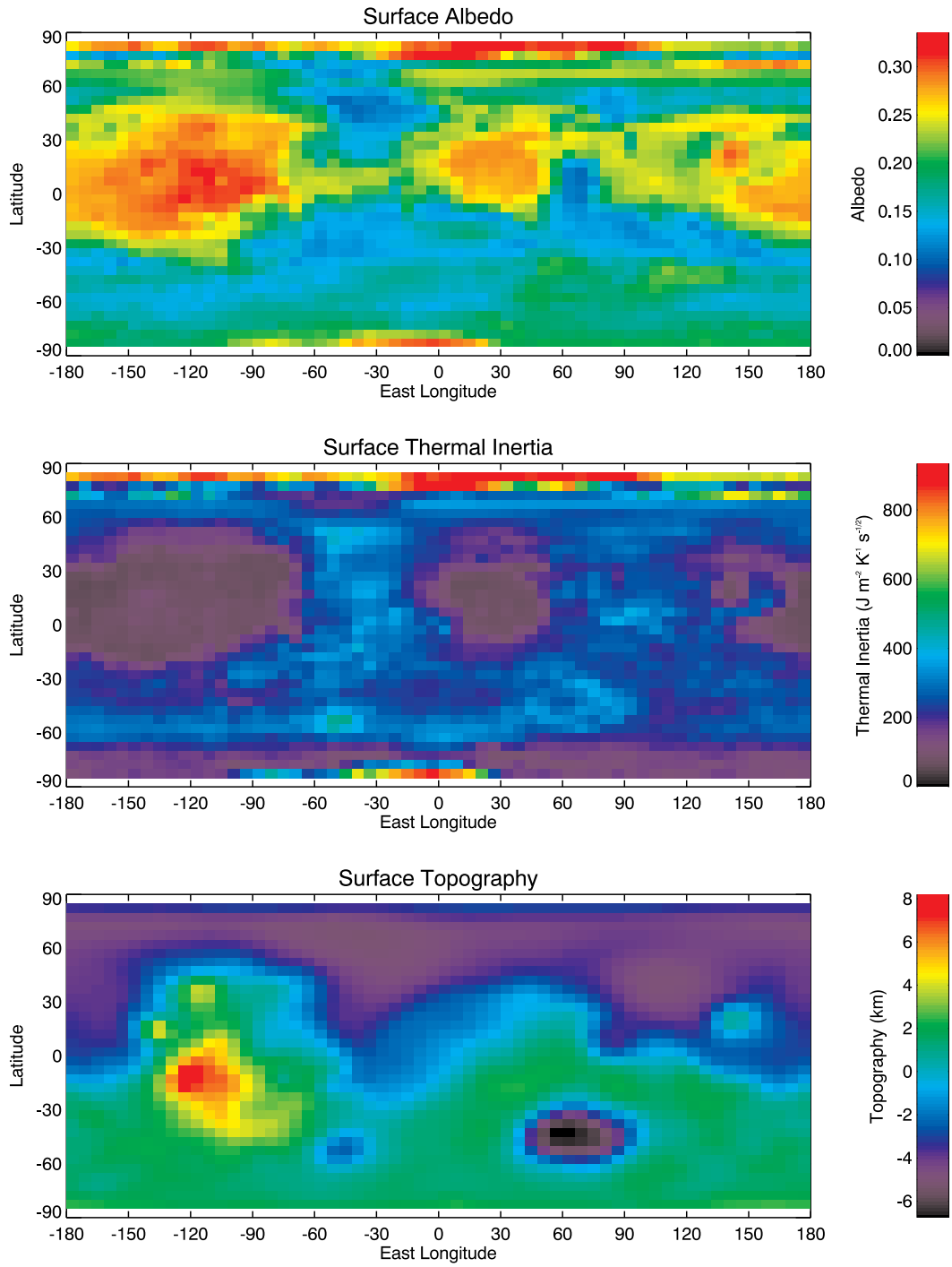

Fig. 2.1. Model surface boundary conditions: albedo (top), thermal inertia (middle), and topography (bottom). Thermal inertia units are SI: J $m^{-2} K^{-1} s^{-1/2}$.

As the NPRC is the only source of water in the model, we assume somewhat arbitrarily that ice is present in this region where the thermal inertia in the OSU maps exceeds 550 SI units. We choose thermal inertia as a proxy for ice because it represents properties averaged over a deeper layer than the albedo, and because dark regions can also be icy. Nevertheless, there is a good correlation between albedo and thermal inertia. The resulting boundaries are shown in Fig. 2.2. Between 82.5°N and 87.5°N ice is present at all longitudes with this prescription, while between 77.5°N and 82.5°N it exists only between −30° and +75° longitudes. In the 75°N band it is an outlier mainly in the +130° to +180° longitude sector. The total area of ice using this prescription is 1.03×10^{12} m^2. This is comparable to the area estimated by Navarro et al. (2014) using temperature as a proxy for ice. While this is about 37% less than that for uniform coverage poleward of 80°N, an assumption often used in early modeling efforts (e.g., Haberle and Jakosky, 1990; Richardson and Wilson, 2002), the water cycle does not dry out proportionately because the outliers at 75°N are warmer and sublimate more water vapor which offsets the size effect. Outside the NPRC we do not account for the radiative effects of transient surface ice. This would require making an assumption about the dependence of albedo on ice thickness, which is complicated due to the wide variation of rock abundances and surface properties. For simplicity, therefore, we use the bare ground albedo regardless of the presence or absence of surface ice.

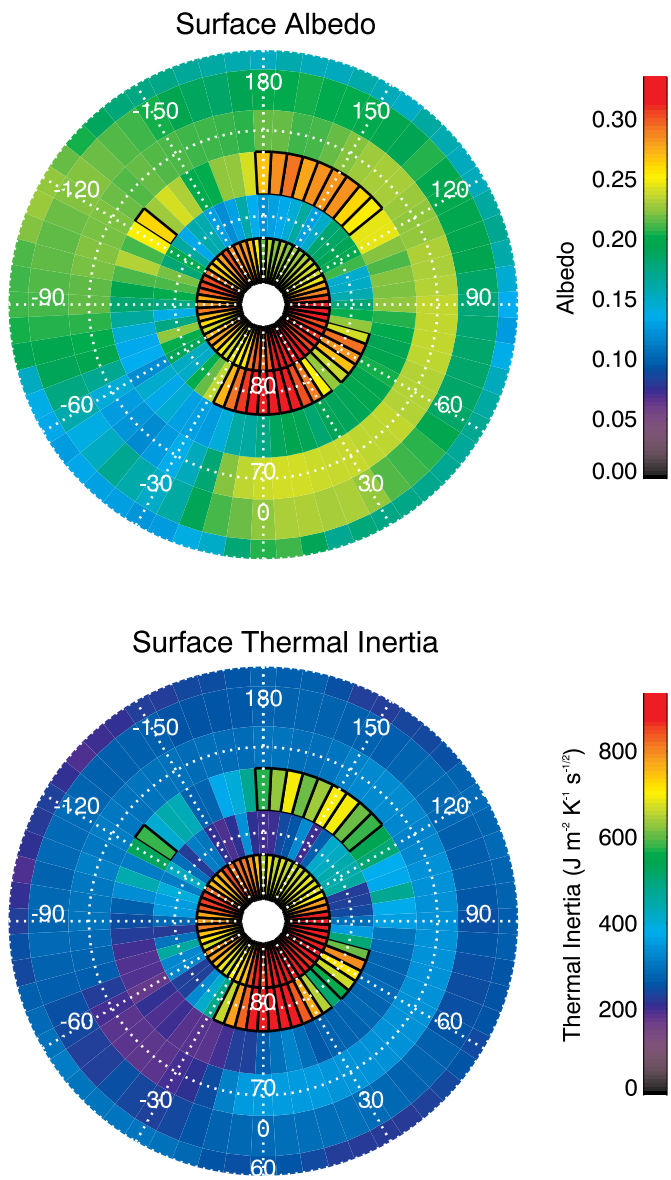

Fig. 2.2. Model albedo (top) and thermal inertia (bottom) of the NPRC region. Outlined grid boxes denote regions where the thermal inertia is above 550 SI units. These regions are sources for water in the model.

In the present version of the model we do not include the cold trapping effect of the SPRC. The SPRC is mainly frozen CO_2 such that any water vapor brought into contact with it will be permanently removed from the system. However, the magnitude of this sink is small compared to the supply from the NPRC and thus it has little effect on the global water cycle (see Montmessin et al., 2017 and references therein). Since we do not model this permanent sink, and since surface ice does not build up anywhere outside the NPRC, our equilibrated water cycle should be closed. Water lost from the NPRC during summer should be returned during winter. In practice, however, water is not precisely conserved in the model as there is a small net loss that amounts to about 1–2% per Mars year. We believe this loss is due to many factors (e.g., time differencing, smoothing, using separate timescales for dynamics and physics updates, etc.) but it is small enough not to affect our conclusions about the physical processes we've implemented in the model.

2.3. Ground temperature model

Temperatures within the ground are calculated by solving a generalized heat conduction equation with net surface energy fluxes for the top boundary condition and zero heat flux for the bottom boundary condition. The surface heat balance, which consists of radiative and convective fluxes, is satisfied using a Newton-Raphson iterative scheme to converge on a self-consistent solution for surface temperatures. Ground properties – density, heat capacity, and thermal conductivity – are allowed to vary with depth. The conduction equation is solved numerically using simple forward in time and centered in space finite differences. We presently run with 40 layers of variable thickness with the top layer thickness equal to ¼ of the diurnal skin depth and subsequent layers increasing in thickness by a factor of 1.2. Nominally, we take the diurnal skin depth to be 6 cm, which corresponds to a surface thermal inertia of 336 SI units, typical of Martian soils.

At the beginning of each run, we set temperatures within the ground to the annually averaged surface temperature of a run from an earlier version of the model. In practice, this introduces errors in the conduction term since the surface heat balance of the present run is not the same as the earlier run. However, since we run for many Mars years the error in surface temperatures due to deep soil conduction errors are small since the profiles down to an annual skin depth have had enough time to approach equilibrium.

There are two basic components of our ground temperature model: soil and ice. In each hemisphere ice is close to the surface at high latitudes and has a significant effect on heat conduction (e.g., Haberle et al., 2008). In the model, poleward of a longitudinally dependent specified latitude we assume ice is present in the ground below a depth of 5.45 cm in the northern hemisphere and 8.05 cm in the southern hemisphere. The longitudinally dependent latitude is based on Odyssey's Gamma Ray Spectroscopy observations of ground ice (Boynton et al., 2002; Feldman et al., 2004; Prettyman et al., 2004) and averages about 55° in each hemisphere. We assume that the ice in the southern hemisphere has a thermal conductivity representative of pure ice, while we arbitrarily lowered the conductivity of ice in the northern hemisphere to obtain a good match with observed surface temperatures in the NPRC region. Overlying the ice in both hemispheres is soil having the thermal inertia shown in Fig. 2.1. The properties of these components are listed in Table 2.1. The motivation for this two-component approach is to run with reasonable CO_2 ice emissivities, which would otherwise need to be lowered to unrealistic values to match to CO_2 cycle (see Haberle et al., 2008 for details).

2.4. PBL scheme

Our planetary boundary layer scheme (PBL) is based on the level 2

Table 2.1
Soil and ice properties in the ground temperature model.

	Density (kg m^{-3})	Specific heat (J kg^{-1} K^{-1})	Thermal conductivity (W m^{-1} K^{-1})	Thermal inertia SI
Soil	1500	627.9	Variable[a]	Variable[b]
SH Ice	1782	1404	2.00	2237
NH Ice	1782	1404	0.48	1100

[a] Calculated from thermal inertia in Fig. 2.1 using specified soil density and specific heat.
[b] Based on Fig. 2.1.

hierarchy of the Mellor and Yamada (1982) classification. We refer the reader to Haberle et al. (1993a) for its adaptation to Mars and to Haberle et al. (1999) for its implementation into the GCM. Briefly, turbulent mixing within the PBL takes place by diffusion with the diffusion coefficients dependent on the local bulk Richardson number. These coefficients are based on mixing length theory with stability functions taken from Arya (2001). Surface heat and momentum fluxes are parameterized from Monin-Obhukov similarity theory with the drag coefficients also dependent on the Richardson number using the formulations described in Savijärvi (1995) and Hourdin et al. (1995). For numerical stability we smooth the wind shear for the Richardson number calculation over a 3–6 h time scale. Because the scheme is diffusive, static instabilities can still develop in the presence of strong radiative forcing such as occurs during the day in tropical locations. While the model can run in such cases, for this work we perform a convective adjustment when the atmosphere is unstable to prevent unstable temperature profiles.

2.5. Sublimation physics

Surface ice deposits, both seasonal and permanent, are the only non-atmospheric reservoirs of water considered in the model at this time. Although the presence of an adsorbing regolith (Böttger et al., 2005) and hydrated surface materials (Martin-Torres et al., 2015) are reservoirs that could be exchanging water with the atmosphere on diurnal and seasonal time scales, we ignore their potential contributions in this work.

There are many prescriptions for calculating sublimation from surface ice deposits in the literature, but no clear indication of which approach is best. For Mars, the situation is further complicated by the fact that water vapor can significantly alter the air density and create a buoyancy driven flux that does not rely on mechanically or thermally driven turbulence (e.g., Ingersoll, 1970; Hecht, 2002). To keep things simple, we use a standard bulk transfer equation such as that described by Brutsaert (1982). Specifically,

$$E = -\rho u_* c_{dh}(q - q_{sat}) \tag{1}$$

where E is the upward sublimation flux, ρ is the air density, u_* is the friction velocity, c_{dh} is a drag coefficient defined as.

$$c_{dh} = (F_h)^{1/2}\frac{k}{\ln\left(\frac{z}{z_0}\right)} \tag{2}$$

q is the water vapor mass mixing ratio, and q_{sat} is the saturation mass mixing ratio. F_h is a bulk Richardson Number (*Rib*) dependent coefficient $= (1 - 64Rib)^{1/2}$, k is von Karman's constant (0.4), and z and z_o are the height of the midpoint of the first layer (~5 m), and roughness length respectively. Sensitivity studies with the model showed a weak dependence of friction velocities on surface roughness so for ice-free surfaces we adopt a constant value of $z_o = 1$ cm. For ice-covered surfaces (both CO_2 or water) we assume a smoother surface and use $z_o = 0.01$ cm. However, for sublimation this is clearly an oversimplification that needs more careful consideration in the future. The density, friction velocity, and water vapor mixing ratio are evaluated from variables predicted at the midpoint of the lowest layer, while the saturation mixing ratio is evaluated using the predicted surface temperature. Note that the use of Eq. (1) allows for both upward and downward fluxes.

The potential sublimation rate as a function of surface temperature for conditions typical of the NPRC based on our bulk transfer approach is shown in Fig. 2.3. For the range of surface temperatures expected for the NPRC (~200–250 K) during the peak sublimation season (L_s ~120°) the maximum sublimation rate varies between near zero and 700 μm sol^{-1}. The dependence on surface temperature is highly nonlinear in this regime, which emphasizes the importance of accurate simulations of surface temperature. However, since we do not include

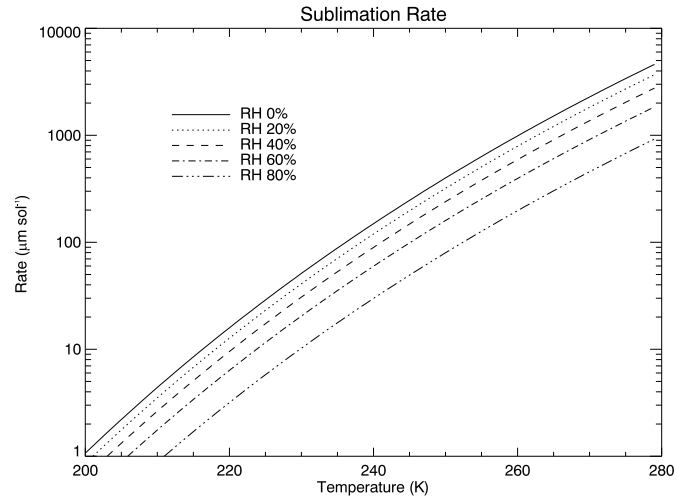

Fig. 2.3. Temperature dependence of the sublimation rate (μm sol^{-1}) for several relative humidities (RH).

sublimation by buoyancy-driven free convection, we may be underestimating the sublimation flux. Several previous studies have included both buoyancy-driven free convection and forced convection in calculating the sublimation flux (e.g., Haberle and Jakosky, 1990; Williams et al., 2008; Dundas and Byrne, 2010). This is a source of uncertainty in our simulations.

2.6. Cloud microphysics

The cloud microphysics scheme includes the processes of nucleation, growth, and gravitational settling of water ice particles. Discussion of these processes for Mars, and expressions used to calculate them are given in Michelangeli et al. (1993), Colaprete et al. (1999), Montmessin et al. (2002, 2004), Määttänen et al. (2005), and Jacobson (2005).

2.6.1. Nucleation

Nucleation is the process where water vapor molecules first cluster into an icy nucleus. When that nucleus reaches a critical size, further growth reduces the free energy of the system thereby enabling continued growth by condensation. This can occur homogeneously (the molecules cluster among themselves), or heterogeneously (they form on insoluble IN). Considering the relative inefficiency of homogeneous nucleation (a saturation ratio > 1000 is required to initiate it, see Montmessin et al., 2002; Määttänen et al., 2005), we only consider heterogeneous nucleation as dust particles in the Martian atmosphere should provide an ample supply of IN. This assumption is supported by laboratory experiments on Martian dust analogs, which indicate a good compatibility of dust for hosting water IN (Iraci et al., 2010).

The nucleation rate, i.e. the number of particles reaching the critical size for growth per unit time, is a complicated function of the IN radius a, temperature T, contact angle m, and the number density of water molecules n_{H_2O}. It is given by.

$$n(a, R, m, S) = \frac{ZkTr_*^2 4\pi(n_{H_2O}a)^2}{F\left(m, \frac{a}{r_*}\right)n_{us}m_0}\exp\left(-\frac{\delta F}{kT}\right) \tag{3}$$

where Z is the Zeldovitch factor, k is the Boltzman constant, r_* is the critical germ radius, n_{H_2O} is the number of water molecules per unit volume, F is a function of the contact angle and ratio of a/r_*, and n_{us} and m_0 are the jump frequency and weight of a water molecule, respectively. The change in free energy, δF, includes the molecular desorption energy and the molecular energy of surface diffusion. (See Montmessin et al. (2002), Pruppacher and Klett (1997), Keesee (1989), and Zent and Quinn (1997), and Seki and Hasegawa (1983) for details.)

Nucleation does not begin until the atmosphere is saturated with respect to ice, i.e., until the super saturation $S = s - 1$ exceeds a critical value S_{crit}, where $s = e/e_s$ with e being the vapor pressure and e_s being the saturation vapor pressure at temperature T. Typically, $S_{crit} \sim 1$ in the case of an infinite flat substrate. However, the finite and usually spherical shape of dust particles induces a curvature effect (also known as the Kelvin effect) that adds a surface tension energy barrier to nucleation. Typically, dust particles with radii smaller than 0.01–0.1 µm are unable to overcome the curvature effect, making nucleation as difficult as in the homogeneous case. In our simulations, we allow the model to self-consistently determine the dust particle (IN) sizes, air temperature, and the number density of water molecules, but we specify the contact angle to be constant and fixed at 0.975, which is the value estimated by Michelangeli et al. (1993) for pre-activated dust particles (i.e., those that have previously had ice formed on them). Although there is some indication from laboratory work that the contact angle is temperature dependent (Iraci et al., 2010), we did not obtain good results with a temperature dependent contact angle so we leave it as a constant in this work.

The nucleation rate is very sensitive to many of the dependent variables. The sensitivity to temperature, for example, is shown in Fig. 2.4. In this example, the nucleation rates are integrated over a log-normal particle size distribution with an effective radius and variance of 1.5 µm and 0.1, respectively. As Fig. 2.4 clearly illustrates, nucleation rates change by orders of magnitude for small changes in temperature and super saturation. At 180 K, a typical temperature in the ACB, nucleation rates increase by almost six orders of magnitude for super saturations ranging from 1.16 to 1.2 and by five orders of magnitude for a 10 K increase in temperature at a super saturation of 1.16. The hypersensitivity of nucleation rates and the very short time scales (seconds) they operate on pose a significant challenge for models, which we discuss later in Section 2.11.

2.6.2. Growth

Once particles are nucleated, growth occurs by molecular and thermal diffusion of water vapor through a background CO_2 gas. We neglect coagulation as the cloud particle concentrations we predict are too small for this to be important. We also neglect the surface kinetics effect whereby vapor molecules diffuse across the crystal surface before reaching a stable site (MacKenzie and Haynes, 1992). Experimental data for this mechanism are lacking for Mars environmental conditions, though we recognize that this could be important effect. The growth rate of an ice crystal of radius r is thus given by

$$r\frac{dr}{dt} = \frac{s - s_{eq}}{R_d + R_h} \tag{4}$$

where s_{eq} is the equilibrium saturation ratio accounting for the curvature (Kelvin) effect,

$$s_{eq} = \exp\left(\frac{2\sigma_{vi} m_{H_2O}}{kT\rho_i r}\right) \tag{5}$$

and R_d and R_h are "resistances" given by

$$R_d = \frac{\rho_i kT}{D' m_{H_2O} e_s(T)} \tag{6}$$

$$R_h = \frac{L_i \rho_i}{KT}\left(\frac{L_i m_{H_2O}}{kT} - 1\right) \tag{7}$$

In these equations, $\sigma_{vi} = 0.001(141.0–0.15\,T)$ is the temperature-dependent surface tension of the ice/vapor interface, ρ_i is the density of ice, D' is a corrected diffusion coefficient, m_{H_2O} is the molecular weight of a water molecule, $e_s(T)$ is the saturation vapor pressure at temperature T, L_i is the latent heat of sublimation (vapor to ice), and K is the thermal conductivity of air (CO_2 gas).

The flux of water vapor to ice crystals depends on the nature of the flow, which can be characterized in terms of the Knudsen number, K_n (the ratio of the mean free path to crystal size). In the continuum regime, $K_n < 1$, the flow is diffusive; in the kinetic regime, $K_n > 1$, molecules follow ballistic trajectories. For Mars, both regimes exist with the kinetic regime dominating at higher altitudes. To account for these differences we modify the molecular diffusion coefficient.

$$D = \frac{\frac{1}{3}\left(\frac{8kTn_a}{\pi m_{H_2O}}\right)^{\frac{1}{2}} kT}{\pi p (r_{CO_2} r_{H_2O})^2 \left(1 + \frac{m_{H_2O}}{m_{CO_2}}\right)^{\frac{1}{2}}} \tag{8}$$

by dividing it by a factor $(1 + \lambda K_n)$ where

$$\lambda = \frac{\frac{4}{3} + \frac{0.71}{K_n}}{1 + \frac{1}{K_n}} \tag{9}$$

In Eq. (8) p is pressure, n_a is Avogadro's number, and r_{CO_2} and r_{H_2O} are the radii of a CO_2 and water molecule, respectively. Hence, D' in Eq. (6) is $= D/(1 + \lambda K_n)$.

Growth rates are most sensitive to temperature and we show this sensitivity in Fig. 2.5 for a 1.5 µm particle at 100 Pa, a typical altitude in the ACB. For all temperatures the greatest sensitivity is at low super

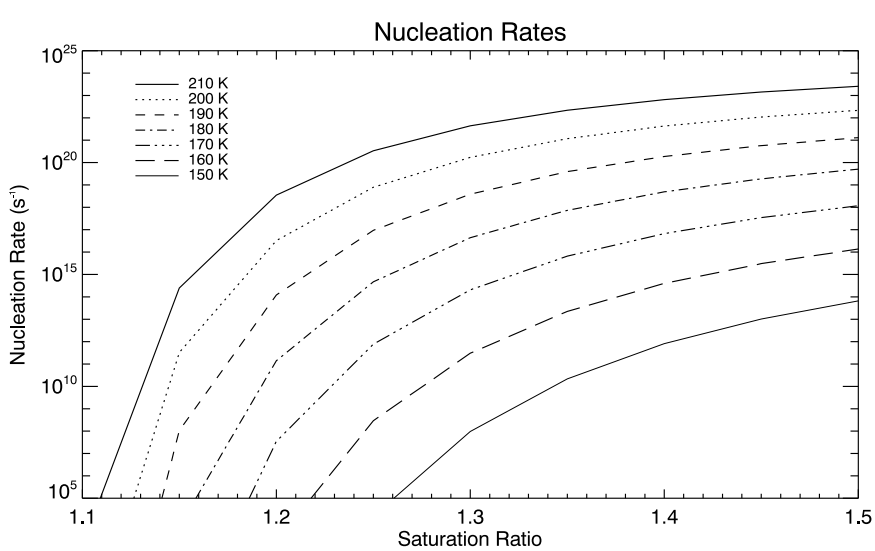

Fig. 2.4. Nucleation rate (number of particles per second) for 1 µm particles as a function of saturation ratio for several different temperatures.

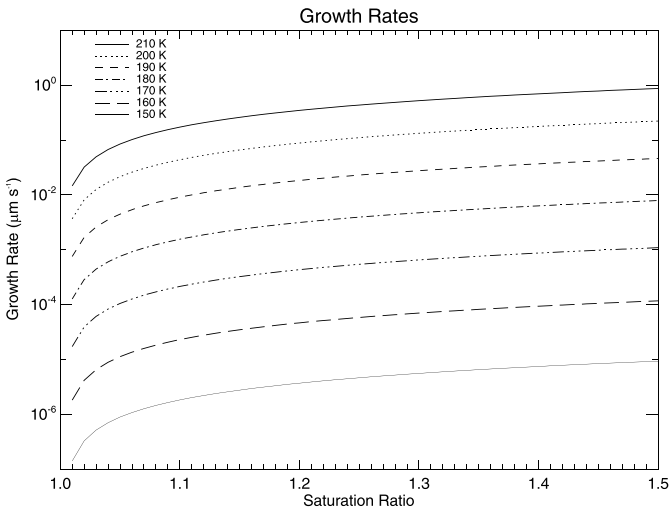

Fig. 2.5. Growth rate (μm s^{-1}) for 1 μm particles at the 100 Pa pressure level as a function of saturation ratio for several different temperatures.

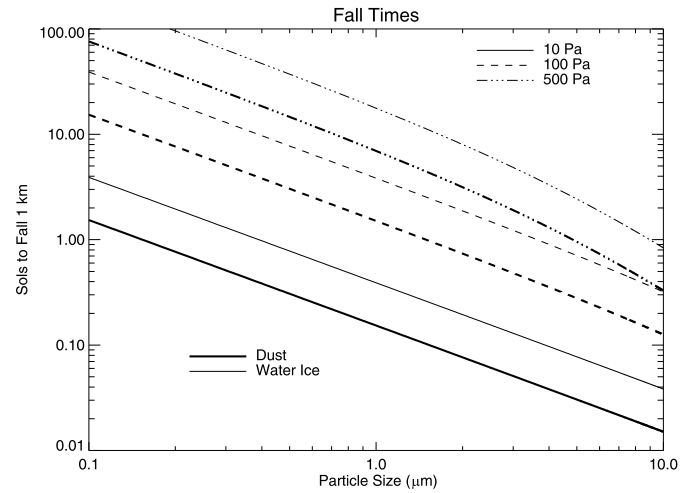

Fig. 2.6. Dust and ice particle fall times from several different pressure levels as a function of particle size. Y-axis gives the time (in sols) to fall 1 km.

saturations (< 1.05). A 10 K temperature change either way at 180 K changes the growth rate by about an order of magnitude. In this example, a 1.5 μm droplet would double its size in about 25 min at 180 K and 1.1 super saturation.

2.6.3. Sedimentation

Sedimentation is based on the standard Stokes-Cunningham relationships for particle fall velocity (v_f) with the slip correction for the thin Martian atmosphere and is given by.

$$v_f = \frac{2gr^2\rho_p}{9\vartheta_a}(1 + \alpha K_n) \tag{10}$$

where g is gravity, ρ_p is the particle density, ϑ_a is the dynamic viscosity of air, and.

$$\alpha = 1.246 + 0.42\exp\left(\frac{-0.87}{K_n}\right) \tag{11}$$

is the Cunningham slip-flow correction. We reduce this fall velocity by an amount equivalent to the vertical turbulent mixing computed in the planetary boundary layer algorithm. The settling fluxes are then computed and their divergences are used to advance the fields using either an explicit or an implicit time integration depending on the fall velocity (if the particles fall through more than one layer in a single time step we use the implicit scheme).

For reference, we show the settling times for dust and ice particles in Fig. 2.6. For a given size, dust particles fall faster than ice because of their greater density. A 1.5 μm ice particle takes about a quarter of a sol to fall 1 km at 10 Pa while a dust particle falls that far in only a couple of hours. Closer to the surface these fall times increase considerably being about 10 sols at 500 Pa for ice and about half that for dust. Overall, the settling times (h) are longer than the growth times (min), which are longer than the nucleation times (s). Thus, there is a wide range of microphysical time scales that must be considered.

2.6.4. Implementation

As described in the following Sections 2.7 and 2.8 we use a log-normal based moment scheme for atmospheric tracers where the tracer mass and number mixing ratios are the transported quantities. Except for nucleation, all cloud microphysical processes are calculated using representative radii computed from these mixing ratios. Nucleation rates, however, are calculated in particle size space. The free-dust (i.e., available IN) mass and number mixing ratios are converted into a log-normal size distribution and divided into an arbitrary number of size bins ranging from 0.1 to 100 μm. Separate 1-D tests show that 4 size bins are adequate for computing total nucleation rates as more size bins did not significantly change the results. The altered size distribution is then converted back into a mass and number mixing ratio, which are then transported at the next time step.

2.7. Atmospheric tracers

For trace gases, such as water vapor, transport is accomplished directly through the transport algorithms, which solve a mass conserving continuity equation with the modifications described in the Section 2.11. For size-dependent aerosols, such as dust and/or water ice particles, we have studied two methods: a bin method and a moment method. In the bin method tracers are discretized into size bins and each bin is transported separately. In the moment method a size distribution is assumed and its moments (mean, variance, etc.,) represent the actual distribution (e.g., Rodin, 2002). The bin method is generally more accurate and self-consistent provided the size distribution is adequately resolved. The moment method, however, is much more computationally efficient. The choice of which method to use is application specific. We have previously used the bin method to study dust particle size evolution (Kahre et al., 2008). Here we employ the moment method.

We assume that size-dependent aerosols have a log-normal distribution

$$n(r)dr = \frac{1}{r\sigma_o\sqrt{2\pi}}\exp\left[\frac{1}{2}\left(\frac{\ln(r/r_o)^2}{\sigma_o}\right)\right] \tag{12}$$

where n(r)dr is the number of particles per unit volume with radii between r and r + dr, r_o is the median radius, and σ_o is the standard deviation. It then follows that the number of particles N between r_{min} and r_{max} is

$$N = N_o\int_{r_{min}}^{r_{max}} n(r)dr = \frac{N_o}{2}\left[\mathrm{erf}\left(\frac{\ln(r_{max}/r_o)}{\sqrt{2\pi\sigma_o}}\right) - \mathrm{erf}\left(\frac{\ln(r_{min}/r_o)}{\sqrt{2\pi\sigma_o}}\right)\right] \tag{13}$$

where N_o is the total number of particles. Thus, the values of r_o, σ_o, and N_o fully describe a log-normal distribution. However, r_o can also be expressed in terms of the mass M_0 of particles per unit volume

$$M_o = \frac{4}{3}\pi\rho N_o r_o^3 exp(4.5\sigma_o^2) \tag{14}$$

where ρ is the particle's density. Solving for r_o gives

$$r_o = \left(\frac{3M_o}{4\pi\rho N_o}\right)^{1/3} \exp(-1.5\sigma_o^2) \tag{15}$$

which means that M_0, σ_o, and N_0 can also fully describe a log-normal distribution. We further simplify this approach by specifying σ_o for each species: 0.63676 for dust particles and 0.30870 for ice particles. These choices give an effective variance of 0.5 and 0.1 for dust and ice, respectively.

Thus, we carry two quantities for each tracer of interest: mass M_0 and number density N_0. In practice, we transport these as mixing ratios defined as the ratio of the mass (number) of aerosol to the mass of air. At present we carry six tracers: a dust mass and number mixing ratio, a water ice mass and number mixing ratio, a water vapor mass mixing ratio, and a dust core mass mixing ratio. The latter allows us to keep track of dust incorporated into ice particles and does not require a number mixing ratio since in the absence of homogeneous nucleation, a process we neglect in this work, the number of dust cores is equal to the number of ice particles. We do not need to carry a water vapor number mixing ratio since water vapor is not a size-dependent tracer.

2.8. Particle radii and bin/moment tests

Another computational advantage of the moment scheme is that physical processes, such as gravitational settling or growth, can be computed using a single particle size rather than integrating over a distribution, provided it is appropriately weighted. In practice, however, derivation of weighted radii is not always straightforward due to the complexity of the functions to be weighted. This is especially true for sedimentation and growth whose actual dependence on radius is quite complicated and for which analytical derivations are not possible without making simplifying assumptions. These simplifications introduce errors, of course, and we assess these below. Table 2.2 lists the moment radii we use for various size-dependent physical processes in the model.

For sedimentation we derive the weighted mass and number radius, $r_{sed,m}$ and $r_{sed,n}$ respectively (see Table 2.2), by neglecting the weak particle size dependence of the Cunningham-slip flow correction factor in Eq. (11). We then compare the sedimentation fluxes calculated from Eq. (10) using $r_{sed,m}$ and $r_{sed,n}$ with those computed from a bin model having more than enough bins to resolve the size distribution. But first we show in Fig. 2.7 that > 100 bins are required for an accurate simulation of the sedimentation flux, which obviously makes this approach infeasible for a GCM. However the errors introduced by the moment method, shown in Fig. 2.8, are quite small when compared to asymptotic bin solutions. They are essentially zero except for particles in the ~5–150 μm size range. In this range the errors grow and then decrease because the Cunningham slip flow correction has a transition regime for intermediate sized particles. The location of this transition varies with altitude through the Knudsen number. For the expected range of particle sizes and pressures, however, maximum errors are always < 2% and are thus quite tolerable.

Errors for growth rates, on the other hand, are more substantial. We derive the appropriate radius for the growth rate (Eq. (4)) by noting that $dr/dt \sim r^{-1}$. This assumption leads to the volume mean radius (r_v in Table 2.2) as the appropriate choice. In reality the diffusive resistance, R_d in Eq. (6), has a very complicated dependence on particle size (because of its dependence on the Knudsen Number) that renders this simple assumption not strictly valid. This can be seen in Fig. 2.9 where the asymptotic bin solutions, which still require > 100 bins for accuracy, are notably less than those from the moment method. For the size ranges of interest (1–50 μm), the errors are about 50% (Fig. 2.10). We discuss the implications of this error in Section 5.1.

Table 2.2
Radii for the moment scheme.

Process	Symbol	Formula
Nucleation	r_o	$\left(\frac{3M_o}{4\pi\rho N_o}\right)^{1/3} \exp(-1.5\sigma_o^2)$
Growth[a]	r_v	$r_o \exp(1.5\sigma_o^2)$
Sedimentation	$r_{sed,\ m}$	$r_o \exp(4.5\sigma_o^2)$
	$r_{sed,\ n}$	$r_o \exp(1.5\sigma_o^2)$
Opacity (total geometric cross-section)	r_s	$r_o \exp(\sigma_o^2)$
Scattering properties	r_{eff}	$r_o \exp(2.5\sigma_o^2)$

[a] Number growth rates are not necessary since growth does not change the number of particles.

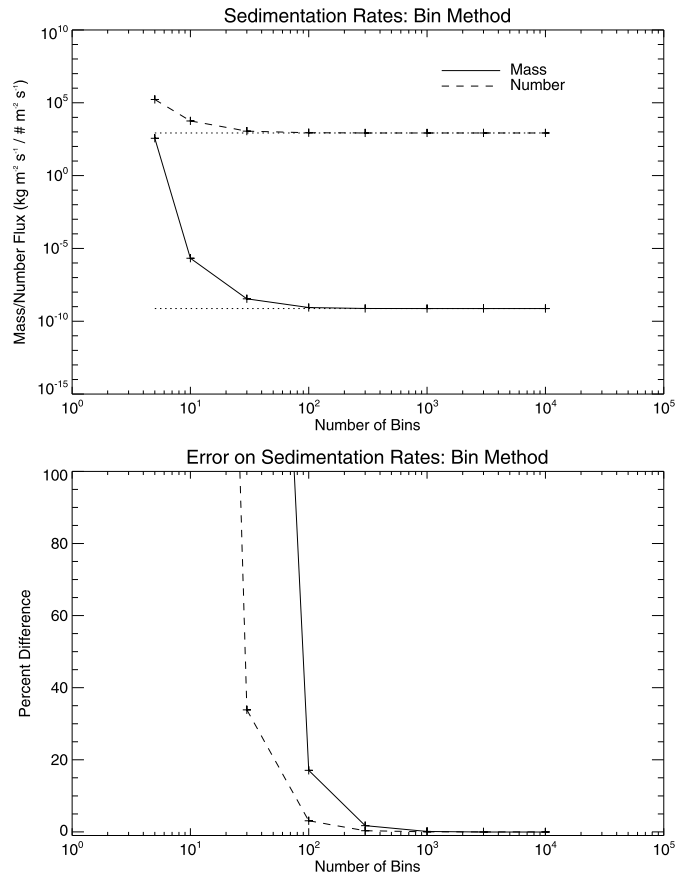

Fig. 2.7. Mass and number sedimentation fluxes at 10 Pa and a temperature of 180 K as a function of the number of bins. Median radius = 1.58 μm, effective variance = 0.5.

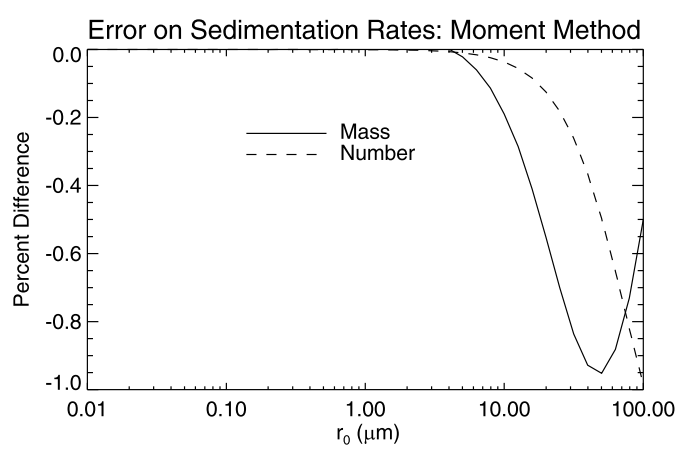

Fig. 2.8. Moment method errors for sedimentation as a function of median particle size. Effective variance = 0.5, P = 10 Pa, T = 180 K.

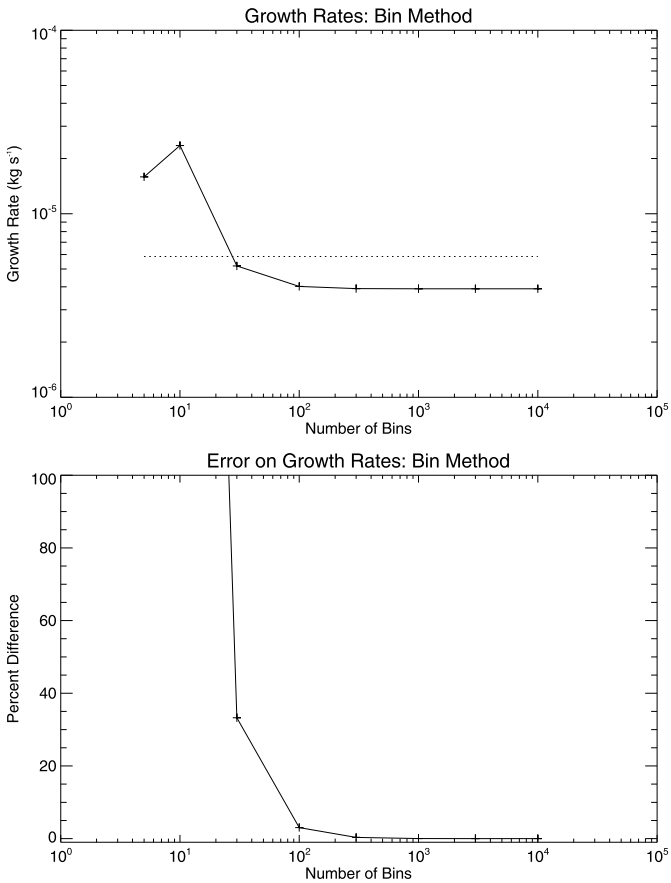

Fig. 2.9. Top: Bin method growth rates as a function of the number of bins. Dashed line is the moment method. Bottom: Bin method error compared to its asymptotic solution. Median radius = 1.58 μm, effective variance = 0.5, P = 10 Pa, T = 180 K.

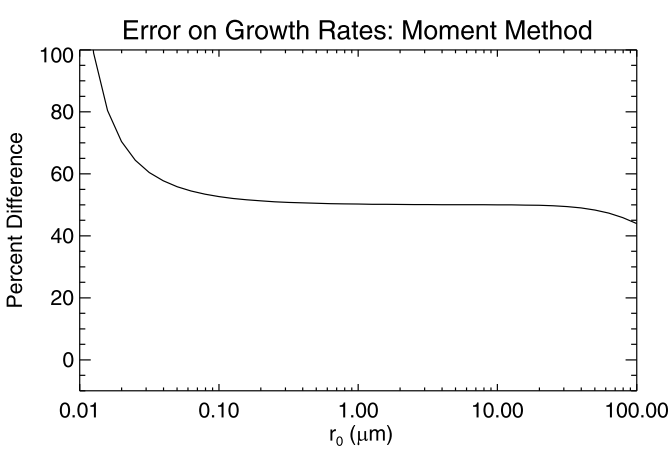

Fig. 2.10. Moment method growth rate errors as a function of median particle size. Errors are compared to asymptotic bin solutions. Effective variance = 0.5, P = 10 Pa, T = 180 K.

2.9. Dust opacity maps

The most important diabatic forcing term for Mars GCMs is radiative heating by suspended dust particles. There are many approaches for handling this term ranging from simply specifying the column dust optical depth (e.g., Haberle et al., 1993b; Forget et al., 1998; Richardson and Wilson, 2002) to allowing the model to lift dust off the surface and be transported by the predicted large-scale wind field (Newman et al., 2002a, 2002b; Basu et al., 2004; Kahre et al., 2006, 2008). Ideally, the latter approach is best but it does not yet lead to accurate simulations of the dust cycle (e.g., Kahre et al., 2017).

In this work we implement a hybrid approach that is designed to track observed column opacities and therefore provide realistic latitude/longitude spatial variations in the forcing, yet permit radiative/dynamical interactions, which are so critical for determining the depth and vertical distribution of the dust. The observed opacities are taken from the daily gridded 9.3 μm absorption maps constructed by Montabone et al. (2015). These maps, which are available at http://www-mars.lmd.jussieu.fr/mars/dust_climatology/index.html, were constructed from a variety of data sets (TES, THEMIS, MCS) using an iterative procedure weighted in space, time, and retrieval quality. They cover ten Mars Years from MY 24–33. The daily maps are produced on 3° × 3° latitude/longitude grids, which we bin into a 5° × 6° grid in space, and a 6° L_s bin in time. Thus, for a single year we have 60 maps of the observed 9.3 μm opacity at 5° × 6° resolution. During a simulation we track these maps assuming the opacity varies linearly in L_s from one map to the next.

The results presented here are based on the MY 24 map which, because TES began operations around L_s 100°, is a hybrid of averages from MY 25–26 for Ls 0 to ~100° and observations from MY 24 from L_s ~100 to 360°. This was a year without a global dust storm and is therefore representative of a "typical" Mars year, though we note there are still non-trivial variations from year to year (e.g., Kass et al., 2016). Our tracking algorithm compares the model-predicted column dust visible opacity at each grid point with that from the dust map (converted to a visible opacity as described below). If the predicted opacity is less than the map opacity we lift dust from the surface into the lowest model layer at a rate equivalent to increasing the column opacity by 0.2 per sol. The lifting is distributed over a log-normal size distribution with an effective mean particle size and variance of 2.0 μm and 0.5, respectively. Tests show that this lifted size distribution gives global mean effective particle sizes of ~1.5 μm which is consistent with those derived by Wolff et al. (2009). And the predicted column 9.3 μm opacities are very similar to the observed map (Fig. 2.11).

The lifted dust is radiatively active, serves as IN for the cloud microphysics scheme, and is transported by model winds. Thus, once in the atmosphere the dust fields are self-consistently determined, avoiding the need to specify a vertical distribution. Given that our dust fields track the 9.3 μm dust absorption feature and our radiation code is keyed to a visible extinction optical depth, we multiply our simulated 9.3 μm opacity by $Q_{ext}(vis)/Q_{abs}(IR)$, where $Q_{ext}(vis)$ is the extinction efficiency for our solar band between 0.4 and 0.8 μm, and $Q_{abs}(IR)$ is the absorption efficiency for our infrared dust band between 8 and 12 μm. In general, the extinction parameters are size and band dependent and are computed as described in Section 2.10. However, for a size distribution with an effective radius of 1.5 μm and variance of 0.5, $Q_{ext}(vis)/Q_{abs}(IR) = 3.67$, which is much larger than our earlier estimated value of 2.75.

2.10. Radiative heating/cooling rates

Radiative heating/cooling rates are calculated from fluxes generated from a two-stream solution to the radiative transfer equation. The two-stream solution is generalized for solar and infrared radiation as described in Toon et al. (1989) and is based on the δ-Eddington approximation at visible wavelengths and the hemispheric mean approximation at infrared wavelengths. Water vapor and CO_2 are the only radiatively active gases and their opacities are calculated from correlated-k distributions. Dust and water ice clouds are radiatively active aerosols whose optical properties depend on their predicted effective particle sizes and in the case of ice clouds, the fraction of dust in their cores.

We run with 12 spectral bands: 7 in the visible (0.24–4.5 μm), and 5 in the infrared (4.5–250 μm). Table 2.3 lists the band boundaries and

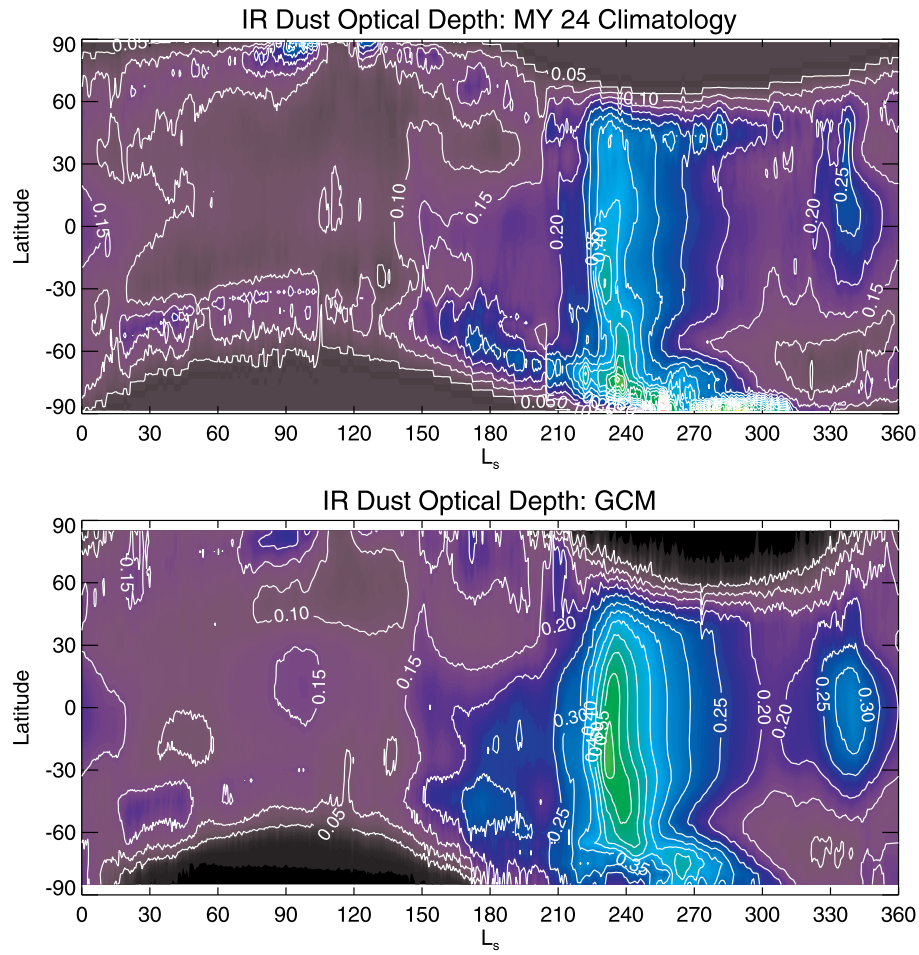

Fig. 2.11. Top: Observed zonal mean column IR dust opacity for a climatologically determined MY24. (Values after L_s 110° are from MY24; before L_s 110° they are averaged from MY25–27. See Montabone et al., 2015). Bottom: Simulated zonal mean column IR dust opacity using the tracking scheme described in the text.

solar fluxes. For the latter, we use fluxes from the 1985 Wehrli Standard Extraterrestrial Solar Irradiance Spectrum. The full spectrum can be downloaded from http://rredc.nrel.gov/solar/spectra/am0/. A blackbody at 5780 K produces an integrated flux over these intervals of 1359 Wm^{-2} at 1 AU compared to 1355 Wm^{-2} for the observed sun. In all spectral intervals the correlated-k's are generated for a binary mixture of CO_2 and water vapor from a line-by-line code using the HITEMP data base from HITRAN for CO_2, and a version of the Schwenke data base for H_2O (to include lines too weak to appear in HITRAN). The lines are assumed to be Lorentzian throughout and are truncated according to.

$$W = W_o\left(\frac{P}{P_o}\right)\sqrt{\frac{296}{T}} \tag{16}$$

where W is the truncation width, $W_o = 25\,cm^{-1}$, P is pressure in atmospheres, P_o is a reference pressure (=1 atm), and T is temperature. W is never less than W_o, so the lines are never truncated at $< 25\,cm^{-1}$. The absorption coefficients are sorted, reordered in g space (cumulative probability space), and stored in a look-up table on a $7 \times 11 \times 10$ temperature (T), pressure (P), and water vapor volume mixing ratio (Q_{H2O}) grid with T = (50, 100, 150, …, 350) K, P = (10^{-4}, 10^{-3}, …, 10^{6}) Pa, and Q_{H2O} = (10^{-7}, 10^{-6}, …, 10^{-1}, 0.2,0.3,0.4). Actual values are linearly interpolated from this table (linear in log space for pressure). An example of k-distributions produced in this manner for the 15-

Table 2.3
GCM spectral intervals and solar fluxes.

No	GCM Band	Wavelength Interval (μm)	Solar Flux @ 1 AU (Wm^{-2}) for a BB Sun @ 5780 K	Obs Solar Flux @ 1 AU (Wm^{-2})/comment
1	Vis - 7	0.24–0.40	158	118
2	Vis - 6	0.40–0.80	630	643
3	Vis - 5	0.80–1.31	349	348
4	Vis - 4	1.31–1.86	123	148
5	Vis - 3	1.86–2.48	51	52
6	Vis - 2	2.48–3.24	24	29
7	Vis - 1	3.24–4.50	14	17
8	IR - 5	4.50–8.00	7.7	- neglected
9 (dust band)	IR - 4	8.00–12.0	1.3	- neglected
10 (15-μm CO_2 band)	IR - 3	12.0–24.0	0.9	- neglected
11	IR - 2	24.0–60.0	0	- neglected
12	IR - 1	60.0–1000	0	- neglected

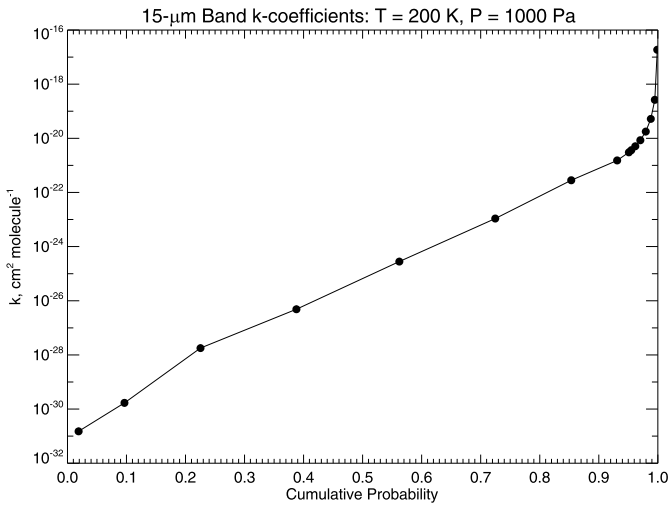

Fig. 2.12. Cumulative distribution of the k-coefficients in the 15-μm CO_2 band.

μm CO_2 band is shown in Fig. 2.12.

Scattering properties for aerosols (Q_{ext}, Q_{scat}, and g) are computed off line with a core/mantle Mie code and are also stored in a look-up table. As shown in Fig. 2.13 we use the Warren (1984) refractive indices of water ice and the Wolff et al. (2009) indices for dust. For each spectral interval, the Planck-weighted (215 K in IR; 6000 K in VIS) properties are computed for 20 mono-disperse populations with sizes ranging from 0.1 to 50 μm, and for 15 cloud/dust volume ratios ranging from 0.1 to 0.99. The spectral dependence of the dust and cloud single scattering albedo for several particle sizes is shown in Fig. 2.14. At each heating rate time step in the GCM we compute the effective particle size from the current mass and number mixing ratios, construct the corresponding particle size distribution, transform it into bin space, and weight the scattering properties by the total cross-sectional area in each bin. These are then summed over all size bins and divided by the total

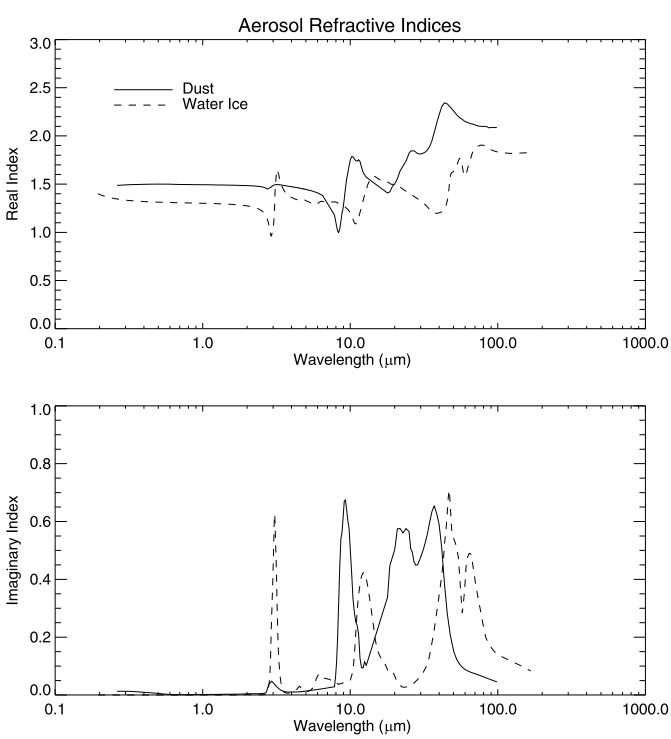

Fig. 2.13. Wavelength dependence of the real (top) and imaginary (bottom) refractive indices for dust (Wolff et al., 2009) and ice (Warren, 1984).

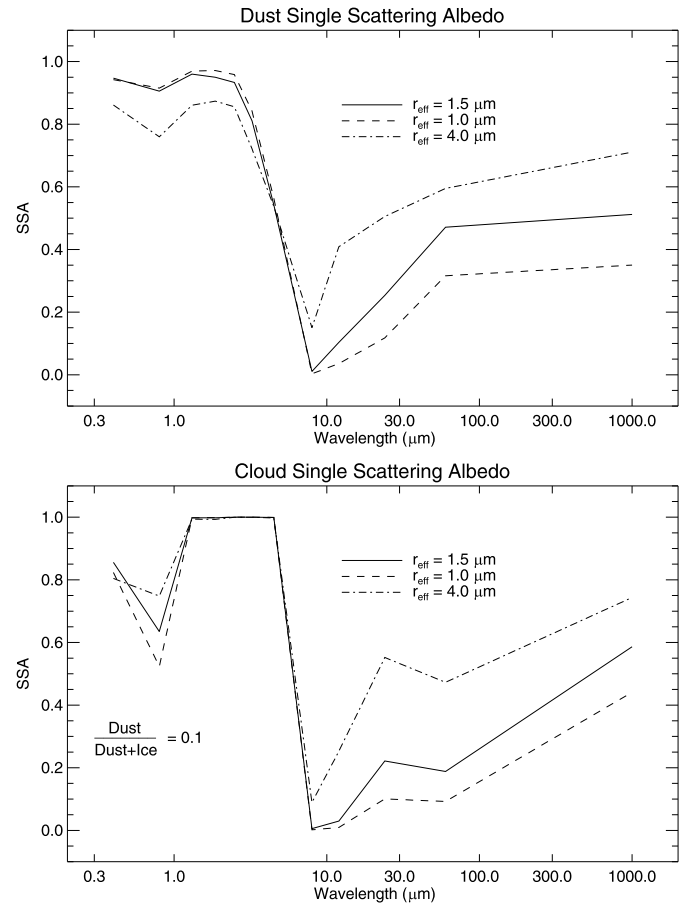

Fig. 2.14. Wavelength dependence of the single scattering albedo for dust (top) and cloud (bottom) for several effective particle sizes. Cloud particles consist of a dust core with an icy mantle. The ratio of core radius to total particle radius is 0.1.

cross-sectional area to obtain the final scattering properties used in the two-stream code. An example of the fluxes and heating rates is shown in Figs. 2.15 and 2.16, respectively.

2.11. Numerical changes and code structure

2.11.1. Modifications to C grid transport scheme

The Van Leer I scheme with slopes limitations is utilized in the dynamical core to account for tracer advection due to model resolved winds (Hourdin and Armengaud, 1999). The Van Leer I formulation is a finite-volume scheme that solves the flux form of the continuity equation to calculate the tracer flux across grid box boundaries. The subgrid-scale mass spatial distribution in each grid box is estimated by a first order polynomial (a slope) and is computed by finite differences of the tracer distribution in each spatial dimension (zonal, latitudinal and vertical). In order to ensure monotonicity, slopes are limited by the requirement that the entire tracer mass in a given grid box does not exceed the average value of the two adjacent grid boxes and that the sign of the slope in a grid box is the same as the slope in the two adjacent grid boxes.

Boundary flux calculations are performed sequentially in the three directions, with the two horizontal directions calculated before the vertical direction. The order of calculations for the zonal and latitudinal horizontal directions alternate back and forth each time the tracer transport scheme is called in the dynamical core.

An addition was implemented to the transport scheme in the zonal direction to account for advection of a tracer over more than one grid box in one time step. This situation tends to occur at high latitudes due

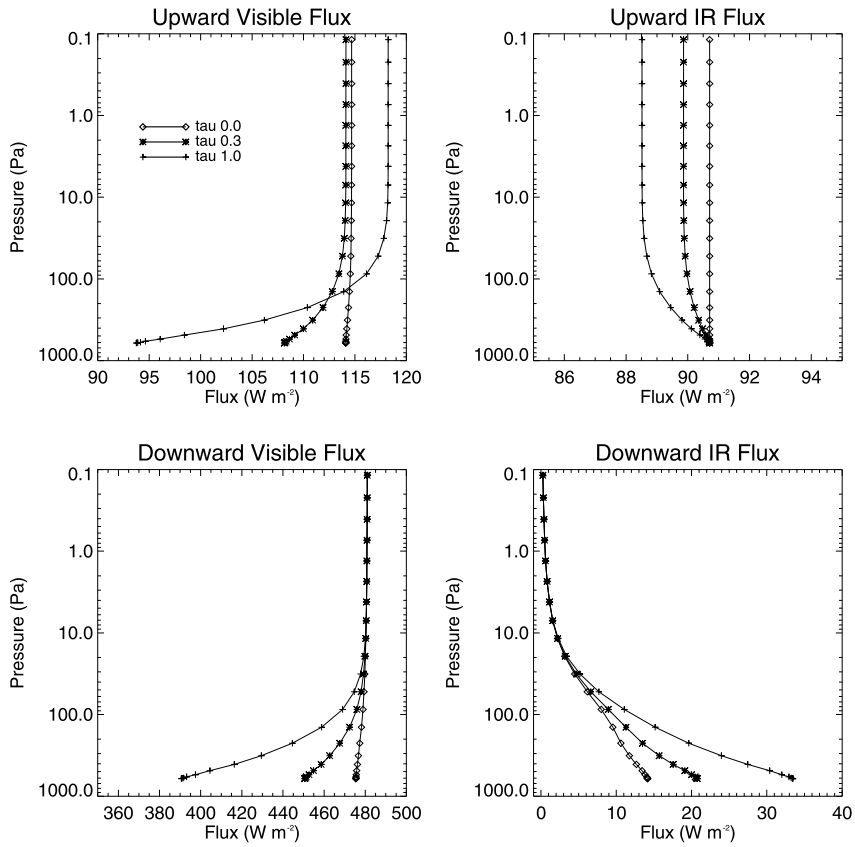

Fig. 2.15. Visible and infrared fluxes for several values of the dust optical depth in an isothermal atmosphere at 200 K with a near overhead sun. Top: upward fluxes. Bottom: downward fluxes.

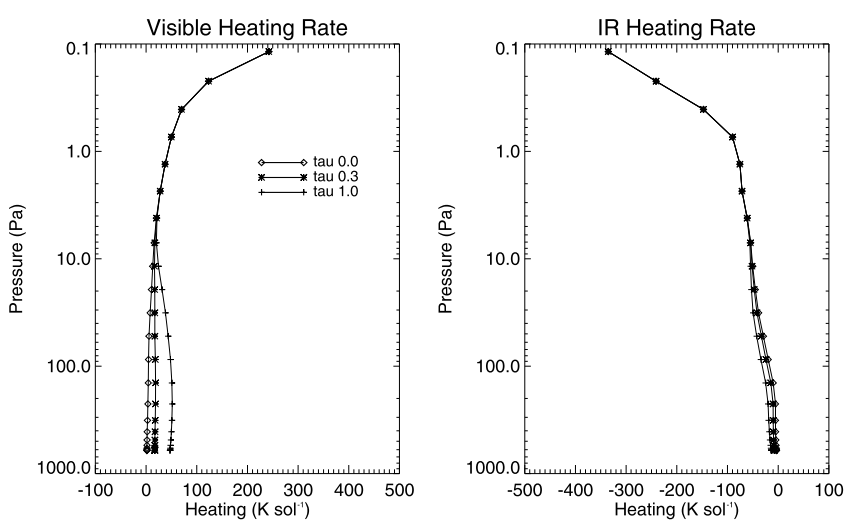

Fig. 2.16. Visible (left) and infrared (right) heating rates corresponding to Fig. 2.15.

to converging meridians. This modification utilizes the fact that the tracer mass flux across a boundary can be exactly calculated if the mass transfer due to wind is exactly equal to the mass of the upstream grid box. Specifically, the total tracer flux across a boundary when the wind at that boundary is strong enough to evacuate the upstream grid box plus some of the second upstream grid box is the sum of the tracer mass in the completely evacuated grid box and the slope scheme-computed flux from the second upstream grid box.

2.11.2. π-weighted potential temperature tendencies

The Goddard C-grid dynamical core formulates tendencies in terms of π-weighted dependent variables, where $\pi = p_s - p_t$, with p_s being a variable surface pressure and p_t a constant "tropopause" pressure. Because of this, subtle issues arise when the model is applied to planets with condensing atmospheres that if not properly addressed can lead to the introduction of spurious energy sources or sinks. Most importantly the diabatic heating term in the thermodynamic energy equation, which is cast in terms of potential temperature θ rather than physical temperature T, needs to account for changes in surface pressure to properly conserve energy. In the π-weighted formalism of the dynamical core this term can be expanded to show that

$$\frac{\partial(\pi\theta)}{\partial t}_{diabatic} = \theta\frac{\partial\pi}{\partial t} + \pi\left[\left(\frac{p_o}{p}\right)^{\kappa}\frac{\partial T}{\partial t}_{diabatic} - \kappa\frac{\theta}{p}\frac{\partial p}{\partial t}\right] \tag{17}$$

where t is time, p is pressure, p_0 a constant reference pressure, and $\kappa = R/c_p$ where R is the molar gas constant and c_p is the specific heat at constant pressure, and t is time.

In our model, diabatic heating rates are computed in terms of the physical temperature such that $(\partial T/\partial t)_{diabatic}$ in Eq. (17) is the total diabatic heating rate due to radiation, turbulence, convection, and latent heat release.

In non-condensing atmospheres, like Earth's, the first and last terms are zero and the p-weighted diabatic heating term for potential temperature is simply the physical temperature tendency multiplied by some pressure factors. However, in a condensing atmosphere neglect of these terms generates spurious results. For example, it is easy to show that these terms reduce to

$$\theta\frac{\partial\pi}{\partial t} - \pi\kappa\frac{\theta}{p}\frac{\partial p}{\partial t} = \theta\frac{\partial\pi}{\partial t}[1-\kappa] \tag{18}$$

Since κ is < 1, in a condensing atmosphere where $\partial\pi/\partial t < 0$ the sum of these two terms is negative. Thus, neglecting them will lead to spurious warming. The converse is true for sublimation when surface pressures are increasing.

To illustrate how important these terms are we show in Fig. 2.17 temperature profiles over the south polar cap during southern winter solstice from full 3-D GCM simulations with and without them included in the diabatic tendency equation. Without them temperatures are much warmer than with them, particularly in the lower atmosphere, which can be as much as 10 K warmer than the case including them. Early versions of our model did not include these terms and our polar temperatures were therefore too warm compared to observations. Including them, however, brings our polar temperatures in much better agreement with observations.

2.11.3. Diabatic calculations

The non-conservative tendencies based on the physics described above are calculated in a sequence of subroutines within the model. These tendencies include diabatic heating, frictional momentum changes, and tracer mixing ratio sources and sinks. The calculated tendencies are passed into the model driver routine, which updates all fields simultaneously due to both dynamical and physical processes. A flow diagram illustrating the basic physics modules and sequence of operations is shown in Fig. 2.18. Table 2.4 provides a brief description.

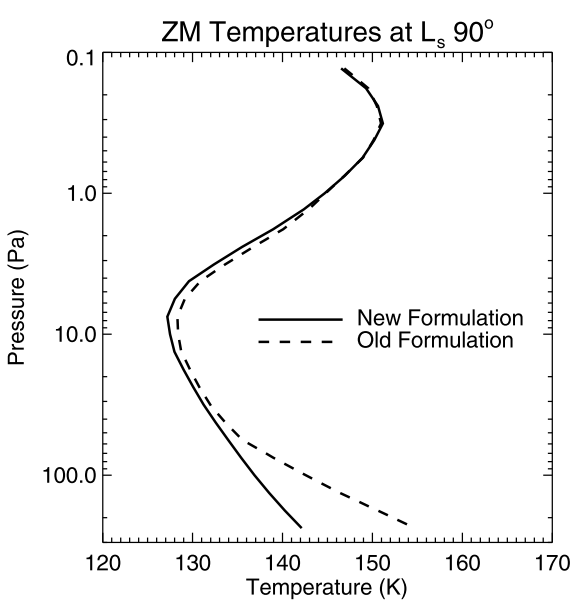

Fig. 2.17. Zonally averaged temperature profiles at 85°S and L_s 90° for a simulation with (solid) and without (dashed) the changes described in Section 2.11.2.

The sequence of operations is designed to maximize efficiency and minimize computing time. While the physics module is called every dynamical time step, nominally 2 min, only ground temperatures are updated at this frequency since they respond quickly to changes in the solar flux. While updating ground temperatures we allow for sun angle changes in the direct beam but hold the diffuse solar component and the downward IR constant at the value from the last physics pass. Updates using the full physics package are done every 8 dynamical time steps, though this is an adjustable parameter. For this case, ground temperatures are updated every 2 min, while those for all remaining fields are updated every 16 min.

We compute tendencies as the difference between the final and initial values divided by the length of a physics time step. Before a full pass through the physics module we store the initial values, update them sequentially in the order shown in Fig. 2.18, and then calculate tendencies at the end. The ordering of updates is somewhat intuitive in that radiation destabilizes the atmosphere, for example, and mixing is the response. Our PBL mixing scheme is diffusive in nature and hence does not completely eliminate instabilities. Thus, the last process in a full pass is convective adjustment. While we can run without convective adjustment, we have left it in until we can fully assess its impact.

This ordering of the physics modules has been the basis of our code since it was originally designed in the 1970's. The major new update is the insertion of the Cloud Microphysics module after the call to the Planetary Boundary Layer module. Importantly, the Cloud Microphysics module is embedded in a time splitting loop with ~ 30 s time steps to better represent the fast time scales of nucleation and growth. While models using implicit schemes can avoid such time-splitting loops (Lee et al., 2018) it is necessary for explicit schemes such as ours. Offline tests show that the number of nucleated dust particles produced in a NPRC like environment asymptotes with time to a single value for time steps approaching 10 s or less, and that the 30 s result is within a factor of two of that solution. This is consistent with the findings of Shaposhnikov et al. (2018) on the need for small time steps to accurately compute the nucleated population. Thus, with 30 s time steps we may still be overestimating somewhat the number of nucleated dust particles, but as explained below the result we seek – a relatively cloud free atmosphere over the NPRC – is still achieved. We also note that an important aspect of this time splitting loop is that we incrementally change the water vapor and temperature fields simultaneously with nucleation and growth. This helps avoid the large super saturations and near complete nucleation of the free dust population that leads to optically thick clouds over the NPRC.

2.11.4. Effect of time splitting

Achieving a cloud free atmosphere over the NPRC during summer has been a particularly vexing problem to solve. Clouds are not observed over the cap at this time of year (e.g., Wang and Ingersoll, 2002; Smith, 2002), yet early versions of our model with the full microphysics package and radiatively active clouds consistently predicted optically thick low lying clouds (fogs) over the cap that dried out the water cycle to unrealistic levels (see Haberle et al., 2011). Being close to the surface, the clouds reflected more sunlight back to space than they emitted to the surface in the infrared. Consequently, the surface cooled, evaporation declined, and the water cycle dried out.

Models with much simpler cloud schemes that do not simulate nucleation and growth can also have problems with thick polar clouds (see, for example, the "no microphysics" simulation in Navarro et al., 2014) which can be mitigated to some extent by arbitrarily limiting the number of IN available for cloud formation (Madeleine et al., 2012; Tyler and Barnes, 2014) or allowing high super saturations to develop before clouds can form (Urata and Toon, 2013). This suggests that there is something about the nucleation and growth process that is at the root

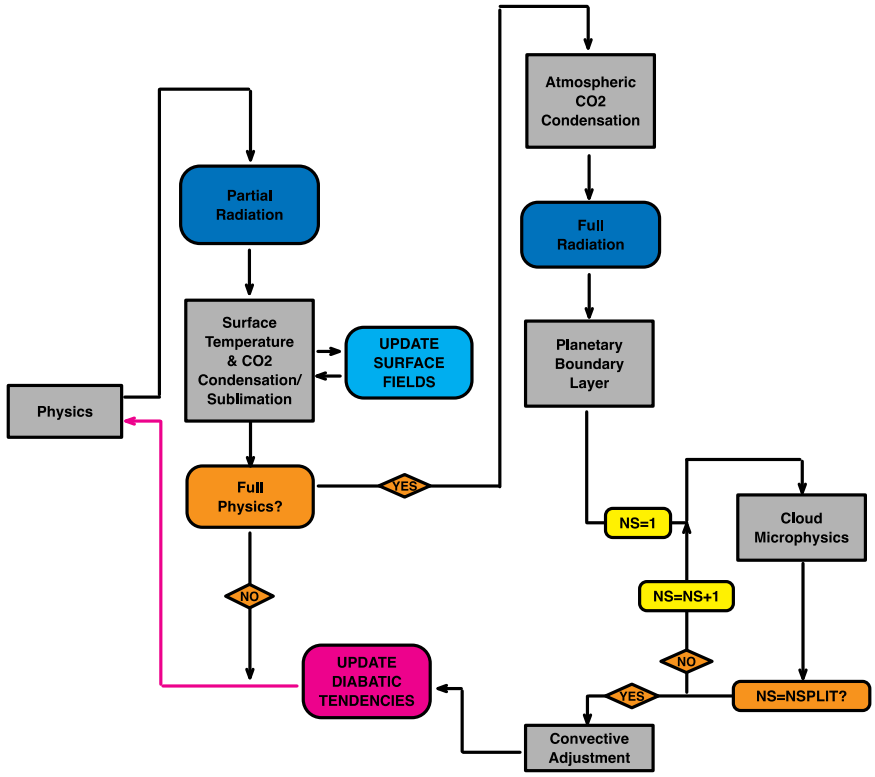

Fig. 2.18. Flow diagram for the diabatic calculations.

Table 2.4
Physics modules.

Module	Description	Comment
Partial radiation	Update the absorbed solar flux at the surface.	Direct beam term is updated. Diffuse solar component and downward IR are constant over a physics time step using value from previous time step.
Surface temperature and CO_2 condensation/sublimation	Calculate ground temperatures and update amount of CO_2 frost on the ground.	Solves a soil conduction equation with a full surface heat balance for the top boundary condition, and zero flux for the bottom boundary condition.
Atmospheric CO_2 condensation	Calculate atmospheric CO_2 condensation.	Based on latent heat needed to maintain frost point temperature. Condensed CO_2 deposited instantaneously on the ground.
Full radiation	Calculate solar and infrared heating/cooling rates.	Fluxes derived from a 2-stream model with opacities from correlated-k s.
Planetary boundary layer	Calculate surface heat, momentum, dust, and moisture fluxes, and atmospheric mixing.	Uses the level-2 scheme of Mellor and Yamada (1982).
Cloud microphysics	Update dust injection, calculate sedimentation, nucleation and growth rates.	Embedded in a time-splitting loop.
Convective adjustment	Perform a convective adjustment of the temperature, tracer, and momentum fields if needed.	Assumes dry adiabatic lapse rate and uniform mixing.

of the problem.

Navarro et al. (2014) found that the time step for nucleation and growth plays a critical role on the nature of polar clouds. With 15min time steps (that used for advancing the dynamical fields) the predicted cloud particle sizes were too small and hence optically thicker than they should be. In their model this led to local cooling which increased the super saturation and nucleated more particles leading to a positive feedback between cloud formation and temperature that ultimately produced unrealistic opacities. While it is not clear if the clouds in their "microphysics" model using 15min time steps dried or moistened the water cycle they concluded that time steps on the order of ~1 min or less are needed to keep the polar atmosphere cloud free. How this was achieved was not explicitly stated, but is presumably related to particle size and suppression of the feedback mechanism.

Our analysis illuminates the nature of the problem as it applies to our model. During summer when the NPRC is exposed high super saturations develop in near surface air as the surface warms and sublimation rates rise. These high super saturations generate high nucleation rates that nucleate most of the available free dust if the time step is too large, such as a physics time step (16 min). Thus, the moisture available for cloud growth is spread out over a large population of IN and consequently the ice particles are small and not easily removed by gravitational sedimentation. These small particles are also bright and low, leading to a reduction in the downward solar flux without a compensating increase in the downward IR. The net effect is to cool the cap and dry out the water cycle. Use of smaller time steps for nucleation and growth (i.e., the time splitting described above) mitigates this problem, but not necessarily because it suppress the feedback mechanism described by Navarro et al. (2014). In our model, the polar atmosphere clears because of removal by sedimentation and we suspect this was the case in Navarro et al. (2014) as well. Smaller time steps nucleate fewer particles, which grow larger and fall out faster. They also allow growth to reduce super saturation and hence lower nucleation rates (Shaposhnikov et al., 2018). As shown in Figs. 2.19 and 2.20, with time splitting and 30 s time steps the lower polar atmosphere is warmer, relatively cloud free, and the atmosphere holds much more

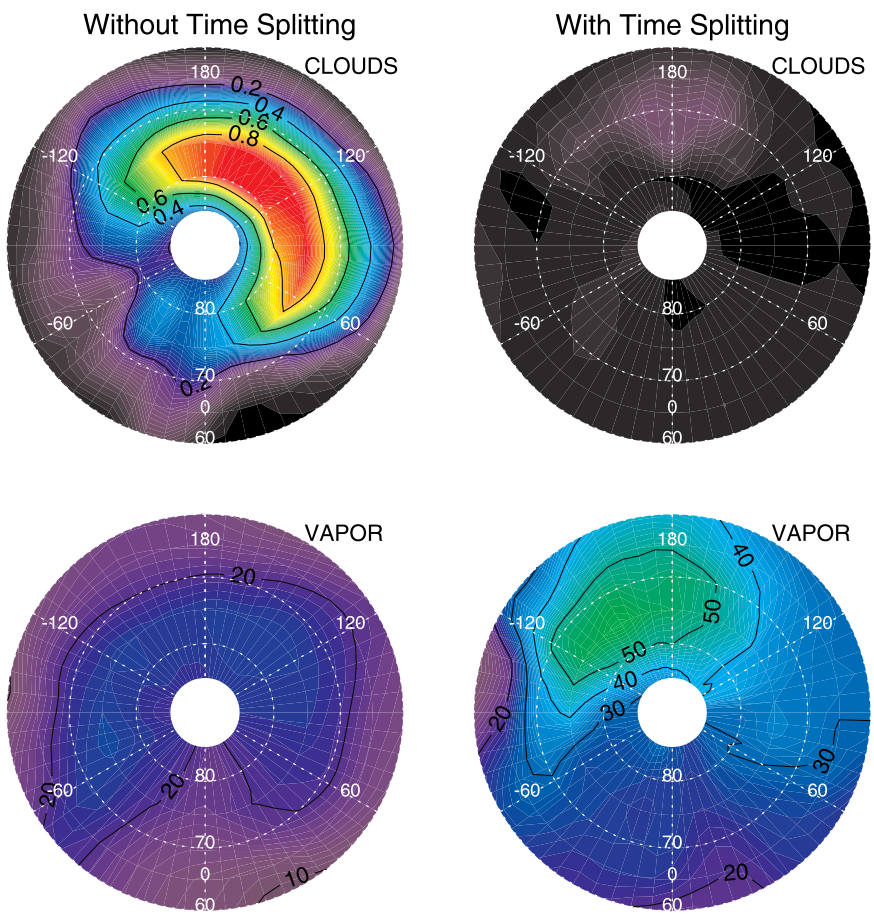

Fig. 2.19. Time average 12-μm column cloud opacity (top row) and vapor abundance (pr-μm, bottom row) fields for early northern summer. Left column is without time splitting, right column is with time splitting. In both cases the clouds are radiatively active.

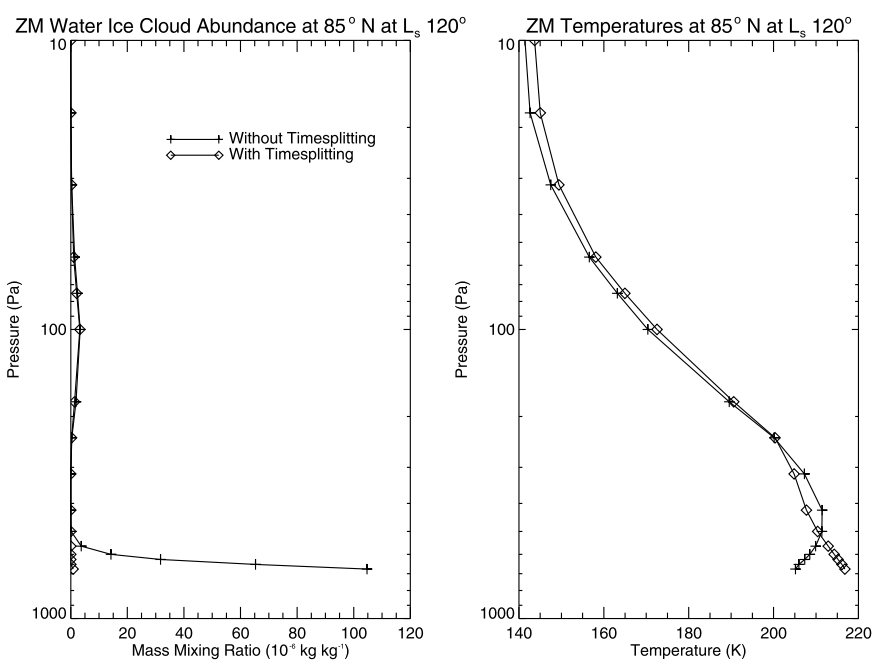

Fig. 2.20. Zonal mean cloud mixing ratio (left) and temperature (right) profiles at 85° N and L_s 120° with and without time splitting.

water; without it the lower atmosphere is too cold, too cloudy, and too dry. Thus, the reason the polar atmosphere is cloud free when using small time steps in our model is because the cloud particles that do form are removed quickly by gravitational settling.

It is worth pointing out here that the effect of polar clouds on the water cycle critically depends on the altitude they form. In our model, the clouds generally form close to the surface where they have a cooling and drying effect. However, in some of our simulations with different

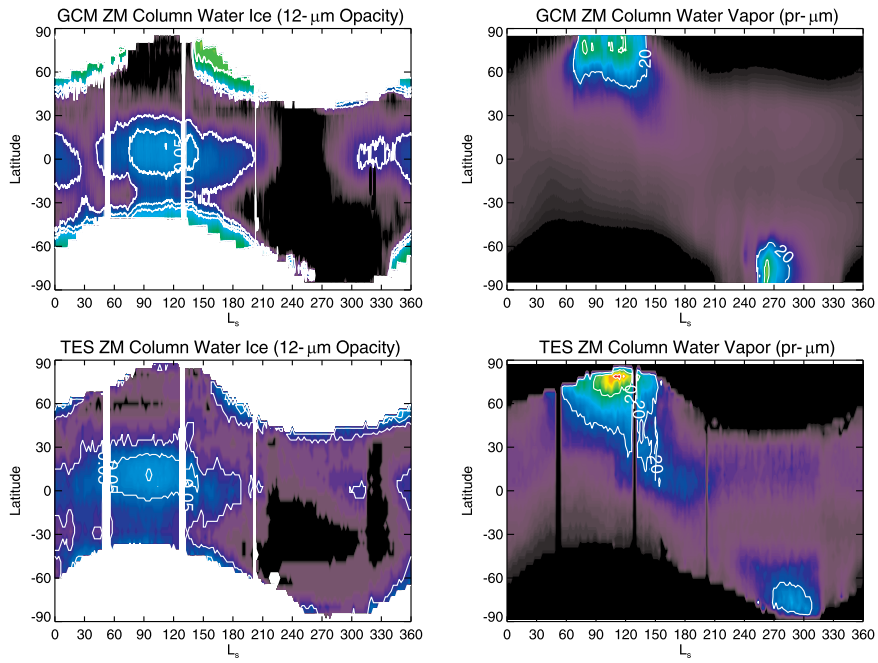

Fig. 3.1. Seasonal and latitudinal variation of zonal mean 2 PM 12-μm column cloud opacities and vapor abundances. Model results are shown in the top row, TES observations in the bottom row. White (black) regions in cloud (vapor) maps denote no retrieved data.

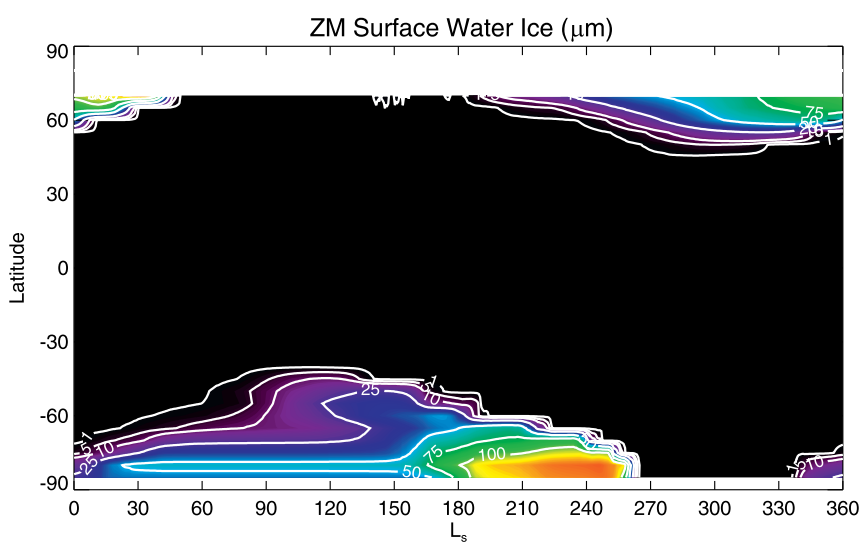

Fig. 3.2. Seasonal and latitudinal variation of the depth of zonal mean surface ice. Contours saturate above 75° N because of the presence of the NPRC (an infinite reservoir).

experimental conditions clouds can form at higher colder levels causing surface temperatures to rise. Other groups have obtained similar results (Madeleine et al., 2012; Urata and Toon, 2013). Its significance here is that it creates a positive feedback between cloud formation and surface temperatures that moistens the water cycle. Thus, summertime polar clouds can dry or moisten the water cycle depending on their altitude. While this may be an academic point for present day Mars since there are no significant summer polar clouds, either high or low, it may play an important role in past climates with different orbital conditions (e.g., Haberle et al., 2012; Madeleine et al., 2014; Kahre et al., 2018).

2.11.5. Run options

There are a variety of run options to consider when running the model. In addition to starting from a resting isothermal atmosphere (cold start) the model can also start from a previous spun up state (warm start). Various logic flags in the input file eliminate the need to recompile for specific conditions such as including the radiative effects of clouds and water vapor, the latent heat effects of water vapor phase changes, the existence of an ice albedo feedback, and whether dust in the atmosphere is specified, radiatively active, self-consistently determined, or tracks a dust map. The model also includes options for the wind stress lifting schemes used in Kahre et al. (2006) and Newman et al. (2002a, 2002b), and a dust devil lifting scheme based on Rennó et al.'s (1998) work.

3. Simulated water cycle: comparison with observations

We now compare the results of our updated model with TES, CRISM, MCS, and MARCI observations. Clouds are radiatively active, time-splitting is on, the dust fields track MY24 (see Fig. 2.11), and the vertical distribution is self-consistently determined. Water vapor radiative effects and latent heating are off as these have very little impact

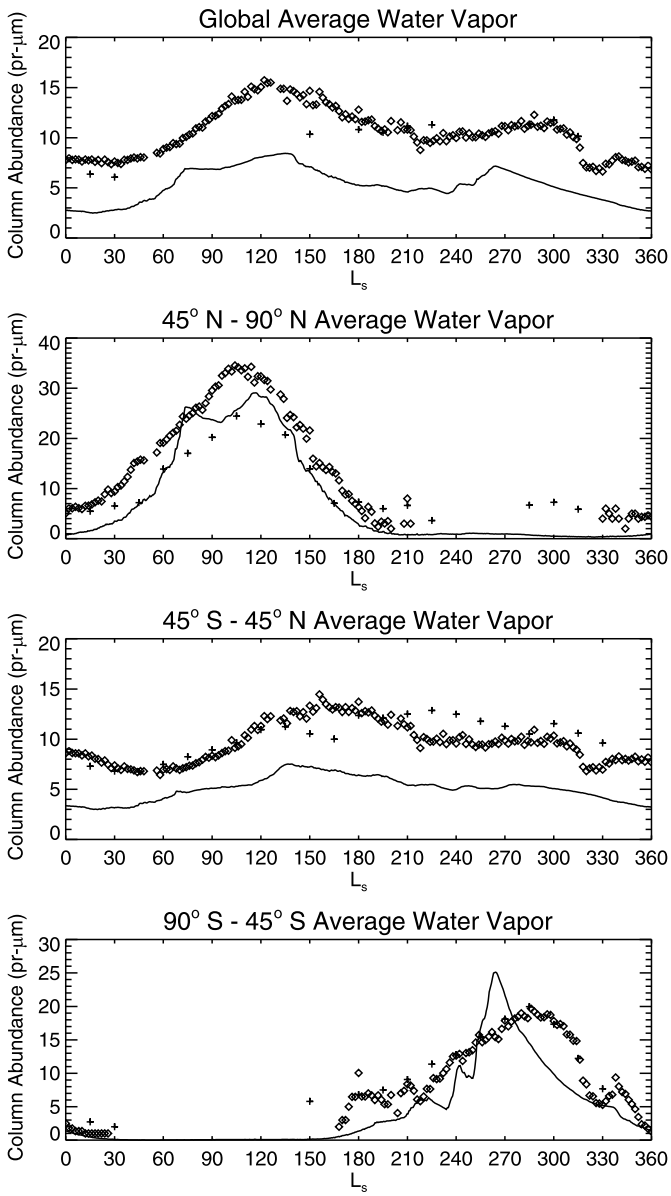

Fig. 3.3. Seasonal variation of total water vapor abundances in selected latitude bands. Open diamond symbols are TES MY26 observations; plus symbols are CRISM MY29 observations; thin solid lines are from the model. Averages are area weighted. MY26 differs from the hybrid MY24 dust forcing we use in that it had a late winter regional dust storm (see Kass et al., 2016) that coincides with the apparent dip in water abundance around L_s 320°. MY29 dust forcing was similar to MY24 in that there was no global dust storm, but there are some differences in the timing and intensity of the regional storms (see Kass et al., 2016).

on the results. We sample year 10 of a simulation warm-started from a 2-year spin up run. The water cycle seasonally repeats after ~5 Mars years and a check of an extension out to year 20 shows little change.

3.1. Moisture fields

For the moisture fields we begin by comparing the model with TES MY26 observations, which is the only complete year of TES water observations without a global dust storm. Simulated zonal mean column cloud and moisture fields and those from these TES observations are shown in Fig. 3.1. Most importantly, the north polar region in the model is cloud-free during early summer. This was a major problem with our previous simulations that is now mitigated with time splitting for nucleation and growth. Keeping the north polar region cloud free during summer while producing a decent ACB was a major goal of our modeling effort and for that we have largely succeeded.

Overall the model provides a reasonably good simulation of the latitudinal and seasonal variation of the moisture fields. When the CO_2 cap disappears and the NPRC is exposed during late spring, water sublimes into the atmosphere and column vapor abundances increase. As the season progresses much of this water is transported southward where it moistens the tropics and reaches well into the southern hemisphere. Much of this water condenses onto the south seasonal CO_2 ice cap (Fig. 3.2) where it steadily accumulates near the edge of the cap as it retreats during southern spring. This accumulation is a consequence of the cap edge "sea breeze" like circulation, which transports water ice exposed during retreat back onto the cap as it sublimates into the atmosphere. Ultimately all of this rolled up water ice is released into the atmosphere when the CO_2 cap finally disappears around L_s 270° which gives rise to the peak in column vapor abundances near the south pole at this time. This basic pattern of a peak in column vapor abundance in the north polar region during summer, followed by equatorward transport into the southern hemisphere through the fall, and a peak in south polar vapor abundance near the winter solstice defines the present water cycle and the model well captures these features.

However, the northern summer peak (~40 pr-μm) is less than observed (~60 pr-μm) while the southern peak (~40 pr-μm) is greater than observed (~30 pr-μm). It may be that the model overestimates horizontal transport between hemispheres during northern summer. Rapid extraction of water from the NPRC and cold-trapping it in the south seasonal CO_2 cap would lower peak abundances in the north and raise them in the south. Thus, the model may be too vigorous with inter-hemispheric mixing, which is on the order of weeks or less in our model. The timing of the southern hemisphere peak is also somewhat early compared to the observations and of shorter duration. The Mars-GEMS model produces similar results when compared with CRISM data (Smith et al., 2018). This may be related to a number of factors including not having an albedo dependence on non-polar surface ice, the presence of desorbing regolith, not properly simulating the retreating CO_2 ice cap, or excessive rapid mixing.

It is also clear that the model is too dry. As shown in Fig. 3.3, which also includes the CRISM data from Smith et al. (2018), global abundances in the model are almost a factor of two less than in the observations and most of the dryness is attributed to the lower latitudes between ± 45°. Poleward of 45° in each hemisphere the comparison is better. It is unclear why the northern high latitude CRISM water abundances are systematically less than TES making it difficult to assess the realism of the model results in this latitude sector. Nevertheless, the double peak in model water abundances, which we attribute to the warming effect of transient high clouds in the model, is not seen in either data set. Tropical dryness during late summer and early fall was also a concern in the Laboratoire de Météorologie Dynamique (LMD) model of Navarro et al. (2014) in spite of the fact that their global abundances were closer to observed abundances (obviously, their summertime peaks were greater than observed). Navarro et al. (2014) attribute their tropical dryness to a vigorous Hadley circulation pumped up by the radiative effects of clouds. This may play a role in our model as well and is consistent with the above suggestion that inter-hemispheric mixing is too strong. However, it cannot be the cause of global dryness. We take up the issue of model dryness later in Section 5.1.

3.2. Aphelion cloud belt

The ACB column abundances are well simulated in the model. Peak 12-μm opacities in Fig. 3.1 are about 0.15 in both model and observations. The peak in both cases is shifted off the equator at ~10°N and occurs shortly after summer solstice. As is observed there are virtually no clouds present north of 30°N in the model during this season, and the observed extension of the ACB into the southern hemisphere is

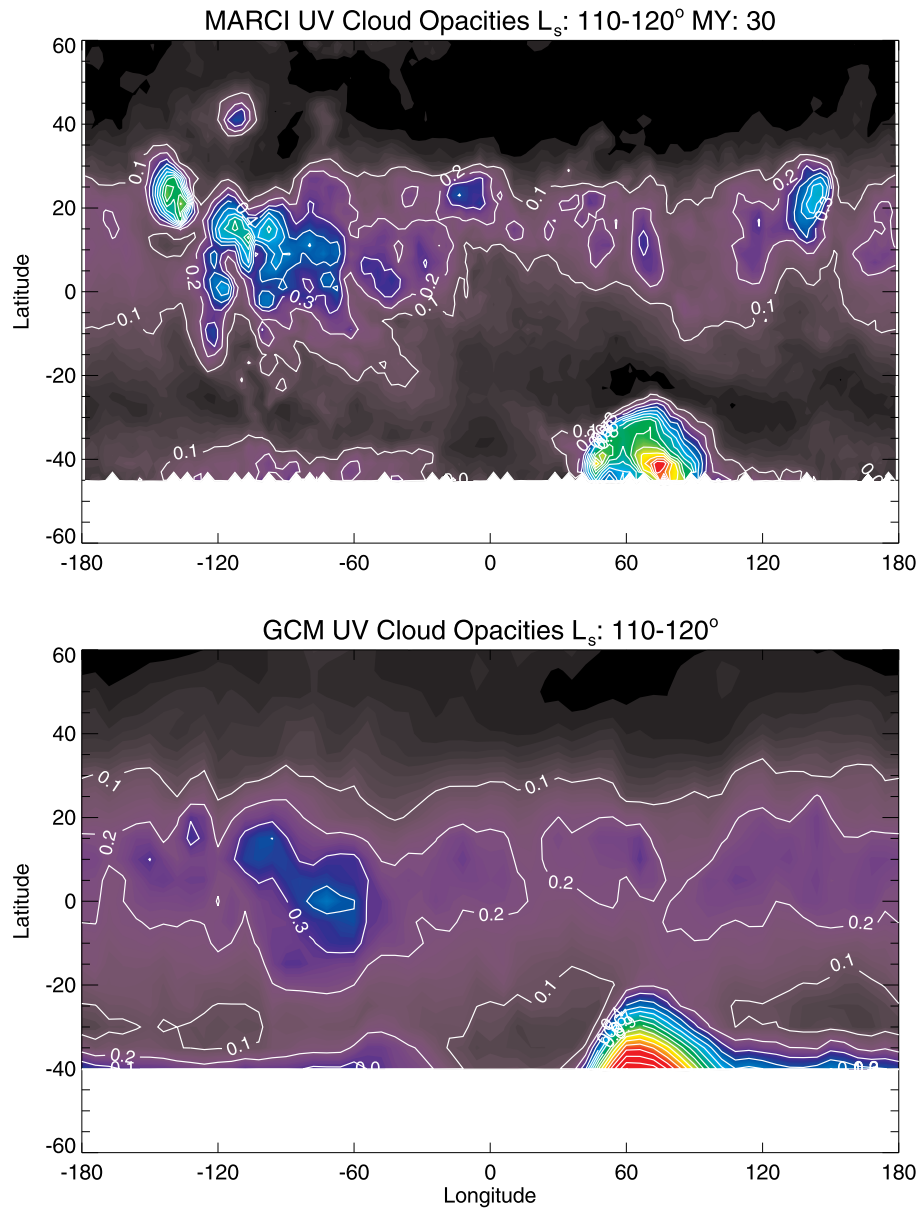

Fig. 3.4. Time average UV column cloud opacities during early northern summer from MARCI observations (top) and the model (bottom).

also well simulated. The only feature of the model ACB that is not evident in the observations is the brief springtime gap in cloudiness around L_s 30°. As we show later this gap contributes to cooler midlevel temperatures than observed.

MARCI UV observations provide a unique view of the horizontal structure of the ACB. As shown in Fig. 3.4 the model ACB is broadly similar to MARCI observations. Clouds in the model are most prevalent in the volcanic provinces of Tharsis (−60°E to −120°E) and Elysium (120°E to 180°E) as they are in the MARCI observations. However, the model clouds are too diffuse and lack the sharp definition seen in the MARCI observations. This is almost certainly a resolution issue – both horizontal and vertical. At 5° × 6° lat/lon resolution the model cannot adequately resolve the slope flows associated with the volcanoes that help produce those clouds. And our coarse vertical resolution may also be a factor. Another feature in the MARCI observations that stands out is the clouds in Hellas. These clouds are not seen by TES because the surface is too cold for reliable water ice cloud retrievals. However, the model does simulate them and we take up in detail the nature of these clouds in a separate paper (Kahre et al., 2019).

The vertical structure of the ACB at L_s 90° is compared to MCS extinction observations in Fig. 3.5. Some caution is required with these comparisons since MCS retrievals degrade as the line-of-sight opacity becomes optically thick (Kleinböhl et al., 2009). However, some comparisons are useful. In the upper part of the ACB, for example, where the MCS retrievals are robust the overall extinctions between the model and observations are similar, which is consistent with the generally good agreement with TES column abundances. However, the observed ACB is somewhat broader in latitude than in the model. And while MCS cannot see the base of the clouds because of the large line-of-sight opacities in the lower atmosphere, it does see the cloud tops, which are higher than in our simulation. This is best illustrated in the bottom panel of Fig. 3.5 where the observed cloud tops are near the 20 Pa level while modeled tops are closer to the 50 Pa level. This is an important discrepancy, which we discuss further in Section 5.2.

The simulated effective particle sizes in the ACB typically have radii in the several μm range and vary only minimally during the season. There is some indication in the observations that particle sizes may actually decrease with time as the ACB builds during spring and early summer. Fig. 3.6 shows the UV and IR column opacities at 15°N self-consistently derived from the model as a function of season along with

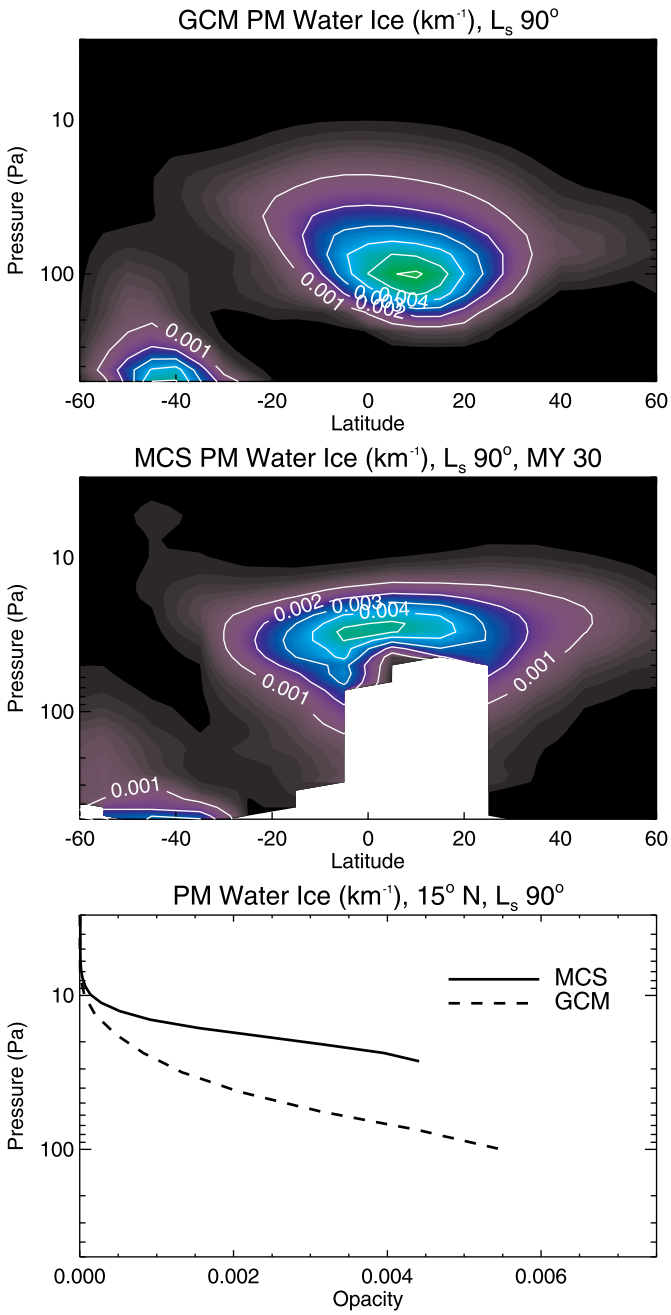

Fig. 3.5. Time and zonal average water ice extinction during early northern summer from the model (top) and MCS data (middle). White region in MCS plot denotes no retrieved data. Bottom plot shows profiles at 15°N from MCS (solid line) and the model (dashed line).

those derived for the same latitude from MARCI UV extinction measurements and MGS TES IR absorption observations. For the season of interest, L_s 30–120°, the model simulates well the time variation of observed UV opacities but is systematically too low in the IR. More importantly, the ratio of UV extinction to IR absorption in the model generally has the opposite trend as in the observations. The model ratio decreases somewhat during this season while it increases rather sharply in the observations. The most logical explanation for this trend in the observations is a decreasing effective particle size, whereas in the model they are not changing significantly or increasing slightly. A decrease in particle size is counter-intuitive and we have not yet found a good explanation for this behavior. An obvious possibility, adding dust to the atmosphere to nucleate more particles, does not change the

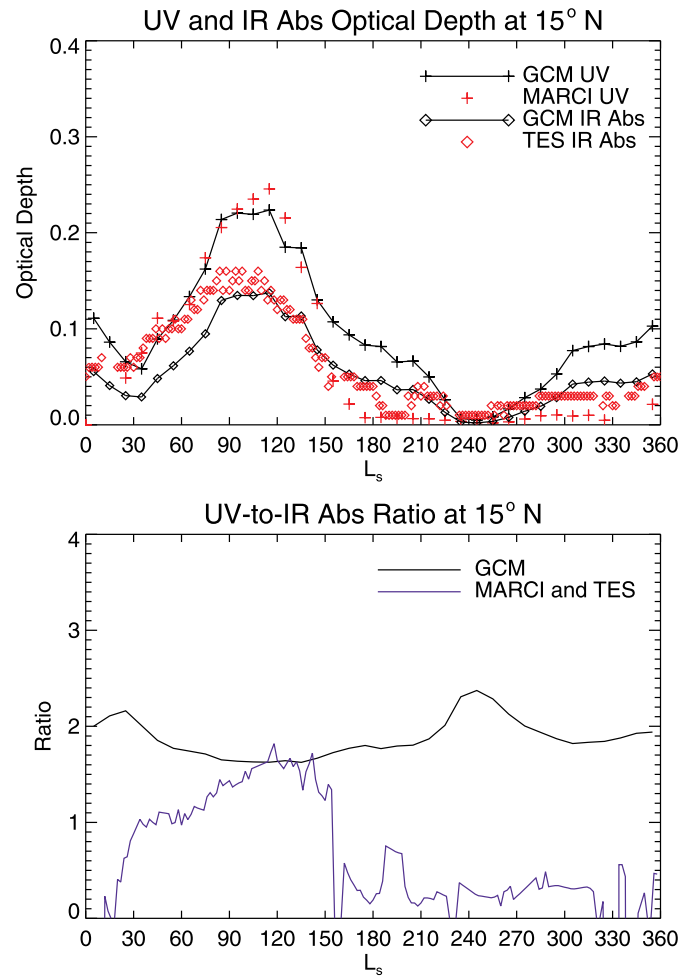

Fig. 3.6. Top: Seasonal variation of the UV and IR absorption optical depth at 15°N. Solid lines are from the model; red symbols are from the observations. Bottom: Same, but for the ratio of UV to IR absorption opacity from the model (black line) and observations (blue line). (For interpretation of the references to color in this figure legend, the reader is referred to the web version of this article.)

model results (Klassen et al., 2017) and is in any case opposite the overall downward trend in atmospheric dust loading observed at this season (see Fig. 2.11). More work is needed to better understand this puzzling behavior.

3.3. Polar hoods

The realism of the simulated polar hoods shown in Fig. 3.1 is difficult to fully assess because of the difficulty with observing over a cold surface. However, it does appear that in both hemispheres the polar hoods form too early and are thicker than observed by TES. This could indicate a potential role for an adsorbing regolith, which would store some of the water locked up in the polar hoods. The polar hoods in the model also have an annular structure in that their maximum thickness during winter solstice is found near the cap edge (see Fig. 4.1 below) with relatively cloud free regions at very high latitudes near the pole. While TES nadir observations cannot see into the deep polar interior because of retrieval limitations, MCS limb observations do show clouds in the polar interior during winter in both hemispheres. According to Benson et al. (2010, 2011) they extend all the way to the pole throughout winter in the northern hemisphere but only during late winter and early spring in the southern hemisphere. How much they extend toward the surface, however, is difficult to determine from MCS

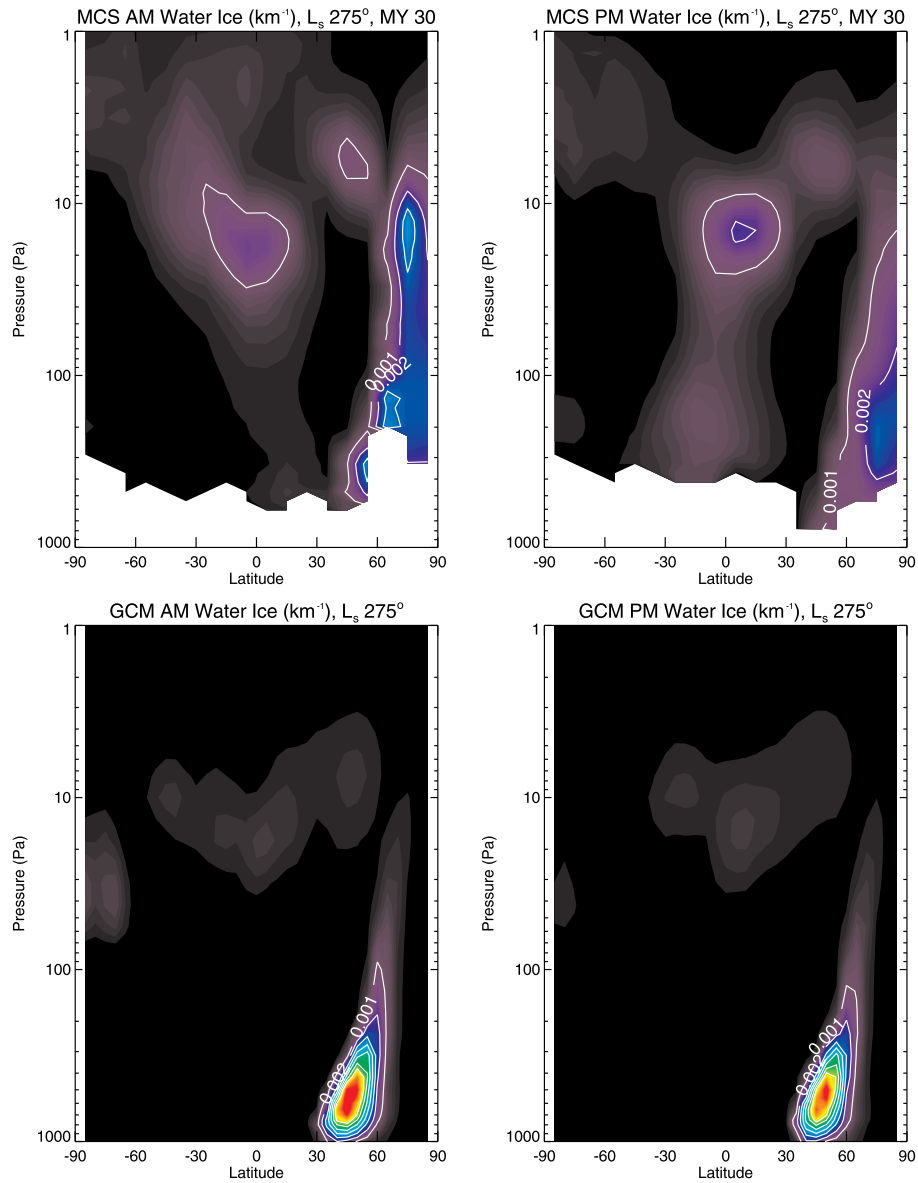

Fig. 3.7. Time and zonal average AM (left column) and PM (right column) water ice extinction as a function of latitude and pressure at L_s 275°. Top row is from MCS observations; bottom row is from the model. White regions in MCS plots denote no retrieved data.

data because of viewing limitations at low altitudes.

The annular nature of the north polar hood is a feature of our model and can be seen in other models as well (Richardson and Wilson, 2002; Navarro et al., 2014 and Pottier et al., 2017). In these models, maximum cloud abundances occur near the edge of the seasonal polar cap with less cloudy regions at higher and lower latitudes. We further illustrate this for our model in Fig. 3.7 where we plot extinction instead of mixing ratio to more directly compare with MCS. Cloud extinction is significant in MCS observations poleward of 75–80°N and at altitudes above the 300–400 Pa level. While there is a poleward tilt with altitude in the model, as is somewhat suggestive in the data, the model clouds are not as opaque nor as high as seen by MCS, and there is virtually no extinction in the model at 85°N at any altitude contrary to the observations. The model also does not produce the high-altitude tropical clouds seen by MCS. While the extinctions we compute are based on model derived particle sizes and extinction coefficients, which can be different from those assumed for the MCS retrievals, we do not believe this is the source of the discrepancy. Use of MCS conversion factors to compute extinction from our cloud mass mixing ratio fields still shows the model to be significantly deficient in high altitude tropical and polar clouds. Thus, we believe the model is not simulating an important observation that has implications for the transport and deposition of water into the polar region. We discuss this further in Section 5.3.

4. Radiative effects of clouds

4.1. Water cycle

We assess the radiative effects of clouds by comparing in Fig. 4.1 our standard run where clouds are radiatively active with an identical run but where the clouds are radiatively passive. As can be seen the overall cloud and moisture fields are very similar for the two cases. Thus, in our model the effectiveness of time-splitting in reducing cloudiness over the polar cap is the same for both passive and active cases. The active case is somewhat wetter and cloudier than the passive case, but the patterns and seasonal variations are quite similar. The slightly wetter nature of the active simulation is due to a longer sublimation season and not to any significant difference in NPRC surface temperatures. In the model there are no clouds over the NPRC during summer for either simulation, hence they have very little effect on the surface heat budget leading to

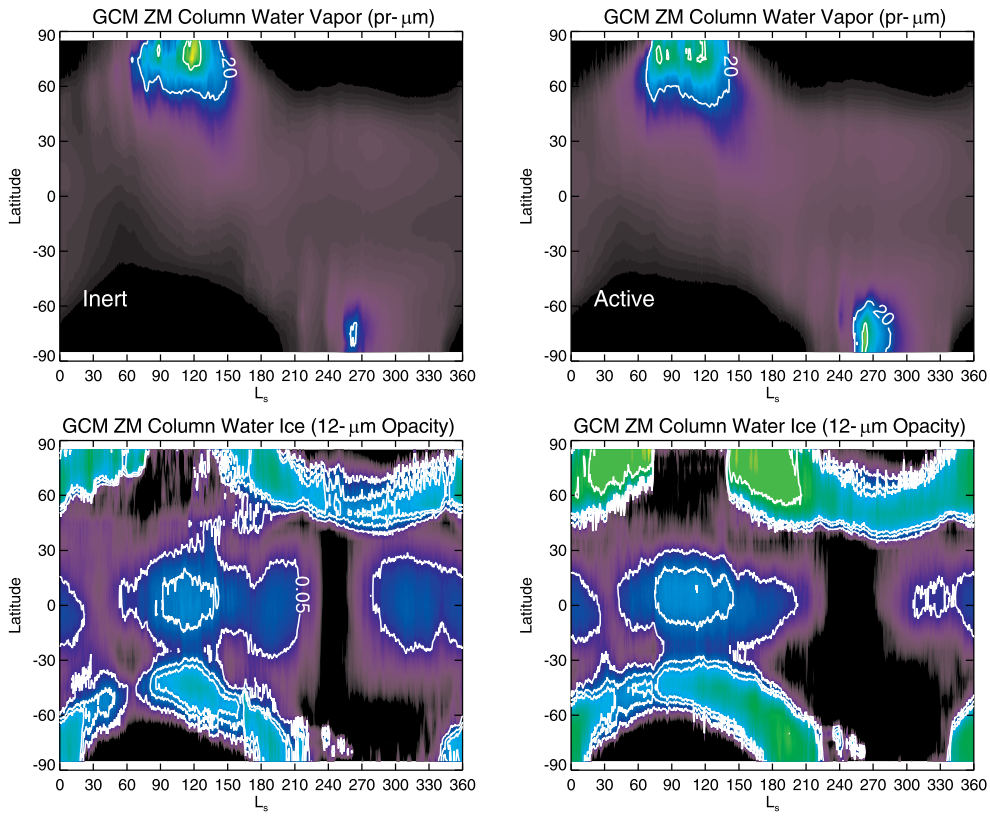

Fig. 4.1. Seasonal variation of the zonal mean column water vapor (top row) and 12-μm cloud opacity (bottom row). Left column is for passive clouds; right column is for radiatively active clouds.

similar surface temperatures and sublimation rates.

Instead, as can be seen from the appearance and disappearance of north polar clouds in Fig. 4.1, CO_2 frost on the surface disappears earlier and forms later when the clouds are active. The earlier peak in column vapor seen in Fig. 4.1 is consistent with this interpretation. The radiative effect of clouds, when they are present, thickens the polar hoods, reduces CO_2 condensation during winter and hence, hastens sublimation during spring. The hoods thicken because they more efficiently cool to space by emission when radiatively active. But the downward component of emission warms the surface even though they are low and optically thick. This is because when they do form, which is late in the season, the sun is already very low on the horizon so that the small increase in reflected loss of solar radiation at the surface is not sufficient to compensate for the increase in downward IR. The sharp rise in surface temperatures just before L_s 150° (shown below in Figs. 5.1 and 5.2) is indeed coincident with the appearance of clouds at those latitudes. Thus, it is the radiative effect of the clouds on the CO_2 cycle that moistens the water cycle and not higher surface temperatures. The NPRC is exposed earlier and covered later which lengthens the sublimation season and boosts the total input of moisture to the atmosphere, though not by a large amount.

The relative similarity between the passive and active cases differs from what Navarro et al. (2014) found with the LMD model. In their model passive clouds led to a drier water cycle by about a factor of two. They cite the radiative effects of clouds on surface temperatures before L_s 90° and enhanced sublimation fluxes due to stronger winds associated with stronger baroclinic eddies as the main reason for a wetter water cycle with active clouds. Neither plays as prominent a role in our simulations because of the near complete absence of clouds in both cases.

Another point worth explaining is why the peak column vapor abundances over the NPRC are so similar in the passive and active cases, yet the peaks in the southern hemisphere are significantly different. The similarity in the northern peaks implies that the equatorward transport out of the NPRC region is similar for the two cases and the transport diagnostics shown in Fig. 4.2 confirm this. This makes sense, of course, since in both cases these regions are relatively cloud free. Thus, there is little change to local circulation patterns. However, the water exported from the polar region is carried into the southern hemisphere by circulation systems that are significantly altered by the radiative effect of clouds. Yet even so, the change in the transport of total water (vapor + cloud) across the equator is small. Thus, the total water pumped into the southern hemisphere is nearly the same in both cases. The cause of the greater southern hemisphere peak in the active case is therefore not enhanced cross equatorial transport that finds its way into the south seasonal cap, but instead an increase in the fraction of water transported across the equator that is deposited onto the cap.

In our model it is the stationary eddies that are mainly responsible for the southward transport of total water into the south polar cap at this season (see Fig. 4.2) and these are stronger with radiatively active clouds. Steele et al. (2014) also found a prominent role for stationary eddies in the southward transport of water at this season. These eddies supply the moisture (mostly as vapor) needed to form the polar hood clouds at mid southern latitudes. When clouds are radiatively active the moisture supply is increased helping thicken the polar hoods. There may even be a modest feedback in that active clouds enhance cooling which strengthens the stationary eddies which supply more moisture which thickens the clouds and further enhances the cooling. Sedimentation from the polar hoods onto the seasonal cap, along with direct vapor deposition, provides the source of water that ultimately is released to the atmosphere when the cap retreats. Both these deposition mechanisms are enhanced when clouds are radiatively active. See Kahre et al. (2018) for a more detailed discussion of the southward transport of water at this season.

Another interesting aspect of our model is that while the total water transport by all components of the circulation is southward at this

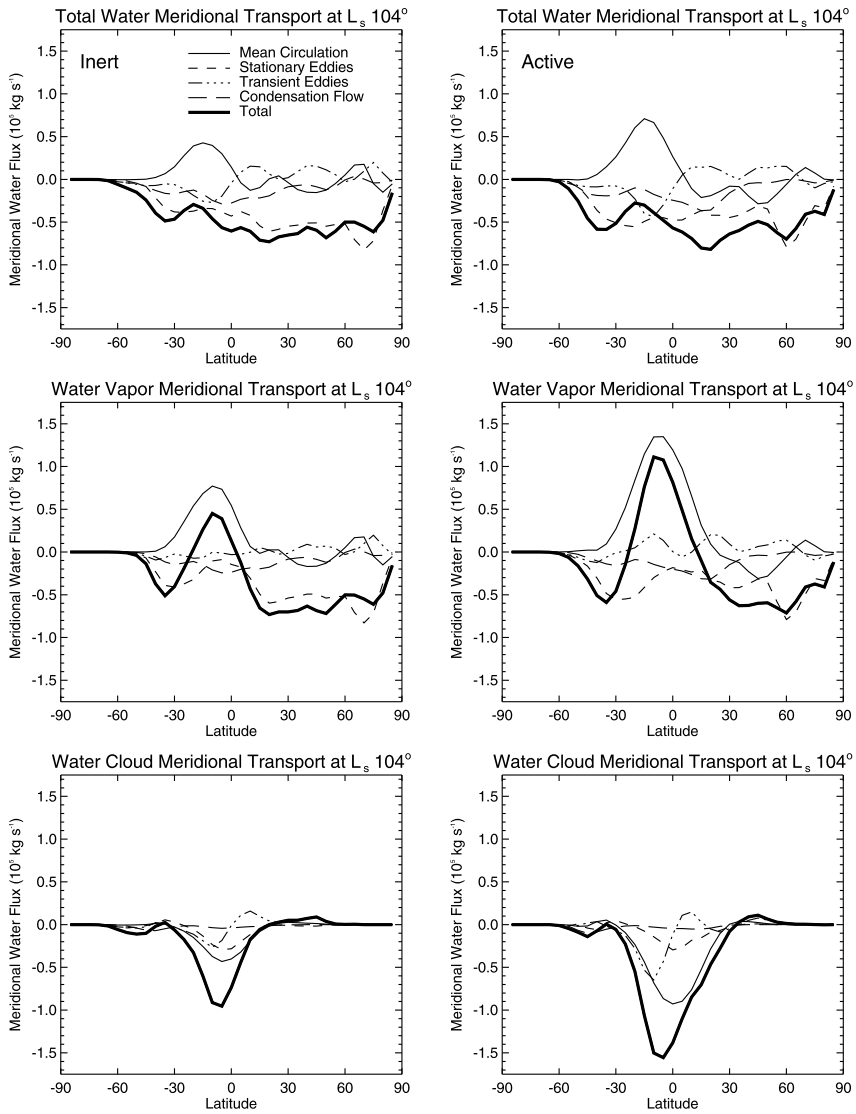

Fig. 4.2. Transport diagnostics for the inert (left column) and active (right column) cases. Top row is total water transport, middle row is vapor only, and bottom row is cloud only.

season (see thick black line in top row of Fig. 4.2), near the equator the zonal mean (Hadley) circulation transports total water northward at this season. The traditional view is that the zonal mean circulation transports total water into the southern hemisphere at this season (e.g., Haberle and Jakosky, 1990; Montmessin et al., 2017) and that this should be enhanced when the clouds are radiatively active (e.g., Wilson et al., 2008; Madeleine et al., 2012; Kahre et al., 2015). Indeed, the mean meridional circulation does strengthen in the model when the clouds are radiatively active (Fig. 4.3). However, it transports total water northward not southward. As can be seen in Fig. 4.3, water vapor is confined to the lower levels below the ACB where the return branch is moving northward. The vertically integrated net transport of vapor is therefore toward the north as indicated in Fig. 4.2. Steele et al. (2014) obtain a similar result. Clouds, on the other hand, form in the ascending branch near the top of the cell such that their net transport is toward the south. For total water, the southward transport of cloud in the upper branch is not sufficient to reverse the northward transport of vapor in the lower branch and consequently the transport of total water by the Hadley circulation is toward the north.

This is, of course, a model dependent result. It depends critically upon where the clouds form with respect to the Hadley cell, how thick they get, and how fast they settle out. Different assumptions about cloud microphysics, radiative forcing, vertical mixing, etc., will produce different results. Montmessin et al. (2017), for example, find a more prominent role for the mean meridional circulation in the southward transport of total water at this season, which may be due to these different assumptions. Higher thicker clouds would favor southward transport. In our model, as discussed in Section 3, the ACB is lower than observed so the reality of our transport diagnosis is uncertain.

The radiative effect of the ACB on midlevel temperatures is shown in Fig. 4.4. During northern spring and summer, model temperatures are too cold compared to TES when clouds are passive but agree well with the observations for this period when clouds are active. The increase in temperatures is due to the absorption of upwelling infrared radiation by high relatively cold clouds overlying a warm surface (Wilson et al., 2008). During northern fall and winter when clouds are absent both cases agree well with observations suggesting that the self-consistently determined vertical distribution of dust is well simulated by the model at this time. The cooler model temperatures between L_s 30–90° in the active simulation are due to the absence of clouds. Clouds in the model dissipate during this interval whereas in the observations their opacities steadily increase (see Fig. 3.1). Since there is no indication in Fig. 2.11 for any significant change in the dust loading at this time this does not appear to be a factor. The disappearance may

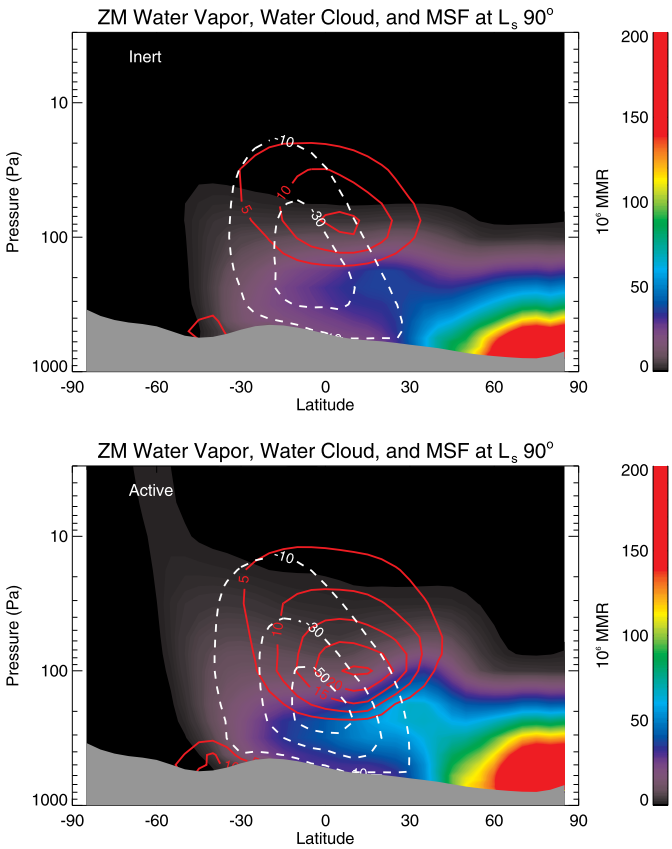

Fig. 4.3. Time and zonal mean mass stream function (dashed white lines, $10^8\,\mathrm{kg\,s^{-1}}$), cloud ice mass mixing ratio (solid red lines, $10^{-6}\,\mathrm{kg\,kg^{-1}}$), and water vapor mass mixing ratio (color shading) for the passive (left) and active (right) cases at L_s 90°. (For interpretation of the references to color in this figure legend, the reader is referred to the web version of this article.)

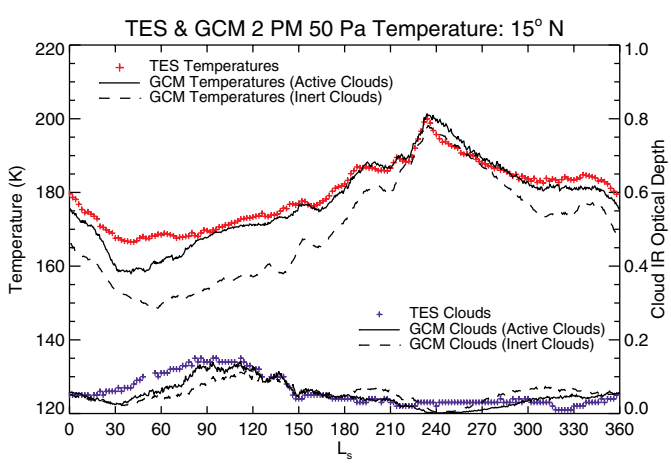

Fig. 4.4. Seasonal variation of zonal mean 2 PM 50 Pa temperatures from TES (red plus symbols) and from the model inert cloud (dashed line) and active cloud (solid line) cases. Bottom three curves refer to the right y-axis and represent zonal mean 12-μm cloud opacity from TES (blue plus symbols) and the model (solid and dashed lines). (For interpretation of the references to color in this figure legend, the reader is referred to the web version of this article.)

instead be due to a reduction in the supply of moisture. At this season the only moisture source in the model is seasonal ice incorporated into the north polar CO_2 cap that sublimes into the atmosphere as the cap retreats. Perhaps too much of this subliming water is trapped in the polar hoods, which are too thick in our model, thereby preventing it

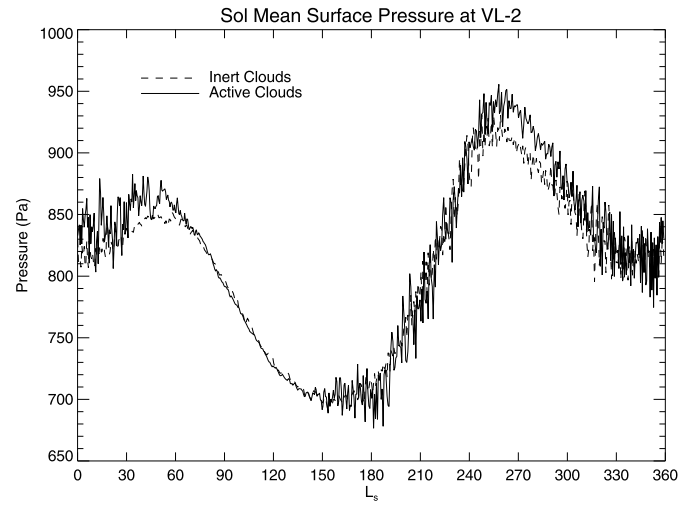

Fig. 4.5. Seasonal variation of model daily average surface pressures at the Viking Lander 2 site for the inert (dashed line) and active (solid line) cases.

from reaching the ACB. As this is the coldest time of year, small changes in the moisture supply can have significant effects on cloud formation.

4.2. Planetary eddies

We have already mentioned the radiative effects of clouds on the mean meridional circulation (see above) and others have discussed this in greater detail (Wilson et al., 2008; Madeleine et al., 2012; Navarro et al., 2014; Steele et al., 2014; Kahre et al., 2015). Thus, we focus here briefly on the transient eddies, stationary waves, and thermal tides. These are the planetary scale eddy components of the global circulation whose characteristics are also sensitive to cloud forcing, and at least for stationary waves this has been less explored in the literature.

4.2.1. Transient eddies

As found by Wilson (2011), Mulholland et al. (2016), and Pottier et al. (2017) the transient eddies are much more vigorous when clouds are radiatively active. As shown in Fig. 4.5 the day-to-day fluctuations in daily averaged surface pressures increase with radiatively active clouds. The increase can be as much as a factor of two at some seasons. These fluctuations are mainly due to baroclinic eddies having periods of 2–8 sols and zonal wavenumbers 1–5 (see Barnes et al., 2017 for a review). Radiatively active clouds can change the thermal structure and associated zonal wind fields in a way that favors baroclinic instability. An example is shown in Fig. 4.6 for the late northern winter season when the eddies are particularly strong. In this case, cooling by the polar hood clouds at northern midlatitudes increases the low-level midlatitude temperature gradients and corresponding zonal wind shear, conditions that favor increased growth rates for baroclinically unstable waves (e.g., Barnes, 1984). Thus, the polar hood clouds play an important role in the general forcing of wintertime midlatitude transient eddies.

We compare simulated transient eddy activity for the passive and active cases with that from Viking Lander 2 data in Fig. 4.7. The curves represent 10 Sol running means of the root mean square variance of deviations of daily average pressure from a seasonal harmonic fit. For most of the fall season the passive eddies are too weak compared to observations while the active eddies are too strong. We believe this is due to a polar hood that is too thick and therefore cools too much. As Fig. 3.1 shows the simulated north polar hood is thicker than observed for the period between L_s ~150–210° when the active eddies are too strong. A similar story holds for late northern winter and early spring between L_s ~350–50°. For both these seasons thinner polar hoods would appear to provide a better match.

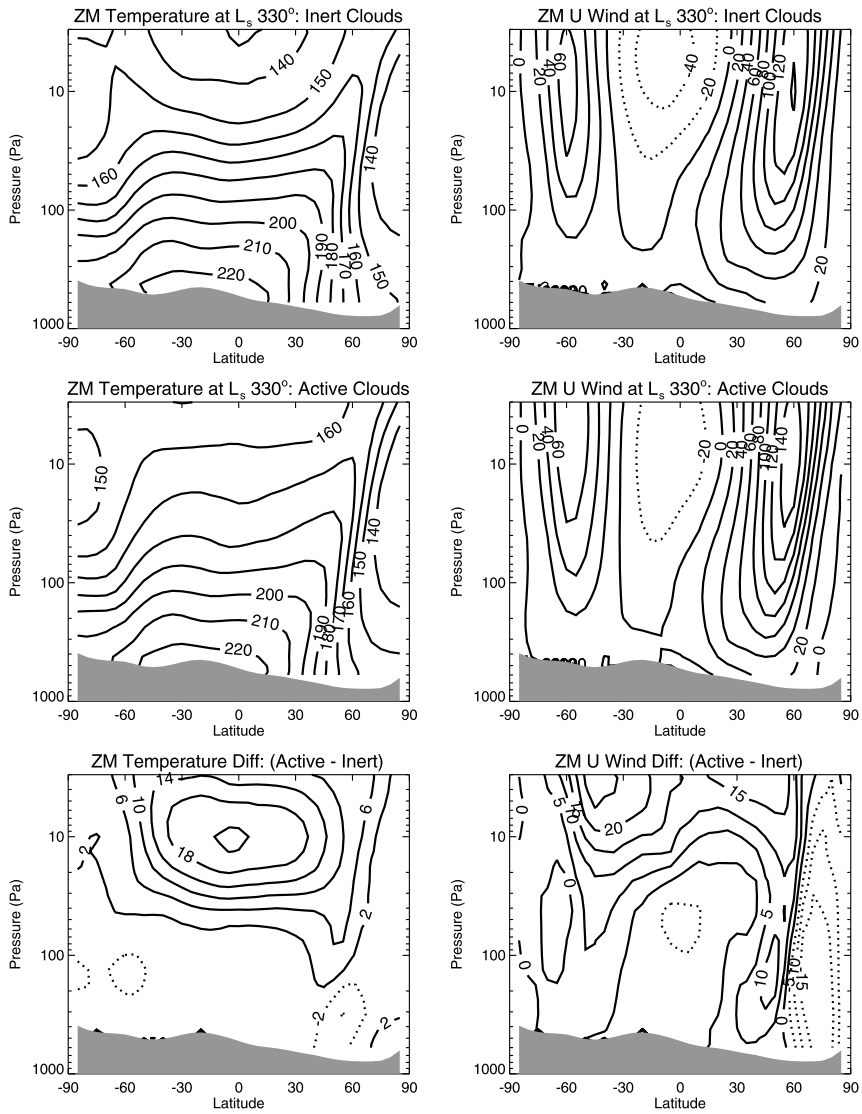

Fig. 4.6. Left column: time and zonal average temperatures at L_s 330° for the inert simulation (top), active simulation (middle), and temperature difference (bottom). Right column: same but for the zonal wind.

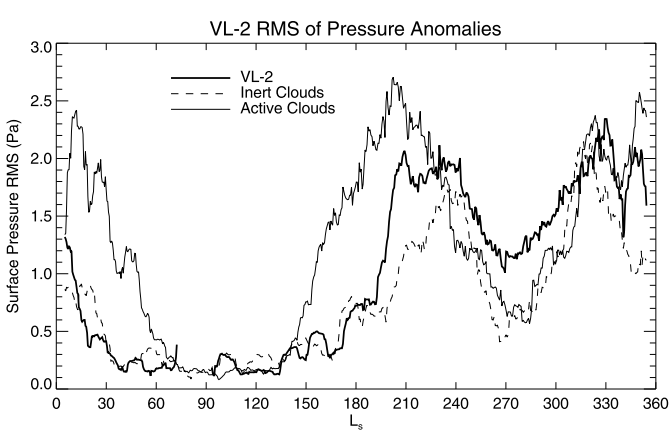

Fig. 4.7. Root mean square surface pressure variance at the Viking Lander 2 site. Model results are the grey lines: solid for the active case and dashed for the inert case. Dark solid line is the observations. For each case, we fit a curve to the annual cycle of daily means and compute a 10-sol running mean variance from it.

For late northern fall and early winter, however, both cases show less activity than the observations suggesting a more complicated story. The late northern fall/early winter period is the so-called solsticial pause season that is characterized by a significant decrease in near-surface eddy activity. Free running GCMs, like ours, have simulated this phenomena as early as the 1990s (Hourdin et al., 1995) and more recently it appears in the reanalysis of TES data by Lewis et al. (2016) suggesting that it is a real feature of the Martian global circulation. Mulholland et al. (2016) and Lee et al. (2018) discuss the cause of the pause and place a major role on the radiative effects of clouds. Evidence for the existence of a pause in our model can be seen in Figs. 4.5 and 4.7. It is also readily apparent in the near-surface zonal mean eddy temperature variance shown in Fig. 4.8. For both cases, eddy temperature fluctuations are large during fall and late winter/spring in both hemispheres, but comparatively small around the winter solstice. With active clouds, however, eddy temperature amplitudes nearly double and are in much better agreement with those from the Lewis et al. (2016) reanalysis than those from the passive simulation.

In the active case, the increase in the temperature variance at northern midlatitudes during fall is particularly interesting since it is also accompanied by an equatorward shift in the maximum and an overall broadening of the meridional scale of the eddies. At L_s 210°, for

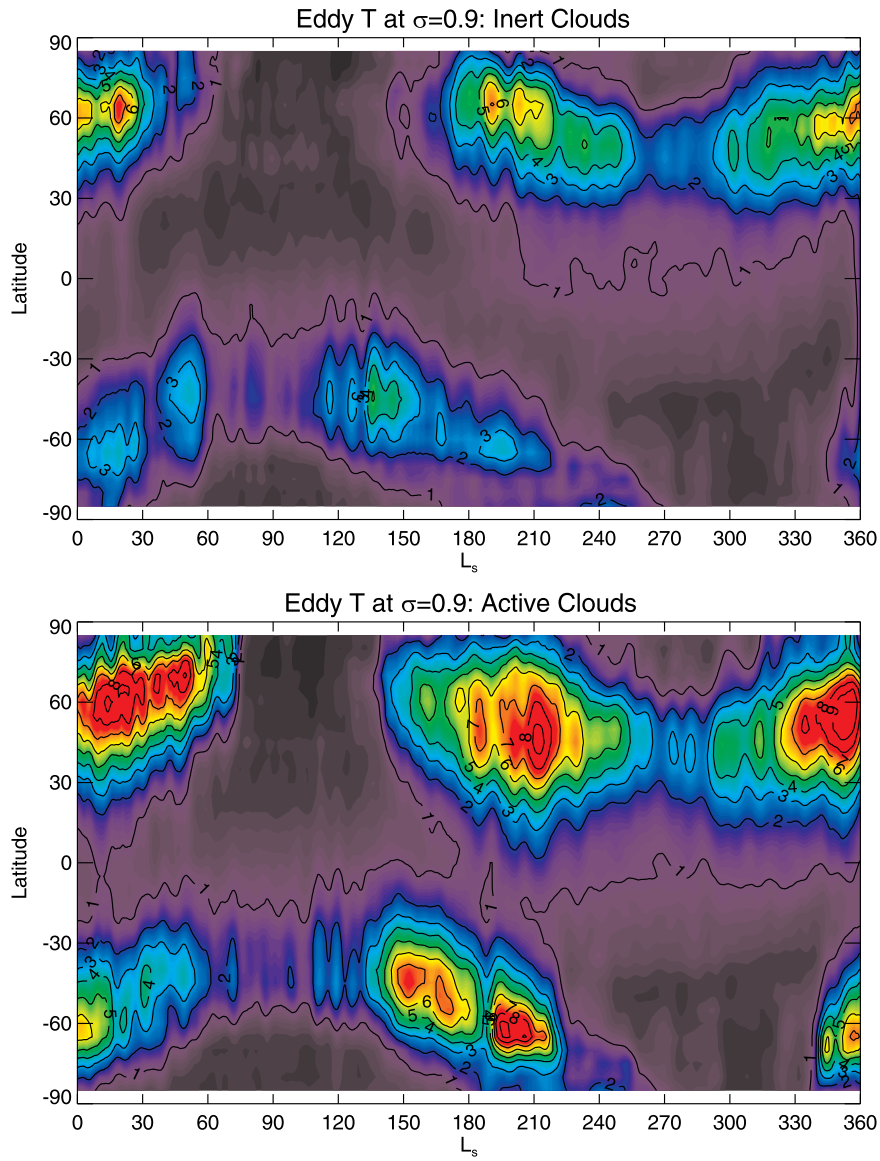

Fig. 4.8. Root mean-square eddy temperature variance near the surface (~1 km) for the inert (top) and active (bottom) cases.

example, the 2 °K contour in the northern hemisphere extends from the pole and nearly reaches the equator. Much of the boost in eddy activity in our model comes from the enhancement in wavenumber 3 disturbances (not shown). Wavenumber 3 is the predominant wavelength of the equator-crossing "flushing" dust storms discussed by Wang et al. (2003), Wang and Fisher (2009), Hinson and Wang (2010), and more recently in Wang (2018). These storms have been linked to the triggering of regional scale storms in the southern hemisphere. Equator crossing northern hemisphere eddies have been detected in surface pressure data from the Curiosity Rover (Haberle et al., 2019a) giving further credence to the ideas proposed by these authors. Thus, the radiative effects of clouds, and the polar hoods in particular, may also play a significant role in the global dust cycle.

Finally, we briefly look how clouds alter the eddy heat and momentum fluxes. For some seasons, such as L_s 320°, there are only minor differences which is consistent with the small change in pressure variations at this season as shown in Fig. 4.5. For other seasons, such as L_s 30°, the differences are quite significant, though again this may be the result of overly thick polar hoods. As shown in Fig. 4.9 synoptic period variability is significantly enhanced in the active cloud case. Transient-eddy poleward heat fluxes $\overline{[v'T']}$ are enhanced in both hemispheres and are more vertically extensive in the active case compared to the passive case. Their magnitudes increase by a factor of four at mid northern latitudes. The poleward momentum fluxes $\overline{[v'u']}$ are also significantly strengthened. As such, the baroclinic/barotropic eastward traveling waves are much more vigorous and efficient in transporting heat, momentum and other scalar quantities (e.g., atmospheric tracers) within middle latitudes. More detailed studies of their wave structures are needed to better understand how these changes occur, but it is clear that the radiative effect of clouds can have a major impact on transient eddies and their role in the heat, momentum, and tracer budgets.

4.2.2. *Stationary waves*

In a separate paper we attribute a wave 2 feature in the north polar hood during late winter to a forced stationary wave and assess how the wind and moisture fields interact to produce it (Haberle et al., 2019b). Here we focus on the effect of cloud forcing on the stationary eddies, which is more complicated to unravel. We mentioned in Section 4.1 that radiatively active clouds increase the stationary eddy moisture fluxes into the southern hemisphere during the wet season (see Fig. 4.2). This transport occurs mainly near the surface where the eddies are more tightly coupled to topography and changes to the wind

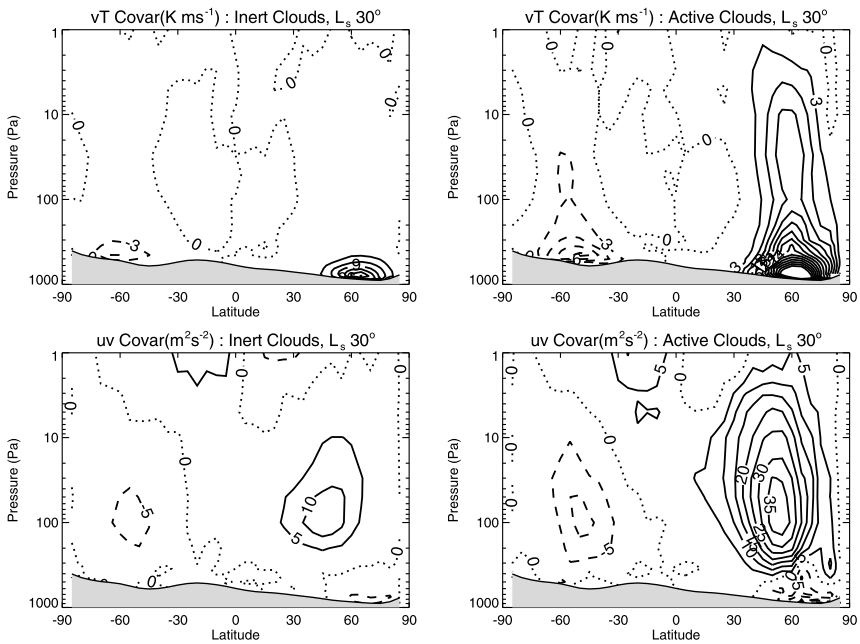

Fig. 4.9. Transient eddy poleward heat flux (top row) and momentum flux (bottom row) for the inert case (left column) and active case (right column) during early northern spring (L_s 30°). The contour intervals in top and bottom panels are $3\,\mathrm{K\,m\,s^{-1}}$ and $5\,\mathrm{m^{-2}\,s^{-2}}$, respectively. Positive values are solid, negative values are dashed.

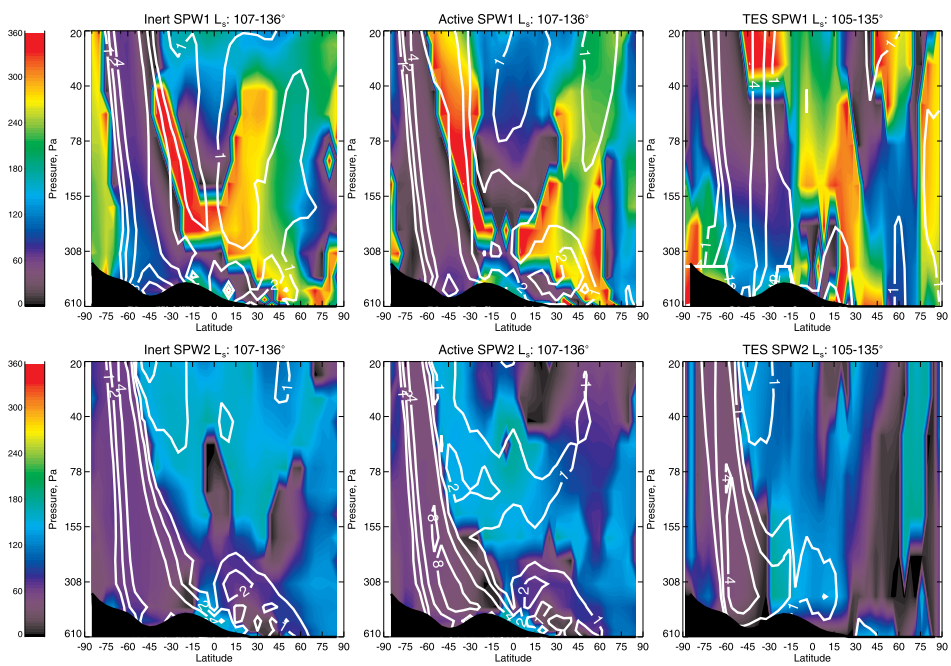

Fig. 4.10. Amplitudes and phases of stationary planetary wave 1 (SPW1, top row) and wave 2 (SPW2, bottom row) for early northern summer (L_s 105–135°). Columns denote inert (left), active (middle), and observed (right) results. Amplitudes are contoured at 1,2,4 and 8 K intervals. Phases are color shaded from blue (0° phase) to red (360° phase). Phases are in East Longitude. (For interpretation of the references to color in this figure legend, the reader is referred to the web version of this article.)

and moisture fields are subtle enough to modestly increase their correlation. Regarding their deeper structures, however, the radiative effects of the clouds are also modest as both the passive and active cases shown in Fig. 4.10 for early northern summer compare reasonably well with Banfield et al.'s (2003) analysis of TES data. The latitudinal and vertical structure of the model wave 1 and 2 amplitudes and phases, as well as their magnitudes, are not strongly affected by cloud radiative forcing and are similar to those in Banfield et al.'s analysis.

This is not the case for other seasons, however. During northern fall equinox, for example, a period when we know the model polar hoods are too thick in each hemisphere, radiatively active clouds can improve model agreement with observations in some cases, and degrade it in others. We illustrate this in Fig. 4.11. In both hemispheres the wave 1 response at upper levels improves with cloud forcing, though it is too strong near the surface in the southern hemisphere. For wave 2 the southern hemisphere response is clearly too strong and not deep enough in the northern hemisphere. Thus, wave response does not appear to be proportional to cloud thickness (which is about the same in each hemisphere, see Fig. 3.1). Instead, the wave response is too strong in the south and too weak in the north. There are other things to consider, of course, such as wave guides and possible resonance (e.g., Hollingsworth and Barnes, 1996) which go well beyond the scope of this paper. Suffice it to say that the stationary wave response to cloud forcing is less obvious than that for the transient eddies and would benefit from more detailed follow-on studies.

4.2.3. *Thermal tides*

The thermal tides are a response to diurnally varying forcing and are therefore sensitive to aerosol heating and cooling within the atmosphere (see Barnes et al., 2017 for a review). The semi-diurnal tide is

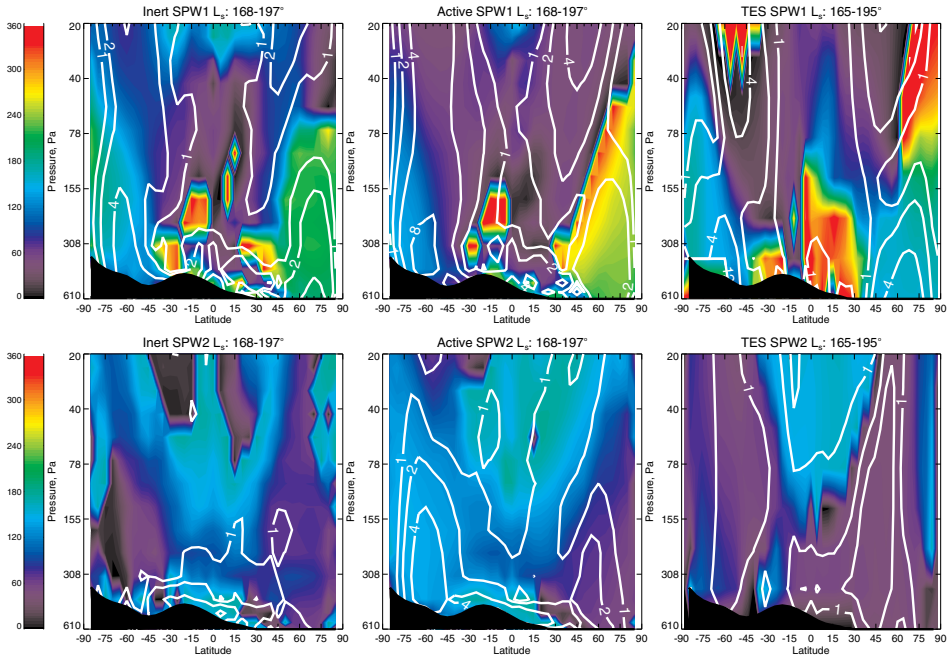

Fig. 4.11. Same as Fig. 4.10, but for late northern summer/early northern fall (L_s 168–197°).

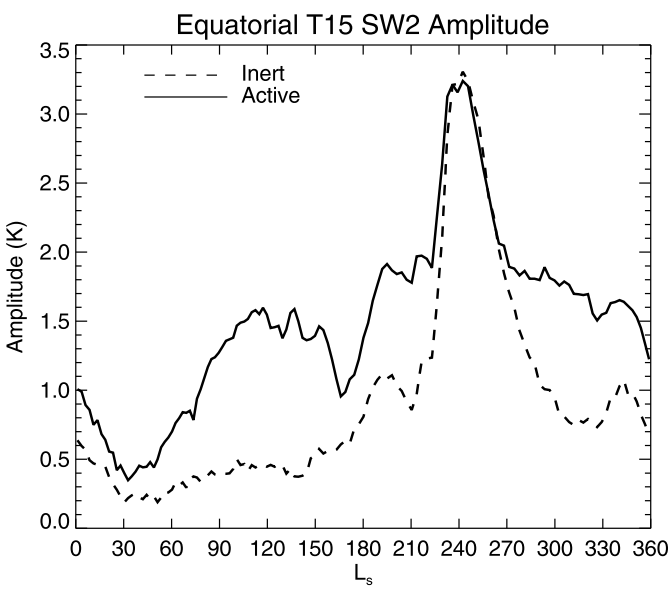

Fig. 4.12. Seasonal variation of the equatorial 15-μm band weighted temperature amplitude of the migrating semi-diurnal tide at ~50 Pa for the inert and active cases.

dominated by the sun-synchronous (migrating) mode, which has long vertical wavelengths and broad meridional scales such that it responds efficiently to global forcing. Fig. 4.12 shows the seasonal variation of the temperature amplitude of the westward migrating semi-diurnal tide (SW2) at ~25 km. With radiatively active clouds SW2 is generally larger than the passive case throughout the year indicating that cloud forcing can significantly affect this component of the tide. The increased amplitude in the active case is largest during northern summer when the ACB is near its maximum thickness. Later in the season and during early fall, the ACB dissipates but the dust loading increases and the differences between the passive and active cases becomes very small at this time. As the ACB belt begins to reappear later during northern winter (see Fig. 3.1) SW2 in the active case again becomes stronger than in the passive case.

The structure of this component is shown in Fig. 4.13. The semi-diurnal tides are vertically propagating at all latitudes and hence their amplitudes increase with height everywhere. While the increase in amplitudes with active clouds is apparent, the magnitude of the increase is modest with maximum values increasing from ~5 K in the passive case to ~6 K in the active case. It is also worth noting that the fields are not symmetric about the equator as there is a stronger response in the southern hemisphere in both cases. The asymmetry is related to the zonal-mean zonal wind fields, which have a jet structure at mid southern latitudes at this season.

We can compare Fig. 4.13 with Fig. 3 in Kleinböhl et al. (2013) (not shown here) who estimate SW2 from MCS cross-track scanning data. While the patterns and overall structure are similar, their analysis suggests a much stronger response by almost a factor of 3 compared to the model. This is demonstrated in Fig. 4.14 where we compare model and MCS profiles of the amplitude and phase of SW2 at 60°S. Maximum observed amplitudes occur near the 0.3 Pa level as can also been seen in the model. However, the observed amplitudes are ~14 K compared to ~6 K in the model. Above the 10 Pa level, where amplitudes begin to increase, the phase of SW2 is much closer to observations when the clouds are radiatively active and shows a shift toward earlier local times with increasing altitude that is expected for a vertically propagating mode. Below this level the amplitudes are too small to say much about the phase.

We suspect that the weak amplitude of SW2 in the model at this season is related to the fact that the ACB is too low. Even though the model reasonably simulates the column cloud opacity at this season (Fig. 3.1), clouds at a higher altitude will be colder which would increase the radiative forcing. In Section 5.2 we discuss possible reasons for the low ACB and some possible ways to raise it.

5. Discussion

5.1. Model dryness

The ultimate source of water in the model is the NPRC. If the sublimation from the NPRC is weak this could explain the model dryness. Weak sublimation could be the result of low surface temperatures, a short sublimation season, or an underestimate of the area of the NPRC.

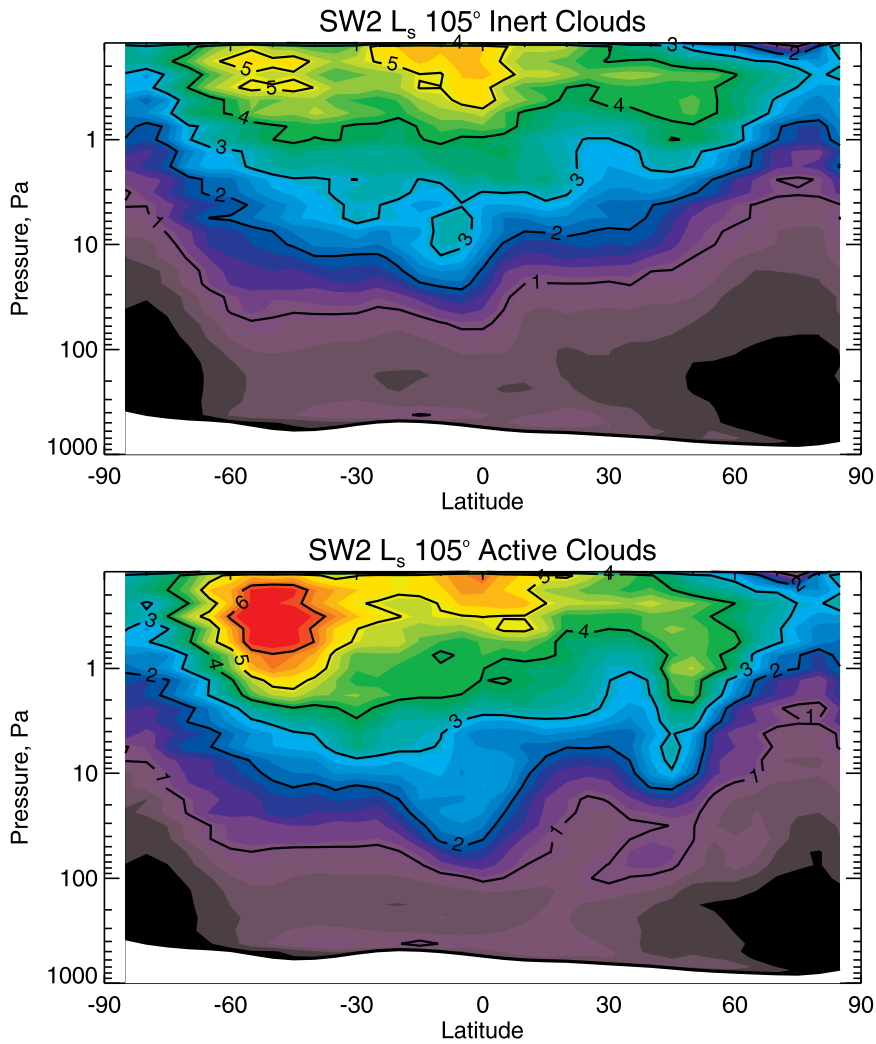

Fig. 4.13. Temperature amplitude of the migrating semi-diurnal tide for early northern summer (L_s 105°) for the inert (top) and active (bottom) simulations.

However, surface temperatures are not too low. As shown in Fig. 5.1 zonal mean surface temperatures are in good agreement with TES. Zonal mean 2 PM and 2 AM surface temperatures track TES very well during the peak sublimation season (L_s ~100–130°). The exception is the 2 AM temperatures at 85°N which are ~5–10 K too high. The point-by-point comparisons presented in Fig. 5.2 reveal the same behavior.

Figs. 5.1 and 5.2 also indicate that the sublimation season is too long. Springtime model temperatures rise too early and too quickly suggesting that not enough CO_2 ice is laid down during fall and winter, or that sub grid scale patchiness, which we do not account for, is playing a role. In either case, the sublimation season is longer than indicated in the observations.

As for the area of the cap, it is possible that the dark regions – which we do not include – are contributing significant water but it is difficult to imagine they would double the total flux into the atmosphere. Furthermore, the area of our NPRC is similar to that in Navarro et al. (2014) who do obtain global abundances closer to the observations than in our simulation. Thus, the fact that our surface temperatures agree well with TES, that our sublimation season is longer than observed, and that the area is probably reasonably well represented suggests that source strength is not the cause for the model dryness.

Perhaps then it is the sink that is too strong. The only major sink for atmospheric water vapor in the model is condensation into clouds followed by sedimentation to the ground. As shown in Fig. 5.3 sedimentation over the NPRC appears to be a major sink for atmospheric water vapor as the upward sublimation flux is significantly offset by the downward sedimentation flux. In fact, poleward of 70°N deposition onto the surface is about 50% of sublimation off the surface. Without this sink a much greater net transfer of water to the atmosphere would occur.

It is possible that because our moment scheme overestimates growth rates (see Section 2.8) ice particles grow too big and are removed too quickly. However, a separate simulation in which we arbitrarily reduced the growth rates by a factor of 1.5 does not show any significant moistening of the water cycle. Evidently, even with smaller growth rates, growth in the model is still fast enough and particles still grow big enough to fall out quickly.

Instead, it appears that the use of time splitting to reduce cloudiness over the NPRC is the direct cause of model dryness and this raises questions about the realism of this result. Is this really the mechanism by which the polar atmosphere remains cloud free during summer? In the real Martian atmosphere does water subliming off the NPRC during summer quickly condense onto large particles and immediately fall back to the surface as it does in our simulations? Is there, as our model suggests, a low-level large-particle "ground fog" with concentrations so small as to be nearly invisible but which provides enough snowfall to the surface to keep the atmosphere nearly cloud free?

In our view the existence of large-particle snowfall over the NPRC in the model is artificial and not actually a real process. We suspect that the primary reason the model is too dry is because it is too sluggish in moving water away from the NPRC both vertically and horizontally. Our level-2 Mellor-Yamada PBL scheme is diffusive in nature and does

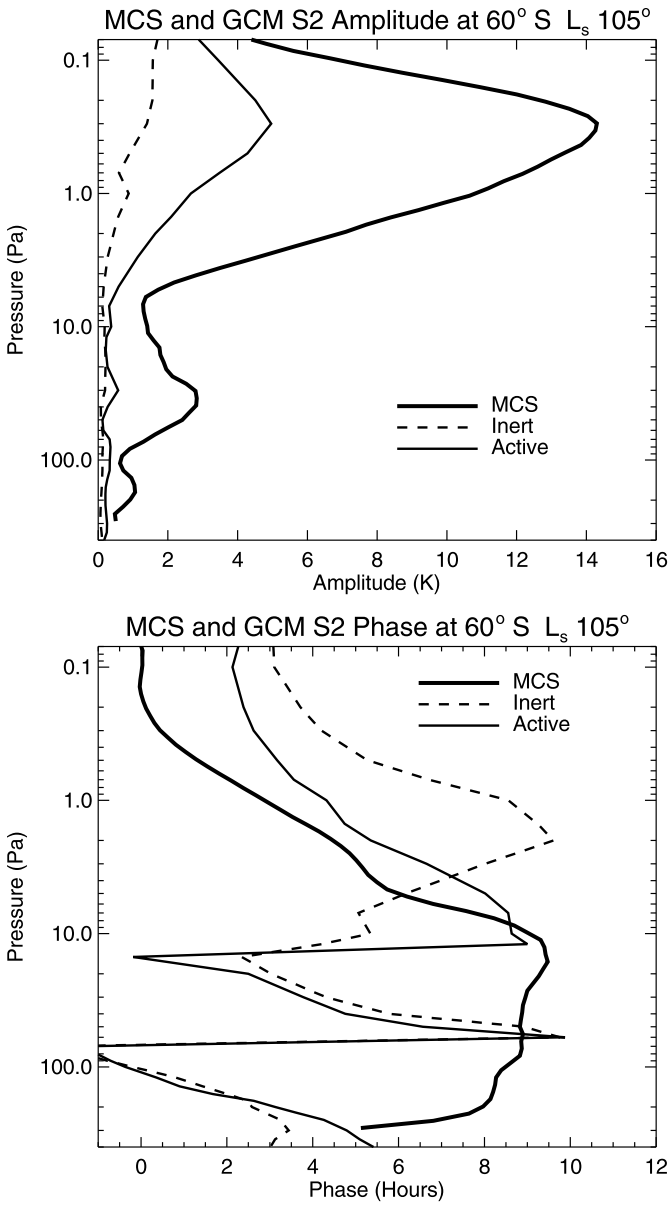

Fig. 4.14. Profiles of the temperature amplitude (top) and phase (bottom) of the semidiurnal migrating at 60°S at L_s 105°. Thick solid lines are the MCS data. Thinner lines are model results for the inert (dashed) and active (solid) cases. Amplitude is in K, phase is local time hours.

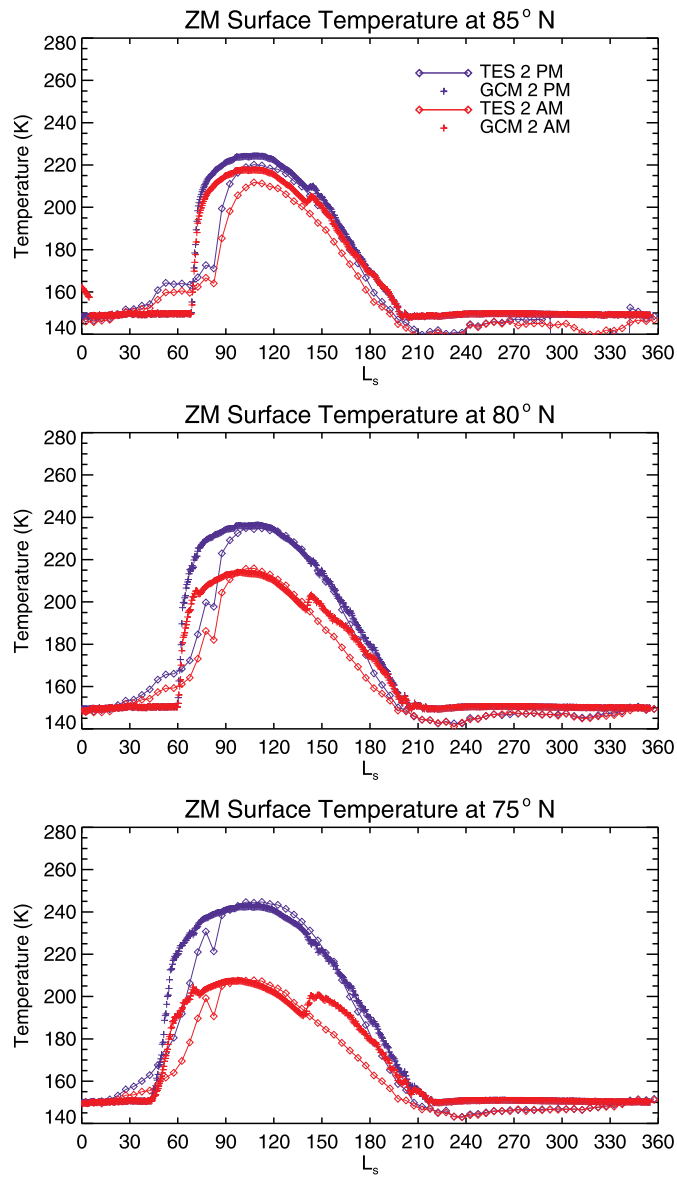

Fig. 5.1. Zonal mean surface temperatures at 2 PM (blue) and 2 AM (red) from observations (open diamonds with thin connecting line) and model (+ symbols) for three different latitudes: 85°N (top), 80°N (middle), and 75°N (bottom). (For interpretation of the references to color in this figure legend, the reader is referred to the web version of this article.)

not account for non-local mixing, which can be deeper and faster. Most of the lowest half scale height in the NPRC region is unsaturated and can hold more moisture than predicted. More vigorous vertical mixing would moisten these regions without forming clouds. Better vertical resolution may help in this regard. It could also enhance the sublimation flux by drying out near surface air and thus boosting the moisture content of the atmosphere. Indeed, our dust and temperature profiles (not shown) do indicate weak vertical mixing: compared to observations the dust is too low and upper level temperatures are too cold. Off cap meridional transport may also be too weak due to our low horizontal resolution. The mesoscale model simulation of Tyler and Barnes (2014) show this "ventilation effect" can be an important consideration. Another possibility is that the sublimation flux is high enough to supersaturate the near surface air in a single time step and the model responds by snowing it out quickly. We do not limit our sublimation rates to avoid this situation. These are all possibilities worthy of future study. For now all we can say is that without any tuning of the water cycle physics in the model and without any source other than the NPRC as we have defined it, we are unable to reproduce the observed wetness of the current water cycle.

5.2. Altitude of the aphelion cloud belt

As mentioned in Section 3.2 the altitude of the top of the ACB is too low compared to MCS observations. Peak extinctions occur at about the 100 Pa level in the model whereas they are closer to 20 Pa in the observations (see Fig. 3.5). Since the radiative effects of the clouds are included, further expansion of the Hadley circulation to bridge this gap is difficult to achieve. Instead there are several alternative explanations for why the clouds do not form high enough in the ACB. It could be that there is an insufficient supply of IN, that cloud particles grow too big and settle out too fast, that temperatures above the ACB are too cold and hence trap vapor at lower altitudes, or that the moisture supply is too limited. For all but the moisture supply issue, we used a 1-D version

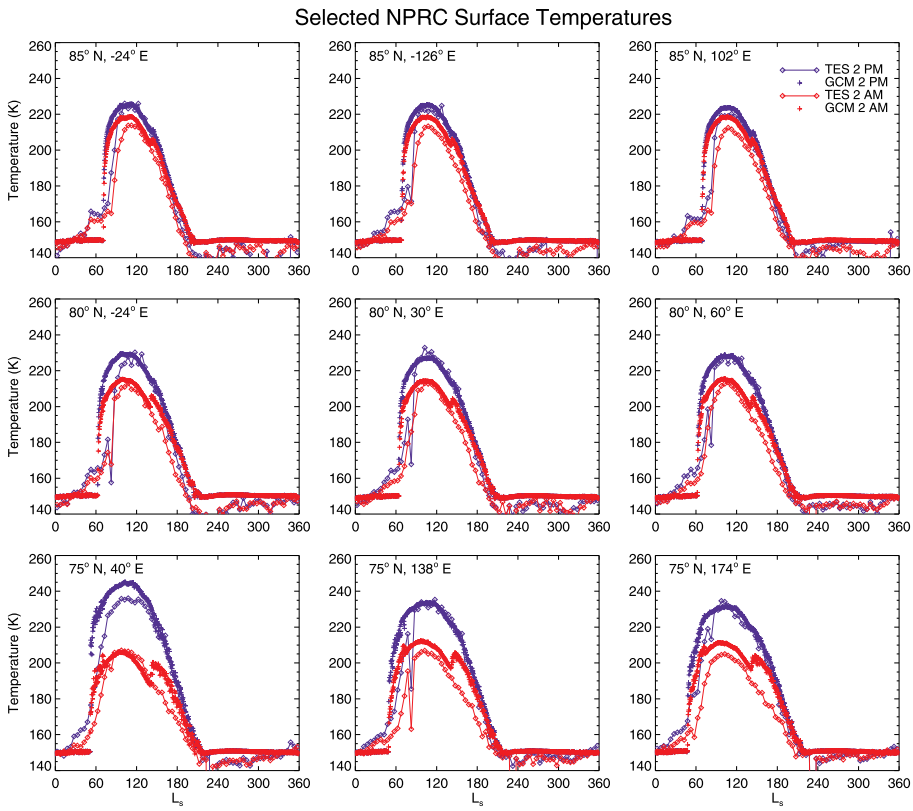

Fig. 5.2. Same as Fig. 5.1, but for selected individual points. Latitude and longitude indicated in upper left corner of each plot.

of the model to assess their potential role. For the IN issue we allowed for an infinite supply; for the cold temperature issue we introduced an elevated fixed dust layer to warm the atmosphere; and for the particle size issue we simply turned off sedimentation. While these changes did induce some changes to the thickness and elevation of the bottom of the clouds, there was very little change in altitude of the tops of the clouds. Thus, by default it would appear that the model is not providing enough moisture to higher levels for clouds to form. Again, this could be related to subgrid scale transport not adequately represented in the model. In this case a good candidate is the vertical pumping mechanism associated with mountain-induced circulations associated with volcanoes (Michaels et al., 2006). Our smoothed topography may not be capable of simulating these circulations, which are capable of injecting moisture to very high altitudes (above 40 km) and are best simulated with models running at very high horizontal and vertical resolution. Pottier et al. (2017) have taken a step in this direction and do find that the ACB thickens and deepens with increasing horizontal resolution. This is a mechanism we plan to investigate further with our next generation of dynamical cores.

5.3. High altitude clouds

To explain the difference between the observed and model clouds shown in Fig. 3.7 we adopt a working hypothesis that the high altitude polar clouds seen by MCS are formed in situ and are separate from the lower level polar hood clouds. In this case they are formed when dust and moisture are carried into the polar region by the upper branch of the mean meridional circulation. This branch extends almost all the way to the pole where it descends and adiabatically warms the atmosphere. Eventually, the air descends to cooler levels and clouds form. In this view these clouds form in situ from moisture and seed nuclei carried into the polar region at very high levels and are not related to the lower level polar hoods.

Support for this hypothesis comes from the MCS temperature, dust, and cloud observations shown in Fig. 5.4. A poleward and upward sloping warm tongue of air that extends almost all the way to the north pole on both the AM and PM sides is strong evidence that the upper branch of a deep mean meridional circulation reaches almost all the way to the pole. Moisture carried by this branch, probably in the form of clouds at first because of the cool temperatures at low latitudes, is transported into the high latitudes where it evaporates as it enters the warm tongue and then recondenses as it is forced down into the cold polar atmosphere. This scenario is consistent with the MCS cloud ice observations poleward of 80°N where most of the ice resides between 1 and 10 Pa. Further descent would produce a fork-like pattern below 10 Pa since the descending branch of the mean circulation has an equatorward component in this region of the atmosphere. Some of the ice will evaporate as it moves toward warmer air thus producing a distinct upper level maximum that is separate from the lower level annular polar hood. The fork pattern is obvious in the model but only moderately so in the observations.

The high-altitude polar clouds may also play a role in generating the CO_2 ice clouds that MCS apparently sees at the pole between 10 and 30 Pa. These clouds show up in the MCS dust channel (see Fig. 5.4) but almost certainly cannot be dust (e.g., Hayne et al., 2012). This is the coldest level in the atmosphere where temperatures are very near the CO_2 ice frost point. This is also the cleanest region of the atmosphere where our model indicates dust particle concentrations are at most $\sim 10^{-2}$ particles cm^{-3}. Since homogeneous nucleation of CO_2 ice particles is not easily achieved in the Martian atmosphere (Määttänen et al., 2005), the high-level water ice clouds are the best candidate for nucleating CO_2 ice clouds. The MCS observations show that some of the water ice clouds lie above the CO_2 ice clouds so it is possible that as they settle out they provide nucleation sites for the CO_2 clouds. It is worth noting here that this structure, water ice clouds above CO_2 ice clouds, was first detected in Mariner IRIS spectra in the early 1970s (Paige et al., 1990).

To produce the pattern seen by MCS (and Mariner 9) the model

would need to generate a stronger mean meridional circulation. It is clear from Fig. 5.4 that the model does not produce the polar warming seen in the observations. Stronger forcing of the mean meridional circulation could remedy this, but what form that forcing takes needs further study. There are several possibilities. An obvious candidate is stronger cloud forcing in the tropics. While this is not the aphelion season, there is a tropical cloud belt formed by the Hadley cell from moisture released from the south seasonal cap. In extinction space, however, the model shows very little evidence for a tropical cloud belt at this season (see Fig. 3.7). Some mechanism is needed to boost the vertical transport of water vapor and thus raise the altitude, opacity, and hence forcing of the clouds. Again, the small-scale mountain-induced plumes suggested by Michaels et al. (2006) and/or higher horizontal and vertical resolution could be important here. The subsequent radiative effects of the clouds they produce would force a stronger circulation that could in principle transport the needed moisture and seed nuclei into the deep polar regions.

Another possibility is gravity waves. The generation, propagation, and breaking of gravity waves could provide a drag force on mean zonal winds that would require stronger meridional winds for momentum balance (e.g. Joshi et al., 1995; Collins et al., 1997; Medvedev et al., 2011). Gravity wave drag has been proposed as a mechanism to warm the poles but it is not included in the present version of the model. The irregular nature of the Martian surface could easily excite a spectrum of gravity waves that under the right conditions could propagate and break at the right levels with about the right drag. We have recently introduced a gravity wave scheme into our new model and are beginning to study its effect on the circulation (Kling et al., 2018a, 2018b). There may, of course, be other processes not mentioned here that are involved but careful studies of the role of enhanced vertical transport and breaking gravity waves should provide useful insights into the nature of the high-altitude polar clouds.

5.4. Stability of the NPRC

No permanent new ice deposits develop anywhere in the model outside the NPRC. Water lost by the NPRC during summer is ultimately returned during the other seasons. The model water cycle is closed and in equilibrium. This is somewhat artificial in that we have not included the permanent SPRC of CO_2 ice near the south pole. Any water brought in contact with the SPRC will be removed from the system and thus it represents a permanent sink. Others have modeled the strength of this sink (e.g., Richardson and Wilson, 2002) and there is evidence from Mars Express observations that water is incorporated into it (Bibring et al., 2004). However, we have ignored it here and thus our water cycle is closed.

A closed water cycle, however, does not preclude a net annual redistribution of water within the NPRC. Redistribution is occurring in the model and at a fairly significant rate. As shown in Fig. 5.5 the outliers in the 75°N latitude band are losing water to the higher latitudes. Peak loss rates in some spots are ~ 1 mm per Mars year. These are similar loss rates to those found by Navarro et al. (2014) and are significant on time scales associated with orbital variations (10^5–10^6 Earth years). They suggest that a meter of ice could be transferred to the pole in ~10^3 years. While there are many uncertainties in the magnitude of these estimates, the basic concept - that a net transfer of ice within the NPRC from lower to higher latitudes is taking place at the present time - is plausible. Mesoscale models or very high resolution GCMs are the more appropriate tools to examine the details of this process.

6. Conclusions

We have described, documented, and discussed the physics packages in the legacy version of the NASA/Ames Mars Global Climate Model. We then presented results of simulations that focus on the

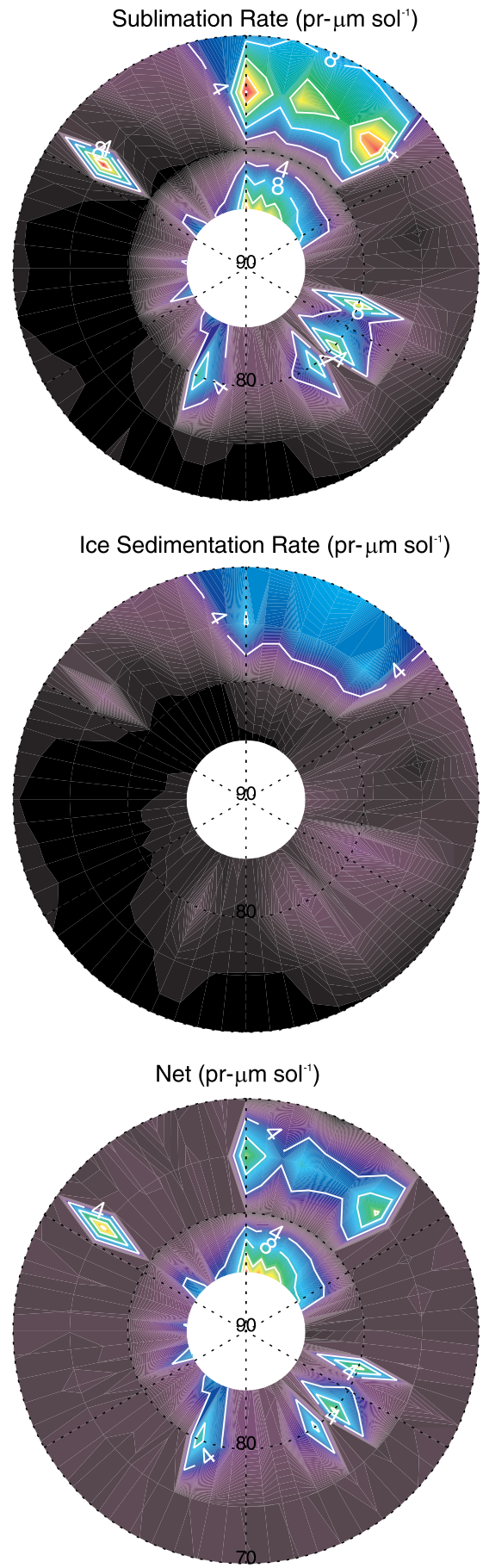

(caption on next page)

Fig. 5.3. Mass balance of the NPRC during early summer. Top: sublimation rate. Middle: sedimentation rate. Bottom: Net rate.

present seasonal water cycle and assessed the role or radiatively active clouds. The most important packages include a two-stream radiative transfer code based on correlated-k's, a suite of cloud microphysics algorithms to simulate the nucleation, growth, and gravitational settling of ice particles, a moment scheme for tracer transport, and several updates to the C-grid dynamical core.

With no tuning of the water cycle, we find it to deliver a credible simulation of the seasonal water cycle assuming the NPRC is the main source for water. The model predicts a nearly cloud free atmosphere over the cap during summer, seasonal variations in column vapor fields that track the observations, an ACB with the correct optical thickness, and surface and air temperatures that are reasonably close to those in the observations. As found in other models, the radiative effect of clouds strengthen and deepen the Hadley circulation during northern summer, but they also have significant consequences for the planetary eddy components of the global circulation: the transient eddies, stationary waves, and thermal tides. In some cases, clouds improve agreement (e.g., ACB temperatures) while in others they degrade it (e.g., SPW2 at northern equinox). Not surprisingly this suggests that more work is needed to better understand the role of cloud forcing on global circulation systems.

Where the model does not compare well with observations, weak vertical mixing appears to be the main problem. The overall dryness of the water cycle, the low altitude of the ACB, and the near absence of high altitude clouds during the perihelion season each imply that vertical transport in the model is not vigorous enough. What form that vertical transport takes needs further study to determine. Non-local PBL mixing, mountain-induced circulations, and stronger mean meridional circulations are some possibilities and each may play a role. Certainly much progress could be made from studies involving higher horizontal and vertical resolution, and the implementation of gravity wave breaking schemes. Such studies are underway at Ames as the group is transitioning to more modern dynamical cores that have better conservation properties and are written to take advantage of parallel

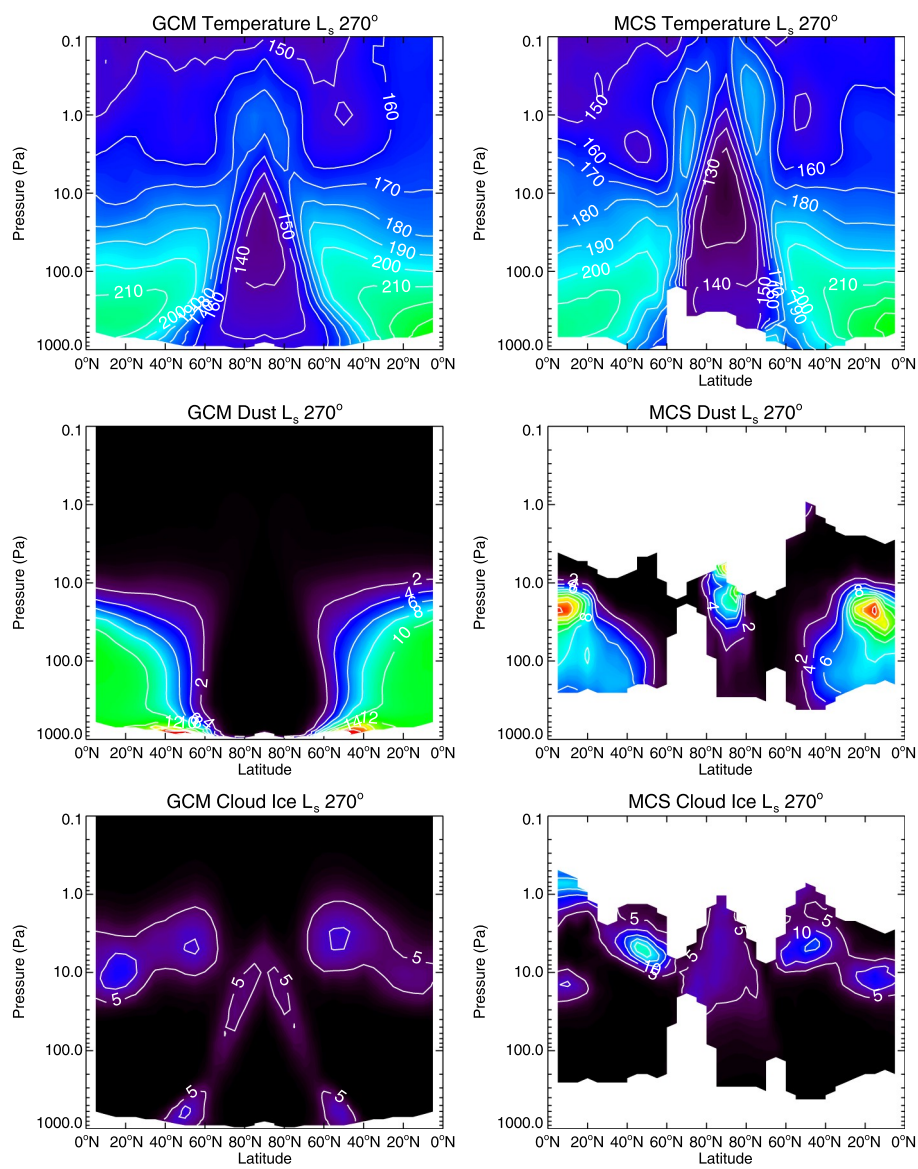

Fig. 5.4. Northern hemisphere time and zonal average temperature (top row) dust mass mixing ratio (middle row) and water ice cloud mass mixing ratio (bottom row) from the model (left column) and MCS observations (right column). Mixing ratios are 10^{-6} kg kg^{-1}. White regions in MCS plots denote no retrieved data. The x-axis shows AM on the left (0 N to 90 N) and PM on the right (90°N to 0°N). Mixing ratios from MCS data are scaled extinctions and are thus estimates of the actual mixing ratio.

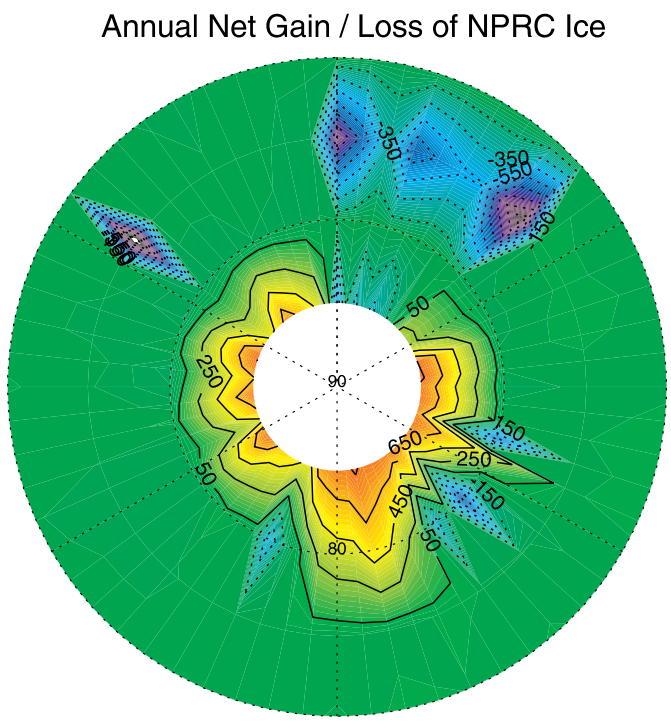

Fig. 5.5. Annual mass balance of the NPRC. Contours represent the net gain (solid) or loss (dashed) in μm.

computing and thereby improve throughput. The physics packages described here are being modularized for implementation into these new dynamical frameworks. They will be made available to the general public when validation and testing are complete.

Acknowledgments

NASA's Science Mission Directorate, Planetary Science Division, Mars Exploration Program, Mars Climate Modeling Center, and various Research and Analysis Programs supported this work. It has also benefited from discussions with many of our colleagues and in particular, Jeff Barnes, Dan Tyler, Jim Murphy, Scot Rafkin, Tim Michaels, and Rich Zurek. Folks from other groups have also contributed many stimulating discussions about modeling issues including François Forget, Thomas Navarro, Jean-Baptiste Madeleine, Aymeric Spiga, Ehouarn Millour, Stephen Lewis, Peter Read, and Brian Toon. The TES and CRISM data were kindly provided by Mike Smith, and the MCS team deserves credit for making their data readily available too. We would also like to express our appreciation to Julie Dequaire and the many other students too numerous to mention that have come to Ames to work on various aspects of the model. And of course, none of this would have been possible without the foresight and vision of Conway Leovy and Jim Pollack who began this effort almost 50 years ago.

References

Arya, P.S., 2001. Introduction to Micrometeorology, 2nd edition. Academic Press, San Diego, Ca (415 pp).

Banfield, D., Conrath, B.J., Smith, M.D., Christensen, P.R., Wilson, R.J., 2003. Forced waves in the Martian atmosphere from MGS TES nadir data. Icarus 161 (2), 319–345. https://doi.org/10.1016/S0019-1035(02)00044-1.

Barnes, J.R., 1984. Linear baroclinic instability in the Martian atmosphere. J. Atmos. Sci. 41, 1440–1536. https://doi.org/10.1175/1520-0469(1984)041(1536:LBIITM)2.0.CO;2.

Barnes, J.R., Haberle, R.M., Wilson, R.J., Lewis, S.R., Murphy, J.R., Read, P.L., 2017. The global circulation. In: Haberle, R.M., Clancy, R.T., Forget, F., Smith, M.D., Zurek, R.W. (Eds.), The Atmosphere and Climate of Mars. Cambridge University Press, pp. 229–294.

Basu, S., Richardson, M.I., Wilson, R.J., 2004. Simulation of the Martian dust cycle with the GFDL Mars GCM. J. Geophys. Res. 109 (E11). https://doi.org/10.1029/2004JE002243.

Benson, J.L., Kass, D.M., Kleinböhl, A., McCleese, D.J., Schofield, J.T., Taylor, F.W., 2010. Mars' south polar hood as observed by the Mars Climate Sounder. J. Geophys. Res. 115 (E12). https://doi.org/10.1029/2009JE003554.

Benson, J.L., Kass, D.M., Kleinböhl, A., 2011. Mars' north polar hood as observed by the Mars Climate Sounder. J. Geophys. Res. 116 (E3). https://doi.org/10.19/2010JE003693.

Bibring, J.-P., Langevin, Y., Poulet, F., Gendrin, A., Gondet, B., et al., 2004. Perennial water ice identified in the south polar cap of Mars. Nature 428, 627–630. https://doi.org/10.1038/nature02461.

Böttger, H.M., Lewis, S.R., Read, P.L., Forget, F., 2005. The effects of the Martian regolith on GCM water cycle simulations. Icarus 177, 174–189. https://doi.org/10.1016/j.icarus.2005.02.024.

Boynton, W.V., Feldman, W.C., Squyres, S.W., Prettyman, T.H., Brückner, J., et al., 2002. Distribution of hydrogen in the near surface of Mars: evidence for subsurface ice deposits. Science 297, 81–85. https://doi.org/10.1126/science.1073722.

Brutsaert, W.H. 1982. Evaporation into the Atmosphere, D. Reidel, (299 pp).

Colaprete, A., Toon, O.B., Magalhaes, J.A., 1999. Cloud formation under Mars Pathfinder conditions. J. Geophys. Res. 104 (E4), 9043–9054. https://doi.org/10.1029/1998JE00018.

Collins, M., Lewis, S.R., Read, P.L., 1997. Gravity wave drag in a global circulation model of the Martian atmosphere: parameterization and validation. Adv. Space Res. 19 (8), 1245–1254. https://doi.org/10.1016/S0273-1177(97)00277-9.

Daerden, F., Neary, L., Viscardy, S., Garcia Munoz, A., Clancy, R.T., Smith, M.D., Encrenaz, T., Fedorova, A., 2018. Mars atmospheric chemistry simulations with the GEM-Mars General Circulation Model. Icarus 326, 197–224.

Dundas, C., Byrne, S., 2010. Modeling sublimation of ice exposed by new impacts in the Martian mid-latitudes. Icarus 206 (2), 716–728. https://doi.org/10.1016/j.icarus.2009.09.007.

Feldman, W.C., Prettyman, T.H., Maurice, S., Plaut, J.J., Bish, D.L., et al., 2004. Global distribution of near-surface hydrogen on Mars. J. Geophys. Res. 109, E09006. https://doi.org/10.1029/2003JE002160.

Forget, F., Hourdin, F., Talagrand, O., 1998. CO_2 snowfall on Mars: simulation with a general circulation model. Icarus 131 (2), 302–316. https://doi.org/10.1006/icar.1997.5874.

Haberle, R.M., Jakosky, B.M., 1990. Sublimation and transport of water from the north residual polar cap on Mars. J. Geophys. Res. 95, 1423–1437. https://doi.org/10.1029/JB095iB02p01423.

Haberle, R.M., Houben, H.C., Hertenstein, R., Herdtle, T., 1993a. A boundary-layer model for Mars: comparison with Viking lander and entry data. J. Atmos. Sci. 50 (11), 1449–1554. https://doi.org/10.1175/1520-0469(1993)050<1544:ABLMFM>2.0.CO:2.

Haberle, R.M., Pollack, J.B., Barnes, J.R., Zurek, R.W., Leovy, C.B., Murphy, J.R., Lee, H., Schaeffer, J., 1993b. Mars atmospheric dynamics as simulated by the NASA Ames General Circulation Model: 1. The zonal-mean circulation. J. Geophys. Res. 98 (E2), 3093–3123. https://doi.org/10.1029/92JE02946.

Haberle, R.M., Joshi, M.M., Murphy, J.R., Barnes, J.R., Schofield, J.T., Wilson, G., Lopez-Valverde, M., Hollingsworth, J.L., Bridger, A.F.C., James, J., 1999. General circulation model simulations of the Mars Pathfinder atmospheric structure investigation/meteorology data. J. Geophys. Res. 104 (E4), 8957–8974. https://doi.org/10.1029/1998JE900040.

Haberle, R.M., Forget, F., Colaprete, A., Schaeffer, J., Boynton, W.B., Kelly, N.J., Chamberlain, M.A., 2008. The effect of ground ice on the Martian seasonal CO_2 cycle. Planet. Space Sci. 56 (2), 251–255. https://doi.org/10.1016/j.pss.2007.08.006.

Haberle, R.M., Montmessin, F., Kahre, M.A., Hollingsworth, J.L., Schaeffer, J., Wolff, M.J., Wilson, R.J., 2011. Radiative effects of water ice clouds on the Martian seasonal water cycle. 4th International Workshop on the Mars Atmosphere: Modelling and Observation. Feb 8–11, 2011. Paris, France. http://www-mars.lmd.jussieu.fr/paris2011/program.html.

Haberle, R.M., Kahre, M.A., Hollingsworth, J.L., Schaeffer, J., Montmessin, F., Phillips, R.J., 2012. A cloud greenhouse effect on Mars: Significant climate change in the recent past? In: 43rd Lunar and Planetary Science Conference. March 19–23, 2012, the Woodlands, Texas. LPI Contribution No. 1659, Id, pp. 1665.

Haberle, R.M., de la Torre Juarez, M., Kahre, M.A., Kass, D.M., Barnes, J.R., Hollingsworth, J.L., Harri, A.-M., Kahanpää, H., 2019a. Detection of northern hemisphere transient eddies at Gale Crater Mars. Icarus 307, 150–160. https://doi.org/10.1016/j.icarus.2018.02.013.

Haberle, R.M., Kahre, M.A., Barnes, J.R., Hollingsworth, J.L., Wolff, M.J., 2019b. MARCI observations of a wavenumber-2 large-scale feature in the North Polar Hood of Mars: Interpretation with the NASA/Ames Legacy Mars Global Climate Model. Icarus (submitted).

Hayne, P.O., Paige, D.A., Schofield, J.T., Kass, D.M., Kleinböhl, A., Heavens, N.G., McCleese, D.J., 2012. Carbon dioxide snow clouds on Mars: south polar winter observations by the Mars Climate Sounder. J. Geophys. Res. 117, E08014. https://doi.org/10.1029/2011JE004040.

Hecht, M.H., 2002. Metastability of liquid water on Mars. Icarus 156 (2), 373–386. https://doi.org/10.1006/icar.2001.6794.

Hinson, D.P., Wang, H., 2010. Further observations of regional dust storms and baroclinic eddies in the northern hemisphere of Mars. Icarus 206, 290–305. https://doi.org/10.1016/j.icarus.2009.08.019.

Hinson, D.P., Wilson, R.J., 2004. Temperature inversions, thermal tides, and water ice clouds in the Martian tropics. J. Geophys. Res. 109, E01002. https://doi.org/10.1029/2003JE0022129.

Hollingsworth, J.L., Barnes, J.R., 1996. Forced stationary planetary waves in Mars's winter atmosphere. J. Atmos. Sci. 53 (3), 428–448. https://doi.org/10.1175/1520-

0469(1996)053<0428:FSPWIM>2.0.CO;2.
Hourdin, F., Armengaud, A., 1999. The use of finite-volume methods for atmospheric advection of trace species. Part I: test of various formulations in a general circulation model. Mon. Weather Rev. 127, 822–837. https://doi.org/10.1175/1520-0493(1999)127<0822:TUOFVM>2.0.CO;2.
Hourdin, F., Forget, F., Talagrand, O., 1995. The sensitivity of the Martian surface pressure and atmospheric mass budget to various parameters: a comparison between numerical simulations and Viking observations. J. Geophys. Res. 100 (E3), 5501–5523. https://doi.org/10.1029/94JE03079.
Ingersoll, A.P., 1970. Mars: occurrence of liquid water. Science 168 (3934), 972–973. https://doi.org/10.1126/science.168.3934.972.
Iraci, L.T., Phebus, B.D., Stone, B.M., Colaprete, A., 2010. Water ice cloud formation on Mars is more difficult than presumed: laboratory studies of ice nucleation on surrogate materials. Icarus 210 (2), 985–991. https://doi.org/10.1016/j.icarus.2010.07.020.
Jacobson, M.Z., 2005. Fundamentals of Atmospheric Modeling, 2nd edition. Cambridge University Press (813 pp).
Joshi, M.M., Lawrence, B.N., Lewis, S.R., 1995. Gravity wave drag in three-dimensional atmospheric models of Mars. J. Geophys. Res. 100 (E10), 21235–21246. https://doi.org/10.1029/95JE02486.
Kahre, M.A., Murphy, J.R., Haberle, R.M., 2006. Modeling the Martian dust cycle and surface dust reservoirs with the NASA Ames general circulation model. J. Geophys. Res. 111 (E6). https://doi.org/10.1029/2005JE002588.
Kahre, M.A., Hollingsworth, J.L., Haberle, R.M., Murphy, J.R., 2008. Investigations of the variability of dust particle sizes in the Martian atmosphere using the NASA Ames general circulation model. Icarus 195 (2), 576–597. https://doi.org/10.106/j.icarus.2008.01.023.
Kahre, M.A., Hollingsworth, J.L., Haberle, R.M., Wilson, R.J., 2015. Coupling the Mars dust and water cycles: the importance of radiative-dynamic feedbacks during northern hemisphere summer. Icarus 260, 477–480. https://doi.org/10.1016/j.icarus.2014.07.017.
Kahre, M.A., Murphy, J.R., Newman, C.E., Wilson, R.J., Cantor, B.A., Lemmon, M.T., Wolff, M.J., 2017. The Mars dust cycle. In: Haberle, R.M., Clancy, R.T., Forget, F., Smith, M.D., Zurek, R.W. (Eds.), The Atmosphere and Climate of Mars. Cambridge University Press, pp. 295–337.
Kahre, M.A., Haberle, R.M., Hollingsworth, J.L., Wolff, M.J., 2019. MARCI-observed clouds in the Hellas Basin during Northern Hemisphere summer on Mars: Interpretation with the NASA/Ames Legacy Mars Global Climate Model. Icarus (submitted).
Kass, D.M., Kleinböhl, A., McCleese, D.J., Schofield, J.T., Smith, M.D., 2016. Interannual similarity in the Martian atmosphere during the dust storm season. Geophys. Res. Lett. 43 (12), 6111–6118. https://doi.org/10.1002/2016GL068978.
Keesee, R.G., 1989. Nucleation and particle formation in the upper atmosphere. J. Geophys. Res. 94 (D12), 14683–14692. https://doi.org/10.1029/JD094iD12p14683.
Klassen, D.R., Kahre, M.A., Wolff, M.J., Haberle, R.M., Hollingsworth, J.L., 2017. Modeling MARCI and TES aphelion cloud belt optical depth peak differences with the Ames MGCM. In: 6th International Workshop on the Mars Atmosphere: Modelling and Observation. Jan 17,20,2017, Granada, Spain, . http://www-mars.lmd.jussieu.fr/granada2017/abstracts/klassen_granada2017.pdf.
Kleinböhl, A., Schofield, J.T., Kass, D.M., Abdou, W.A., Backus, C.R., Sen, B., Shirley, J.H., Lawson, W.G., Richardson, M.I., Taylor, F.W., Teanby, N.A., McCleese, D.J., 2009. Mars Climate Sounder limb profile retrieval of atmospheric temperature, pressure, and dust and water ice opacity. J. Geophys. Res. 114 (E10). https://doi.org/10.1029/2009JE003358.
Kleinböhl, A., Wilson, R.J., Kass, D., Schofield, J.T., McCleese, D.J., 2013. The semi-diurnal tide in the middle atmosphere of Mars. Geophys. Res. Lett. 40. https://doi.org/10.1002/grl.50497.
Kling, A., Kahre, M., Wilson, J., Brecht, A., Murphy, J., 2018a. Gravity wave drag parameterization for the new generation of Mars Global Circulation Models. In: European Planetary Science Conference, Vol. 12, EPSC2018-680, Berlin, Germany.
Kling, A., Kahre, M., Wilson, J., Brecht, A., Murphy, J., 2018b. Investigating Parameterized and Resolved Gravity Waves in the Martian Atmosphere With the NASA Ames Mars Global Climate Model. Fall AGU Meeting, Washington, D.C. (P431-3853).
Lee, C., Richardson, M.I., Newman, C.E., Mischna, M.A., 2018. The sensitivity of solsticial pauses to atmospheric ice and dust in the MarsWRF general circulation model. Icarus. https://doi.org/10.106/j.icarus.2018.03.019. In Press.
Lewis, S.R., Mulholland, D.P., Read, P.L., Montabone, L., Wilson, R.J., Smith, M.D., 2016. The solsticial pause on Mars: 1. A planetary wave reanalysis. Icarus 264, 456–464. https://doi.org/10.1016/j.icarus.2015.08.039.
Määttänen, A., Vehkamäki, H., Lauri, A., Merikallio, S., Kauhanen, J., Savijärvi, H., 2005. Nucleation studies in the Martian atmosphere. J. Geophys. Res. 110 (E2). https://doi.org/10.1029/2004JE002308.
MacKenzie, A.R., Haynes, P.H., 1992. The influence of surface kinetics on the growth of stratospheric ice crystals. J. Geophys. Res. 97 (D8), 8057–8064. https://doi.org/10.1029/91JD01436.
Madeleine, J.-B., Forget, F., Millour, E., Navarro, T., Spiga, A., 2012. The influence of radiatively active water ice clouds on the Martian climate. Geophys. Res. Lett. 39, L23202. https://doi.org/10.1029/2012GL053564.
Madeleine, J.-B., Head, J.W., Forget, F., Navarro, T., Millour, E., Spiga, A., Colaïtis, A., Määtänen, A., Montmessin, F., Dickson, J.L., 2014. Recent Ice Ages on Mars: the role of radiatively active clouds and cloud microphysics. Geophys. Res. Lett. 41, 4873–4879. https://doi.org/10.10002/2014GL059861.
Martin-Torres, F.J., Zorzano, M.-P., Valentín-Serrano, P., Ari-Matti, Harri, Genzer, M., et al., 2015. Transient liquid water and water activity at Gale crater on Mars. Nat. Geosci. 8, 357–361. https://doi.org/10.1038/ngeo2412.
Medvedev, A.S., Yigit, E., Hartogh, P., Becker, E., 2011. Influence of gravity waves on the Martian atmosphere: general circulation modeling. J. Geophys. Res. 116 (E10). https://doi.org/10.1029/2011JE003848.
Mellor, G.L., Yamada, T., 1982. Development of a turbulence closure model for geophysical fluid problems. Rev. Geophys. Space Phys. 20, 851–875. https://doi.org/10.1029/RG020i004p00851.
Michaels, T.I., Colaprete, A., Rafkin, S.C.R., 2006. Significant vertical water transport by mountain-induced circulations on Mars. Geophys. Res. Lett. 33, L16201. https://doi.org/10.1029/2006GL026562.
Michelangeli, D.V., Toon, O.B., Haberle, R.M., Pollack, J.B., 1993. Numerical simulations of the formation and evolution of water ice clouds in the Martian atmosphere. Icarus 100, 261–285. https://doi.org/10.1006/icar.1993.1048.
Montabone, L., Forget, F., Millour, E., Wilson, R.J., Lewis, S.R., et al., 2015. Eight-year climatology of dust optical depth on Mars. Icarus 251, 65–95. https://doi.org/10.1016/j.icarus.2014.12.034.
Montmessin, F., Rannou, P., Cabane, M., 2002. New insights into Martian dust distribution and water-ice cloud microphysics. J. Geophys. Res. 107 (E6), 5037. https://doi.org/10.1029/2001JE001520.
Montmessin, F., Forget, F., Rannou, P., Cabane, M., Haberle, R.M., 2004. Origin and role of water ice clouds in the Martian water cycle as inferred from a general circulation model. J. Geophys. Res. 109. https://doi.org/10.1029/2004JE002284.
Montmessin, F., Smith, M.D., Langevin, Y., Mellon, M.T., Fedorova, A., 2017. The water cycle. In: Haberle, R.M., Clancy, R.T., Forget, F., Smith, M.D., Zurek, R.W. (Eds.), The Atmosphere and Climate of Mars. Cambridge University Press, pp. 338–373.
Mulholland, D.P., Lewis, S.R., Read, P.L., Madeleine, J.-B., Forget, F., 2016. The solsticial pause on Mars: 2 modelling and investigation of causes. Icarus 264, 465–477. https://doi.org/10.1016/j.icarus.2015.08.038.
Musiolik, G., Kruss, M., Demirci, T., et al., 2018. Saltation under Martian gravity and its influence on the global dust distribution. Icarus 306, 25–31. https://doi.org/10.1016/j.icarus.2018.01.007.
Navarro, T., Madeleine, J.-B., Forget, F., Spiga, A., Millour, E., Montmessin, F., Määttänen, A., 2014. Global climate modeling of the Martian water cycle with improved microphysics and radiatively active water ice clouds. J. Geophys. Res. 119 (7), 1479–1495. https://doi.org/10.1002/2013JE004550.
Neary, L., Daerden, F., 2018. The GEM-Mars general circulation model for Mars: description and evaluation. Icarus 300, 458–476. https://doi.org/10.1016/j.icarus.2017.09.028.
Newman, C.E., Lewis, S.R., Read, P.L., Forget, F., 2002a. Modeling the Martian dust cycle, 1. Representations of dust transport processes. J. Geophys. Res. 107 (E12). https://doi.org/10.1029/2002JE001910.
Newman, C.E., Lewis, S.R., Read, P.L., Forget, F., 2002b. Modeling the Martian dust cycle, 2. Multiannual radiatively active dust transport simulations. J. Geophys. Res. 107 (E12). https://doi.org/10.1029/2002JE001920.
Paige, D.A., Crisp, D., Santee, M.L., 1990. Bull. Astron. Soc. 22, 1075.
Pottier, A., Forget, F., Montmessin, F., Navarro, T., Spiga, A., Millour, E., Szantai, A., Madeleine, J.-B., 2017. Unraveling the Martian water cycle with high-resolution global climate simulations. Icarus 291, 82–106. https://doi.org/10.1016/j.icarus.2017.02.016.
Prettyman, T.H., Feldman, W.C., Mellon, M.T., McKinney, G.W., Boynton, W.V., et al., 2004. Composition and structure of the Martian surface at high southern latitudes from neutron spectroscopy. J. Geophys. Res. 109 (E5). https://doi.org/10.109/2003JE002139.
Pruppacher, H.R., Klett, J.D., 1997. Microphysics of Clouds and Precipitation, Second edition. Kluwer Academic Publishers, Dordrecht, The Netherlands 954 pp. (ISBN 0-79-234221-1).
Putzig, N.E., Mellon, M.T., 2007. Apparent thermal inertia and the surface heterogeneity of Mars. Icarus 191, 68–94. https://doi.org/10.1016/j.icarus.2007.05.013.
Rennó, N.O., Burkett, M.L., Larkin, M.P., 1998. A simple thermodynamical theory for dust devils. J. Atmos. Sci. 55, 3244–3252.
Richardson, M.I., Wilson, R.J., 2002. Investigation of the nature and stability of the Martian seasonal water cycle with a general circulation model. J. Geophys. Res. 107 (E5). https://doi.org/10.1029/2001JE001536.
Rodin, A.V., 2002. On the moment method for the modeling of cloud microphysics in rarefied turbulent atmospheres: I. condensation and mixing. Sol. Syst. Res. 36, 97–106.
Savijärvi, H., 1995. Mars boundary layer modeling: diurnal moisture cycle and soil properties at the Viking Lander 1 Site. Icarus 117, 120–127. https://doi.org/10.1006/icar.1995.1146.
Seki, J., Hasegawa, H., 1983. The heterogeneous condensation of interstellar ice grains. Astrophys. Space Sci. 94, 177–189. https://doi.org/10.1007/BF00651770.
Shaposhnikov, D.S., Rodin, A.V., Medvedev, A.S., Fedorova, A.A., Kuroda, T., Hartogh, P., 2018. Modeling the hydrological cycle in the atmosphere of Mars: influence of a bimodal size distribution of aerosol nucleation particles. J. Geophys. Res. https://doi.org/10.1002/2017JE005384. In Press.
Smith, M.D., 2002. The annual cycle of water vapor on Mars as observed by the Thermal Emission Spectrometer. J. Geophys. Res. 107 (E11). https://doi.org/10.1029/2001JE001522.
Smith, D.E., Zuber, M.T., Solomon, S.C., Phillips, R.J., Head, J.W., et al., 1999. The global topography of Mars and implications for surface evolution. Science 284, 1495. https://doi.org/10.1126/science.284.5419.1495.
Smith, M.D., Daerden, F., Neary, L., Khayat, A., 2018. The climatology of carbon monoxide and water vapor on Mars as observed by CRISM and modeled by the GEM-Mars general circulation model. Icarus 301, 17–131. https://doi.org/10.1016/j.icarus.2017.09.027.
Steele, L.J., Lewis, S.R., Patel, M.R., Montmessin, F., Forget, F., Smith, M.D., 2014. The seasonal cycle of water vapour on Mars from assimilation of Thermal Emission

Spectrometer data. Icarus 237, 97–115. https://doi.org/10.106/j.icarus.2014.04.017.
Suarez, M.J., Takacs, L.L., 1995. Documentation of the AIRES/GEOS Dynamical Core: Version 2. NASA Technical Memorandum 104606. vol. 5 Goddard Space Flight Center, Greenbelt, Maryland.
Toon, O.B., McKay, C.P., Ackerman, T.P., Santhanam, K., 1989. Rapid calculation of radiative heating rates and photodissociation rates in inhomogeneous multiple scattering atmospheres. J. Geophys. Res. 92, 16287–16301. https://doi.org/10.1029/JD094iD13p16287.
Tyler, D., Barnes, J.R., 2014. Atmospheric mesoscale modeling of water and clouds during northern summer on Mars. Icarus 237, 388–414. https://doi.org/10.1016/j.icarus.2014.04.0202.
Urata, R., Toon, O.B., 2013. Simulations of the Martian hydrologic cycle with a general circulation model: implications for the ancient Martian climate. Icarus 226, 229–250. https://doi.org/10.106/j.icarus.2013.05.014.
Wang, H., 2018. Cross-equatorial flushing dust storms and northern hemisphere transient eddies – an analysis for Mars year 24. J. Geophys. Res. 123, 1732–1745.
Wang, H., Fisher, J.A., 2009. North polar frontal clouds and dust storms on Mars during spring and summer. Icarus 204, 103–113. https://doi.org/10.1016/j.icarus.2009.05.028.
Wang, H., Ingersoll, A.P., 2002. Martian clouds observed by Mars Global Surveyor Mars Orbiter Camera. J. Geophys. Res. 107 (E10). https://doi.org/10.1029/20201JE001815.
Wang, H., Richardson, M.I., Wilson, R.J., Ingersoll, A.P., Toigo, A.D., Zurek, R.W., 2003. Cyclones, tides, and the origin of a cross-equatorial dust storm on Mars. Geophys. Res. Lett. 30. https://doi.org/10.1039/2002/GL016828.
Warren, S.G., 1984. Optical constants of ice from the ultraviolet to the microwave. Appl. Opt. 23, 1206–1225. https://doi.org/10.1364/AO.23.001206.
Williams, K.E., Toon, O.B., Heldmann, J.L., McKay, C., Mellon, M.T., 2008. Stability of mid-latitude snowpacks on Mars. Icarus 196, 565–577. https://doi.org/10.1026/j.icarus.2008.03.017.
Wilson, R.J., 2011. Dust cycle modeling with the GFDL Mars general circulation model. In: 4th International Workshop on the Mars Atmosphere: Modelling and Observation. Feb 8–11, 2011. Paris, France, . http://www-mars.lmd.jussieu.fr/paris2011/program.html.
Wilson, R.J., Guzewich, S.D., 2014. Influence of water ice clouds on nighttime tropical temperature structure as seen by the Mars Climate Sounder. Geophys. Res. Lett. 41, 3375–3381. https://doi.org/10.1002/2014GL060086.
Wilson, R.J., Lewis, S.R., Montabone, L., Smith, M.D., 2008. Influence of water ice clouds on Martian tropical atmospheric temperatures. Geophys. Res. Lett. 35. https://doi.org/10.1029/2007GL032405.
Wilson, R.J., Millour, E., Navarro, T., Forget, F., Kahre, M., 2014. GCM simulations of aphelion season tropical cloud and temperature structure. In: 5th International Workshop on the Mars Atmosphere: Modelling and Observation. Jan. 13–16, 2014, Oxford, UK. Id.1304, . http://www-mars.lmd.jussieu.fr/oxford2014/program.htm.
Wolff, M.J., Smith, M.D., Clancy, R.T., Arvidson, R., Kahre, M., Seelos IV, F., Murchie, S., Savijärvi, H., 2009. Wavelength dependence of dust aerosol single scattering albedo as observed by the Compact Reconnaissance Imaging Spectrometer. J. Geophys. Res. 114 (E00D04). https://doi.org/10.1029/2009JE003350.
Zent, A.P., Quinn, R.C., 1997. Measurement of H_2O adsorption under Mars-like conditions: effects of adsorbent heterogeneity. J. Geophys. Res. 102 (E4), 9085–9096. https://doi.org/10.1029/96JE03420.